universität wien

DISSERTATION / DOCTORAL THESIS

Titel der Disseratation / Title of the Doctoral Thesis

„Electron beam shaping with light“

verfasst von / submitted by

Marius Constantin Chirita Mihaila MSc

angestrebter akademischer Grad / in partial fulfilment of the requirements for the degree of

Doktor der Naturwissenschaften (Dr. rer. nat.)

Wien, 2022 / Vienna, 2022

Studienkennzahl lt. Studienblatt / degree programme code as it appears on the student record sheet:	UA 796 605 411
Studienrichtung lt. Studienblatt / degree programme as it appears on the student record sheet:	Doktoratsstudium Physik
Betreut von / Supervisor:	Assoc.-Prof. Dipl.-Ing. Dr. Thomas Juffmann

I dedicate this thesis to my family

Statement of contribution

This dissertation contains data published in the following article: Phys. Rev. X 12, 031043 (2022).

My contribution to the article: design of the experiment (equal), construction of the experimental setup (lead), data acquisition (lead), data analysis (equal), preparation of manuscript (equal), theoretical framework of the ponderomotive interaction (no contribution).

This dissertation contains also data that is not published in any journal. The contribution of others is stated in the acknowledgements section and in the text.

Acknowledgments

First, I want to thank my supervisor Thomas Juffmann for his continuous scientific feedback over the years and for his patience when correcting my dissertation. The lab was empty when I joined Thomas, so we built all the required technology from scratch. With his active help, this dissertation was possible.

Furthermore, working closely with Phillip Weber was a privilege and a great pleasure. Most notably, Phillip designed the 3D drawing of the optical setup inside the vacuum and assisted me with the Ronchigram measurements and synchronization of electron-laser pulses. Special thanks go to the master's students Matthias Schneller and Lucas Grandits. Matthias did the simulations of electron-light interaction, and Lucas assisted me with the experimental ponderomotive measurements. Furthermore, both Matthias and Lucas helped me with the evaluation of the ponderomotive data. Also, I want to thank Stefan Nimmrichter, who derived the ponderomotive phase shift formula (sub-chapter 2.2) with Thomas and my colleagues.

Thank Francisco Balzarotti for interesting discussions about Laguerre-Gauss beams. Also, I want to thank the Electron Microscopy Facility team at Vienna BioCenter Core Facilities for the gold coating of the carbon sample and scintillator and for borrowing the 200 microns aperture we used for some of the Ronchigram experiments. I thank my colleagues Franz, Remi, Francisco, Clara, Dante, Lukas, Felix, Ronja, Ian, Peter, Hanieh, Ilia, and the administrative team at VBC5. Furthermore, I want to thank Sebastian Lekart and my friends for their moral support along the way.

Abstract

The precise transverse control of electrons is at the heart of any high-resolution electron microscope where electron lenses and multipole aberration correctors have enabled sub-Angström spatial resolution.

This thesis describes a novel way of achieving transverse control over the electrons by interaction with shaped light fields. An experimental setup has been built from scratch and is based on a scanning electron microscope, which has been modified to allow ultra-short laser-triggered electron pulses and operation in transmission mode. In the modified specimen chamber of the scanning electron microscope, the electrons interact in free space with a counter-propagating transversely shaped laser. During the interaction with the laser, the electrons acquire a local phase shift proportional to the laser's local pulse energy density. Electron displacements are measured with a position-sensitive detector.

The transverse profile of the laser beam is shaped by diffractive optical phase masks, which are displayed on a spatial light modulator. A Gerchberg-Saxton algorithm has been modified to calculate the required phase mask, which allows for minimizing heating effects along the beam path and produces speckle-free laser distributions.

For the electron-light interaction to take place, temporal and spatial overlap between pulses is established in a two-step process without an energy filter. First, a fast-timing scintillator is placed in the interaction plane. The arrival time of electron-triggered photons and laser is recorded with a silicon photomultiplier, and the delay stage is adjusted accordingly. Second, pump-probe measurements are carried out with a copper grid in the interaction plane, synchronizing the pulses with an uncertainty of $\sim 1ps$.

Programmable lossless transverse electron beam-shaping and both concave and convex electron lensing via ponderomotive scattering in free space is demonstrated. Furthermore, an electron Ronchigram in pulsed mode is recorded, which opens up the possibility of doing coherent experiments with the modified microscope. Selected applications that can arise from the electron phase modulation with light are programmable phase plates for contrast enhancement, generation of exotic beams, aberration correction of traditional electron lenses, and more versatile electron microscopes with lenses made out of light.

Kurzfassung

Die präzise transverale Kontrolle von Elektronen ist das Herzstück jedes hochauflösenden Elektronenmikroskops, bei dem Elektronenlinsen und Multipol-Aberrationskorrektoren eine räumliche Auflösung unterhalb von Angström ermöglichen.

Diese Dissertation beschreibt einen neuartigen Weg, wie durch Wechselwirkung mit geformten Lichtfeldern eine transversale Kontrolle über die Elektronen erreicht werden kann. Ein komplett neu aufgebauter Versuchsaufbau basiert auf einem Rasterelektronenmikroskop, das für ultrakurze lasergetriggerte Elektronenpulse und den Betrieb im Transmissionsmodus modifiziert wurde. In der modifizierten Probenkammer des Rasterelektronenmikroskops wechselwirken die Elektronen im freien Raum mit einem gegenläufigen, transversal geformten Laser. Während der Wechselwirkung mit dem Laser erhalten die Elektronen eine lokale Phasenverschiebung proportional zur lokalen Pulsenergiedichte des Lasers. Elektronenverschiebungen werden mit einem Detektor gemessen.

Die transversale Intensitätsverteilung des Laserstrahls wird durch diffraktive optische Phasenmasken geformt, die auf einem räumlichen Lichtmodulator abgebildet werden. Ein Gerchberg-Saxton-Algorithmus wurde modifiziert, um die erforderliche Phasenmaske zu berechnen, die eine Minimierung von Erwärmungseffekten entlang des Strahlengangs ermöglicht und speckle-freie Intensitätsverteilungen erzeugt.

Damit die Elektron-Licht-Wechselwirkung stattfinden kann, wird eine zeitliche und räumliche Überlappung zwischen Pulsen in einem zweistufigen Prozess ohne Energiefilter hergestellt. Zunächst wird ein Szintillator in der Interaktionsebene platziert. Die Ankunftszeit von elektronengetriggerten Photonen und Laser wird mit einem Silizium-Photomultiplier aufgezeichnet und die Verzögerung entsprechend angepasst. Im zweiten Schritt werden Pump-Probe Messungen mit einem Kupfergitter in der Wechselwirkungsebene durchgeführt, wobei die Pulse mit einer Unsicherheit von $\sim 1ps$ synchronisiert werden.

Es wird eine programmierbare verlustfreie transversale Elektronenstrahlformung und sowohl konkave als auch konvexe Elektronenlinsen durch ponderomotorische Streuung im freien Raum demonstriert. Außerdem wird ein Elektronen-Ronchigramm im Pulsmodus aufgenommen, was die Möglichkeit eröffnet, kohärente Experimente mit dem modifizierten Mikroskop durchzuführen. Ausgewählte Anwendungen, die sich aus der Elektronenphasenmodulation mit Licht ergeben können, sind programmierbare Phasenplatten zur Kontrastverstärkung, Erzeugung exotischer Strahlen, Aberrationskorrektur herkömmlicher Elektronenlinsen und vielseitigere Elektronenmikroskope mit Linsen aus Licht.

Contents

Statement of contribution ii

Acknowledgments iii

Abstract iv

Kurzfassung v

1 Introduction 1
- 1.1 Ultrafast electron miscroscopy . . . 1
- 1.2 Structure of the thesis . . . 4

2 Theoretical background 6
- 2.1 Relativistic quantum description of the electron in an electromagnetic field 6
  - 2.1.1 Electric and magnetic fields expressed as potentials . . . 6
  - 2.1.2 Schrödinger and Klein-Gordon equation of a relativistic charged particle in an electromagnetic field . . . 7
  - 2.1.3 The Pauli Equation for an electron in an electromagnetic field . . . 8
  - 2.1.4 The Dirac equation . . . 9
- 2.2 Ponderomotive interaction for a relativistic charged particle . . . 10

3 Experimental Setup 13
- 3.1 Noise sources in the SEM region . . . 14
- 3.2 The procedure of creating the pulsed electron beam . . . 15
- 3.3 Electron detection system . . . 16
- 3.4 Optical setup . . . 17

4 Wavefront Shaping of the Laser Beam 19
- 4.1 Spatial Light Modulator . . . 19
- 4.2 The Gerchberg Saxton algorithm (GSA) . . . 19
- 4.3 Modified Gerchberg-Saxton algorithm . . . 20
  - 4.3.1 Inclusion of elements in the iterative algorithm with Fresnel propagation . . . 20
  - 4.3.2 Speckle suppression of the desired intensity distribution with an initial quadratic phase . . . 25
  - 4.3.3 Shaping the laser beam for electron deflections . . . 28
  - 4.3.4 The Laguerre Gauss beam of charge one . . . 31

5 Spatial and temporal overlap between electrons and light pulses without an energy filter **34**
5.1 Reducing the timing mismatch between the laser and electron pulse 34
5.1.1 Fast-timing scintillators 34
5.1.2 Ultra-low light intensity detection with Silicon Photomultipliers . . 35
5.1.3 Quantitative time delay measurement 36
5.2 Pump-probe measurement with a copper grid to establish the spatial and temporal overlap 38
5.3 Spatial and temporal overlap with ponderomotive deflection 40

6 Transverse Phase Modulation of Electron-waves using Light **43**
6.1 Programmable electron beam shaping 43
6.2 Ponderomotive lensing 47
6.2.1 Laser pulse energy loss along the beam path 48
6.2.2 Laser-based concave lens for electrons 50
6.2.3 Laser-based convex lens for electrons 53
6.2.4 Moving the interaction plane in the z-direction 55

7 Diagnosis of electron microscope aberrations **57**
7.1 Probe size limiting factors in electron microscopy 57
7.1.1 Ronchigram Simulation 62
7.1.2 Experimental Ronchigram measurement in continuous mode 65
7.1.3 Experimental Ronchigram measurement in pulsed mode 66
7.2 Light-based electron optics for spherical aberration correction of electron beams 68

8 Discussion **72**

9 Conclusion and Outlook **76**

Bibliography **77**

10 Appendix **96**
10.1 Laser beam power measurement 96

1 Introduction

This thesis describes an experiment built from scratch, which demonstrates transverse, programmable phase shaping of electron waves using counter-propagating, shaped ponderomotive potentials from high-intensity laser pulses. The scanning electron microscope has been modified, and the required infrastructure has been built to have on-axis interaction between electron and laser pulses. The experiments are carried out in a high laser pulse energy regime such that imprinting the ponderomotive phase shift (up to 980 radians) can lead to an observable change at the detector plane.

Chapter 1.1 overviews state-of-the-art in ultrafast electron microscopy. Also, the longitudinal and transverse manipulation of the electron wave function in conventional and ultrafast electron microscopes is discussed. The motivation for having a light-based electron interaction in free space is described. Chapter 1.2 provides a general outlook of what to expect in the following chapters.

1.1 Ultrafast electron miscroscopy

In conventional electron microscopy, information about a sample is extracted by scanning [Rei00, PN11] or transmitting [Rei13] the electrons through the sample. Depending on the specific application, the detector records electrons' elastic and/or inelastic scattering [BCE89]. For imaging techniques, the elastically scattered electrons are usually used, where the energy of the probe electrons remains unchanged. Contrary to elastic scattering experiments, spectroscopy techniques like electron energy loss spectroscopy (EELS) has been established to be a powerful tool for extracting elemental, chemical, or dielectric information about a sample [Ege11]. However, there are also selected applications where inelastically scattered electrons are used for imaging [KR85].

Ultrafast electron microscopy (UEM) has enabled the imaging of samples with high temporal (from 10 ns up to fs timescales) and spatial resolution providing unprecedented structural information in material science, chemistry, and biology [BYZ07, Zew10, MB18]. The so-called 'pump-probe' measurement technique is employed, where a pulsed laser (pump) is used to excite the sample, and a pulsed electron beam (probe) interacts with the excited sample at different time delays. Earlier versions of ultrafast transmission electron microscopes (UTEM) that were based on thermionic sources [LCR$^+$08, RLS$^+$10, BPC$^+$16] have been used to study solid state reactions, the martensitic transformation of nanocrystalline Ti and many other ultrafast processes none of which would have been possible to study using setups limited by the frame rate of the acquisition camera. Even though highly

performant for many applications, thermionic sources have planar photocathodes, which result in an electron emission area limited by the focal spot of the laser beam to several microns. To increase the electron beam coherence and hence unlock different phase-sensitive applications, UTEMs based on Schottky field emission guns (SFEG) [FBdS+17, ZZW+20] and cold field emission guns (CFEG) [HCW+18] have been developed. Some challenges lie in modifying the microscopes such that triggering the electrons is effective, interfacing the pump optics with the electron column, and synchronizing the two pulses in space and time. Also, ultrafast microscopes have found applications in studies of magnetization dynamics [dSMF+18] or skyrmion writing [BMM+18] which could be studied to improve data storage devices. Furthermore, ultrafast electron vortex beams have experimentally been created by interaction with strong, femtosecond, chiral, and plasmonic near fields [VBM+19]. More recently, time-resolved experiments in an ultrafast SEM have been carried out to study the hot carrier diffusion in semiconductors [CPH+22].

Moreover, it has been shown that the photon lifetime can be measured by studying the interaction between ultrafast electrons and cavity photons [WDS+20]. Additionally, the interaction of electrons with laser-triggered whispering gallery modes in a microsphere can lead to spectral electron broadening of up to 700 electron volts [KLMS+20]. A detailed study on the state-of-the-art shaping of electron beams with light can be found in [RK20].

Photon-induced near-field electron microscopy

Time-resolved methods involving femtosecond laser excitations are combined with EELS methods to study the ultrafast dynamics for phenomena occurring at the femtosecond scale. It has been shown in [BFZ09] that photon-induced near-field electron microscopy (PINEM) can image the near field of an electric field distribution close to a carbon nanotube or silver nanowire with femtosecond precision. First, the nanostructure is excited by an ultrafast laser. When an electron pulse is overlapped spatially and temporally at the excited nanostructure, direct absorption and emission of single photons are observed in the electron energy spectra. Secondly, when selecting the electrons that gained or lost energy, an image of the near field is formed. Also, PINEM enabled quantum walk of electrons [FES+15] and the generation of attosecond electron pulse trains [PRY+17].

Wavefront shaping of electron beams

The precise control over the wave function of a laser beam has been reached with the development of adaptive spatial light modulators. Programming and displaying on-demand diffractive optical elements that can arbitrarily shape the wave function led to tremendous progress in many optics applications [LHKO12]. Unfortunately, this degree of freedom has yet to be reached in electron microscopy. Programmable wavefront shaping of the electron phase has been realized by transmission of electron beams through holographic binary masks [VTS10, MAA+11, VBLL+13], magnetic [BVBVTV14, GBLM+17, TBM+18], electrostatic [VBMC+18, TRR+21, IBV22] and thin film material phase plates [UT10, GCGK+14, SLLA14, HPA+14, OCP+16, KRBD17, SRL+18, RSL+21a]. Many wavefront

shaping applications have been used for generating electron vortex beams carrying orbital angular momentum, creating self-healing beams, diffractive probe engineering, contrast enhancement in weak scattering objects, and aberration correction of electron beams. Although programmable (except thin films), most current wavefront shaping applications can suffer from losses, charging, inelastic scattering, and material deterioration.

The electron wave packet can also be shaped in free space by light in the vicinity of materials. It has been shown in [FYSR20] that a coherent inelastic beam splitter can be constructed if ultrafast electrons pass through laser-illuminated graphite sheets. Furthermore, attosecond coherent control has been demonstrated by probing electrons with semi-infinite light fields [VMB+18]. More recently, adaptive shaping was demonstrated by tunable photon induced spatial modulation [TDW+22]. Also, adaptive shaping with optical near field plates has been proposed [KcvdA20] for arbitrary wavefront-shaping of electron waves, whereas the first experimental demonstration followed shortly afterward [MLM+22].

Pondemorotive interactions

Even though it provides temporal and spatial control over the electron waves, optical manipulation of electron beams in the vicinity of materials can still suffer from charging, inelastic scattering, and beam-induced deterioration. The interaction of electrons and light in free space avoids these problems. It has been theoretically predicted by Kapitza and Dirac [KD33] that electrons could be diffracted from a standing optical wave. The interaction of electrons with a standing wave in free space has been theoretically studied further [Bar67, CT79], while the first experimental deflection of electrons was realized [BSB88] after the development of pulsed lasers, after some other attempts [BRT68, Sch73] that were inconclusive due to setup stability. Diffraction of electrons at a standing light wave and coherent phase shifting of electrons has been experimentally demonstrated [FAB01, FB02] afterward.

Moreover, Kapitza-Dirac experiments have found applications beyond electrons also in atom [GRP86] and molecular [GHH+07] physics. Also, the generation of electron vortex beams has been proposed, where the Kapitza-Dirac standing wave is replaced by optical waves carrying orbital angular momentum [HSB15] or via traveling waves by inelastic pondemorotive scattering [Koz21]. More recently, ponderomotive interactions have found applications in temporal characterization [SGHM05, HEH+06, HSH+08], attosecond generation and detection of electron pulses [KESH18, KO22, SCH22b]. Furthermore, attosecond electron pulses can be created by modulating the longitudinal and transverse momentum of the electron wave function using three different optical pulses overlapped with the electron pulse [Koz19]. Morever, light-based convex lensing with negative spherical aberrations [UKS21, UKS22] has been recently proposed for non-relativistic electrons.

In continuous wave mode, because the power requirements to induce ponderomotive phase shifts of $\pi/2$ are very high ($> 30\,000\,\mathrm{W}$), an optical enhancement cavity system that

features a standing wave has been proposed in [MJD+10] and successfully implemented in [SAC+19, ACS+20]. The continuous wave experiments have been carried out in a modified phase contrast TEM, where an image's contrast is enhanced by phase shifting $(\pi/2)$ the scattered wave with respect to the unscattered wave.

1.2 Structure of the thesis

Chapter 2, Theoretical background, provides the necessary steps to calculate the phase shift that relativistic electron waves experience when traversing a shaped high-intensity laser beam. The equation that describes how the state of a relativistic electron in an electromagnetic field evolves time is the Dirac equation [Mes14]. However, getting an analytical expression for the phase shift directly from the Dirac equation is challenging. It has been recently shown in [GdAKcv21] that the Dirac equation can be reduced to an effective Schrödinger equation. Thus, the phase shift can be calculated by integrating over the interaction Hamiltonian of the effective Schrödinger equation. Furthermore, in the derivation of the phase shift we neglect electron spin, single-photon processes, and energy spread of electrons, and we assume that the interaction takes place within the focal plane of the laser. We eventually arrive at an analytical expression for the phase shift that is proportional to the spatial transverse profile of the laser beam.

Chapter 3, Experimental Setup, describes the methods used to achieve light-induced transverse phase modulation of electron waves. We first discuss the environmental requirements regarding stray fields and mechanical vibrations and explain how we could realize them experimentally. We then describe how we modified the scanning electron microscope (SEM) to install the required optics that ensure a collinear interaction between electron and laser pulses. Finally, we discuss how we implemented the position-sensitive detector that consists of a microchannel plate (MCP) assembly.

Chapter 4, Wavefront Shaping of the Laser Beam, discusses our technique in shaping laser focal spots into speckle-free arbitrary intensity patterns. Laser beam shaping is done by displaying the required diffractive phase mask on a spatial light modulator (SLM). The phase masks are programmed using a modified Gerchberg-Saxton algorithm (GSA) that minimizes losses along the laser beam path. Furthermore, the aberrations of the laser focal spot have been corrected by superimposing various Zernike phase patterns to the calculated phase mask.

Chapter 5, Spatial and temporal overlap between the electrons and light pulses without an energy filter, explains the innovative method used to synchronize the electron and laser pulses in the interaction plane. Establishing the spatial and temporal overlap between ultrashort electron and laser pulses is challenging and requires a step-wise course of action. Synchronizing the pulses is not easy because, unlike photons, the electrons do not travel with constant velocity throughout the microscope column, which eventually could lead to timing uncertainties of nanoseconds. This error might be minimized if the

distances between the electrodes that accelerate the electrons are known; however, we did not have that information. Another error comes from the difficulties in measuring the propagation length of electrons. Note that 1 cm in path length error for 30 keV electrons already leads to an error of 30 ps. To avoid all these problems, we describe the methods used to trace back the precise arrival time of electrons and light in the interaction plane.

Chapter 6, Transverse Phase Modulation of Electron-waves using Light, represents the central part of my thesis and concentrates on the experimental results obtained by interacting a counter-propagating, spatially shaped laser pulse with a converging electron pulse. It is experimentally shown that arbitrary, light-induced electron phase modulation can lead to controllable transverse intensity modulation of electron beams. Furthermore, both convex and concave light-based electron lenses with focal lengths (a few mm) similar to those of state-of-the-art electro- and magnetostatic lenses are created. Note that concave lenses are impossible to create with static, cylindrically symmetric megnetostatic lenses. Electrostatic electron lenses can be made divergent, however, only if the electron energy is not preserved [WR01].

A future application of our light-based method is the aberration correction of electron beams. Chapter 7, Diagnosis of electron microscope aberrations, discusses the parameters that influence the shape of electron focal spot and the methods used to measure the aberrations. Furthermore, an electron Ronchigram is recorded in pulsed mode, which opens up possibilities of coherent wavefront-shaping. Also, various methods of achieving a laser intensity distribution that could correct the spherical aberrations of the electron beam are discussed.

Finally, Chapters 8 and 9 discuss the results presented in this thesis and the outlook for future research on transverse phase modulation of electron beams with light.

2 Theoretical background

2.1 Relativistic quantum description of the electron in an electromagnetic field

The following literature has been used to write the current chapter: [Sha12, Zwi22]. This chapter aims to derive an equation that describes how relativistic electrons are affected by strong electromagnetic fields. We start by giving a short introduction to classical electrodynamics to make the connection between electromagnetic fields and potentials. We then briefly describe why the Schrödinger and Klein-Gordon equations are not suited for calculating the evolution of spin-half particles and recall the Pauli and Dirac equations.

2.1.1 Electric and magnetic fields expressed as potentials

The Maxwell equations are partial differential equations that form the basis of classical electrodynamics and optics and describe the behaviour of the electric and magnetic field ($\boldsymbol{E} \equiv \boldsymbol{E}(\boldsymbol{r}, t)$ and $\boldsymbol{B} \equiv \boldsymbol{B}(\boldsymbol{r}, t)$). In quantum mechanics, a description using potentials is often more practical.

The second equation is the Gauss law for magnetism and tells us that there are no magnetic monopoles:

$$\nabla \cdot \boldsymbol{B} = 0. \tag{2.1}$$

The magnetic field $\boldsymbol{B}$ from Eq. 2.1 can be written in terms of the vector potential $\boldsymbol{A} \equiv \boldsymbol{A}(\boldsymbol{r}, t)$:

$$\boldsymbol{B} = \nabla \times \boldsymbol{A}. \tag{2.2}$$

The third equation is Faraday's induction law, which says that a spatially varying electric field results in a time-varying magnetic field:

$$\nabla \times \boldsymbol{E} = -\frac{1}{c}\frac{\partial \boldsymbol{B}}{\partial t}. \tag{2.3}$$

We now use the Eq. 2.2 and rewrite Eq. 2.3:

$$\nabla \times (\boldsymbol{E} + \frac{1}{c}\frac{\partial \boldsymbol{A}}{\partial t}) = 0. \tag{2.4}$$

Since the curl of the gradient of a scalar is zero, it is possible to introduce the scalar potential $\boldsymbol{\Phi} \equiv \boldsymbol{\Phi}(\boldsymbol{r}, t)$:

$$\nabla \times (-\nabla \boldsymbol{\Phi}) = 0. \tag{2.5}$$

We set Eq. 2.4 equal to Eq. 2.5 and rewrite the electric field in terms of potentials:

$$\boldsymbol{E} = -\nabla \boldsymbol{\Phi} - \frac{1}{c}\frac{\partial \boldsymbol{A}}{\partial t}. \tag{2.6}$$

2.1.2 Schrödinger and Klein-Gordon equation of a relativistic charged particle in an electromagnetic field

The Schrödinger equation describes how a wavefunction evolves in time and is defined as:

$$\hat{E}\Psi = \hat{H}\Psi, \tag{2.7}$$

with $\hat{E}$ the energy operator and $\hat{H}$ the Hamiltonian. However, the Schrödinger equation is inconsistent with special relativity. From the Einstein relation we have:

$$\hat{H} = \sqrt{\hat{\boldsymbol{p}}^2 c^2 + m^2 c^4}, \tag{2.8}$$

with $\hat{\boldsymbol{p}}$ the momentum operator. To couple the charged particle to the electromagnetic field, the scalar potential is added directly to the Hamiltonian, and the vector potential enters via the so called 'minimal coupling':

$$\hat{\boldsymbol{p}} \rightarrow \hat{\boldsymbol{\pi}} = \hat{\boldsymbol{p}} - \frac{q}{c}\boldsymbol{A}, \tag{2.9}$$

where q is the elementary charge and $\hat{\boldsymbol{\pi}}$ the canonical momentum operator. The Hamiltonian for a relativistic charged particle in an electromagnetic field becomes:

$$\hat{H} = \sqrt{\left(\hat{\boldsymbol{p}} - \frac{q\boldsymbol{A}}{c}\right)^2 c^2 + m^2 c^4} + q\Phi. \tag{2.10}$$

Now if we substitute:

$$\hat{\boldsymbol{p}} \rightarrow -i\hbar\nabla, \tag{2.11}$$

$$\hat{E} \rightarrow i\hbar\frac{\partial}{\partial t}, \tag{2.12}$$

into Eq. 2.7, we get the following equation:

$$i\hbar\frac{\partial \Psi}{\partial t} = [\sqrt{\left(-i\hbar\nabla - \frac{q\boldsymbol{A}}{c}\right)^2 c^2 + m^2 c^4} + q\Phi]\Psi. \tag{2.13}$$

Rewriting Eq. 2.13 yields the Klein-Gordon equation 2.14 of a spinless particle in an electromagnetic field. However, Ψ is scalar and cannot describe the state of an electron:

$$(i\hbar\frac{\partial}{\partial t} - q\Phi)^2\Psi = \left(-i\hbar\nabla - \frac{q\boldsymbol{A}}{c}\right)^2 c^2\Psi + m^2 c^4\Psi. \tag{2.14}$$

2.1.3 The Pauli Equation for an electron in an electromagnetic field

When charged particles with spin one-half couple to electromagnetic fields, the correct description for the Hamiltonian in the nonrelativistic case has been found by Pauli. The equation that describes a free spin one-half particle is:

$$i\hbar\frac{\partial\chi}{\partial t} = \frac{\hat{\boldsymbol{p}}^2}{2m}\mathrm{I}_{2\mathrm{x}2}\chi, \tag{2.15}$$

where $\chi = (\chi_1, \chi_2)$ is a column vector (Pauli spinor) that accounts for the two degrees of freedom of the spin one-half particle, and $\mathrm{I}_{2\mathrm{x}2}$ is the identity matrix. Next, we rewrite the Hamiltonian by using the identity:

$$(\boldsymbol{\sigma}\cdot\hat{\boldsymbol{p}})(\boldsymbol{\sigma}\cdot\hat{\boldsymbol{p}}) = \hat{\boldsymbol{p}}^2\mathrm{I}_{2\mathrm{x}2} + i\boldsymbol{\sigma}(\hat{\boldsymbol{p}}\times\hat{\boldsymbol{p}}), \tag{2.16}$$

with $\boldsymbol{\sigma} = \sigma_x\hat{x} + \sigma_y\hat{y} + \sigma_z\hat{z}$ the unit vectors with the Pauli matrices:

$$\sigma_x = \begin{pmatrix} 0 & 1 \\ 1 & 0 \end{pmatrix}$$

$$\sigma_y = \begin{pmatrix} 0 & -i \\ i & 0 \end{pmatrix}$$

$$\sigma_z = \begin{pmatrix} 1 & 0 \\ 0 & -1 \end{pmatrix}$$

Since the cross product $\hat{\boldsymbol{p}}\times\hat{\boldsymbol{p}} = 0$, the Hamiltonian takes the following form:

$$\hat{H} = \frac{\hat{\boldsymbol{p}}^2}{2m}\mathrm{I}_{2\mathrm{x}2} = \frac{(\boldsymbol{\sigma}\cdot\hat{\boldsymbol{p}})(\boldsymbol{\sigma}\cdot\hat{\boldsymbol{p}})}{2m}. \tag{2.17}$$

We now couple the charged particle to electromagnetism by replacing the momentum operator with the canonical momentum, and include the scalar potential:

$$\begin{aligned} \hat{H}_{\mathrm{Pauli}} &= \frac{1}{2m}(\boldsymbol{\sigma}\cdot\hat{\boldsymbol{\pi}})(\boldsymbol{\sigma}\cdot\hat{\boldsymbol{\pi}}) + q\Phi \\ &= \frac{1}{2m}(\hat{\boldsymbol{\pi}}\cdot\hat{\boldsymbol{\pi}})\mathrm{I}_{2\mathrm{x}2} + i\boldsymbol{\sigma}(\hat{\boldsymbol{\pi}}\times\hat{\boldsymbol{\pi}}) + q\Phi. \end{aligned} \tag{2.18}$$

Note that $\hat{\boldsymbol{\pi}}\times\hat{\boldsymbol{\pi}} \neq 0$ does not commute. Evaluating the cross product of the canonical momentum (see [Zwi22] for details), and replacing $m = m_e$ and $q = -e$, we arrive at:

$$\hat{H} = \frac{1}{2m_e}(\hat{\boldsymbol{p}} + \frac{e}{c}\boldsymbol{A})^2\mathrm{I}_{2\mathrm{x}2} + \frac{e\hbar}{2m_e c}\boldsymbol{\sigma}\boldsymbol{B} - e\Phi. \tag{2.19}$$

The spin coupling to the magnetic field can be read from the second term in Eq. 2.19. However, the Pauli equation is valid only in the nonrelativistic limit. Thus, we have to include relativity for a complete description.

2.1.4 The Dirac equation

The Dirac equation for a free particle

Following on [Sha12], Dirac managed to get rid of the square root from Eq. 2.8. To get rid of the square root, we need to rewrite the arguments under the square root such that they are equal to something squared.

$$\begin{aligned} c^2\hat{\boldsymbol{p}}^2 + m^2c^4 &= \left(c\boldsymbol{\alpha_d}\cdot\hat{\boldsymbol{p}} + \boldsymbol{\beta_d}mc^2\right)^2 \\ &= \left(c\alpha_x p_x + c\alpha_y p_y + c\alpha_z p_z + \boldsymbol{\beta_d}mc^2\right)^2 \end{aligned} \tag{2.20}$$

In order for Eq. 2.20 to hold, one needs to enforce some properties on $\boldsymbol{\alpha_d}$ and $\boldsymbol{\beta_d}$. The first condition requires:

$$\alpha_x^2 = \alpha_y^2 = \alpha_z^2 = \boldsymbol{\beta_d}^2 = 1. \tag{2.21}$$

The second condition requires that the dot products vanish:

$$\alpha_i\alpha_j + \alpha_j\alpha_i = 0 \quad \text{for all} \quad i \neq j, \tag{2.22}$$

$$\alpha_i\boldsymbol{\beta_d} + \boldsymbol{\beta_d}\alpha_i = 0 \quad \text{for all} \quad i. \tag{2.23}$$

Finally, $\boldsymbol{\alpha_d}$ and $\boldsymbol{\beta_d}$ need to be matrices, whereas 4x4 matrices give the simplest solution. The Dirac equation in free space takes the following form:

$$i\hbar\frac{\partial\psi}{\partial t} = \left(c\boldsymbol{\alpha_d}\cdot\hat{\boldsymbol{p}} + \boldsymbol{\beta_d}mc^2\right)\psi \tag{2.24}$$

where $\boldsymbol{\alpha_d}$ and $\boldsymbol{\beta_d}$ are the Dirac matrices:

$$\boldsymbol{\beta_d} = \begin{bmatrix} \mathrm{I}_{2\mathrm{x}2} & 0 \\ 0 & -\mathrm{I}_{2\mathrm{x}2} \end{bmatrix}, \quad \boldsymbol{\alpha_d} = \begin{bmatrix} 0 & \boldsymbol{\sigma} \\ \boldsymbol{\sigma} & 0 \end{bmatrix}, \tag{2.25}$$

Note the wavefunction is changed from the Pauli spinor to a four-component column spinor (see Appendix E in [CMWS+22]), which adds to the complexitity of finding an analytical solution for an electron.

The Dirac equation for a particle in an electromagnetic field

Coupling in the potentials in 2.24 will lead to:

$$[m_e c\boldsymbol{\beta_d} + c\boldsymbol{\alpha_d}(\hat{\boldsymbol{p}} + \frac{e}{c}\mathbf{A}) - e\Phi]\Psi = i\hbar\frac{\partial\Psi}{\partial t}, \tag{2.26}$$

The Dirac Hamiltonian for a relativistic charged particle coupled to the electromagnetic field takes the following form:

$$\hat{H}_{Dirac} = m_e c\boldsymbol{\beta_d} + c\boldsymbol{\alpha_d}(\hat{\boldsymbol{p}} + \frac{e}{c}\mathbf{A}) - e\Phi. \tag{2.27}$$

2.2 Ponderomotive interaction for a relativistic charged particle

Most studies of electron-light interactions consider the perpendicular interaction between electrons and a standing light wave, also known as the Kapitza-Dirac effect. In our setup, we have an intense traveling light wave propagating in the opposite direction to relativistic electrons. This sub-chapter aims to arrive at an analytical solution that allows us to calculate the electron's phase shift induced by arbitrary light distributions. The following part of this sub-chapter is reprinted from our publication [CMWS+22].

We derive the light-induced phase modulation of a relativistic electron beam in free space, using SI units throughout. We define the direction of propagation to be the z-axis and assume the electron waves travel at a relativistic mean velocity $\boldsymbol{v} = v\boldsymbol{e_z}$, which sets the Lorentz factor as $\gamma = 1/\sqrt{1 - v^2/c^2}$ and the energy as $E_e = \gamma m_e c^2$. In such a setting, the electron wavefunction ψ can be factorized into the rapidly oscillating plane-wave component at E_e and a slowly varying envelope $\psi_\perp$ that accounts for the transverse wave profile,

$$\psi(\boldsymbol{r}, t) = \psi_\perp(\boldsymbol{r}, t) e^{i\gamma m_e (vz - c^2 t)/\hbar}. \tag{2.28}$$

Assuming that light-induced variations of the electron energy be small compared to the initial energy E_e (called non-recoil approximation), it is shown in [GdAKcv21] that the Dirac equation 2.26 for the electron state reduces to the effective Schrödinger equation

$$(\partial_t + \boldsymbol{v} \cdot \nabla)\psi_\perp(\boldsymbol{r}, t) = -\frac{i}{\hbar} U(\boldsymbol{r}, t)\psi_\perp(\boldsymbol{r}, t), \tag{2.29}$$

with the effective interaction potential

$$\begin{aligned} U(\boldsymbol{r}, t) &= \frac{e^2}{2m_e\gamma}\left[A_x^2(\boldsymbol{r}, t) + A_y^2(\boldsymbol{r}, t) + \frac{1}{\gamma^2}A_z^2(\boldsymbol{r}, t)\right] \\ &\quad + e\boldsymbol{v} \cdot \boldsymbol{A}(\boldsymbol{r}, t) - e\boldsymbol{\Phi}(\boldsymbol{r}, t). \end{aligned} \tag{2.30}$$

By integrating Eq. (2.29), we find that the evolution of the state $\psi_\perp$ between two times t_0 and t_1 can be expressed as

$$\begin{aligned} \psi_\perp(\boldsymbol{r} + \boldsymbol{v}t_1, t_1) &= \psi_\perp(\boldsymbol{r} + \boldsymbol{v}t_0, t_0) \\ &\quad \times \exp\left[-\frac{i}{\hbar}\int_{t_0}^{t_1} dt'\, U(\boldsymbol{r} + \boldsymbol{v}t', t')\right]. \end{aligned} \tag{2.31}$$

The free propagation amounts to a position shift while the light field contributes an additional phase modulation. In fact, if we choose a sufficiently large interval $(t_0, t_1) \to (-\infty, \infty)$ that covers the whole duration of the electron-light interaction, Eq. (2.31) can be understood as the instantaneous scattering transformation from the incoming to the outgoing electron wave evaluated at the same time,

$$\psi_\perp^{(\mathrm{out})}(\boldsymbol{r}, t) = e^{i\varphi(\boldsymbol{r})}\psi_\perp^{(\mathrm{in})}(\boldsymbol{r}, t), \tag{2.32}$$

with the scattering phase $\varphi(\boldsymbol{r}) = -\int dt'\, U(\boldsymbol{r} + \boldsymbol{v}t', t')/\hbar$. The time coordinate t marks the scattering event, i.e. the point in time when the electron wave packet hits the light pulse.

Regarding the interaction potential from Eq. (2.30), notice that we may fix the gauge such that $\boldsymbol{\Phi} = 0$ and we can safely neglect the term $\boldsymbol{v} \cdot \boldsymbol{A}$ as we integrate the optical field over a pulse length of 10^2 periods [GdAKcv21]. Hence we may omit the respective terms in U.

Given a paraxial light pulse (as focused by moderate numerical apertures) with central frequency ω_L that propagates in the $\pm z$-direction and is linearly polarized along x, the associated complex-valued electric field can be written as

$$\boldsymbol{E}(r,t) = \mathcal{E}_0 \boldsymbol{e_x} g(x,y) e^{-i\omega_L(t \mp z/c)} u\left(t \mp \frac{z}{c}\right), \tag{2.33}$$

with $\mathcal{E}_0$ the characteristic field strength, $g(x,y)$ the transverse mode profile, and $u(t)$ the temporal pulse envelope. For simplicity, these three terms are taken to be real-valued in the following. The real-valued vector potential in Eq. (2.30) is related to the physical field amplitude via $-\partial_t \boldsymbol{A}(\boldsymbol{r},t) = \Re\{\boldsymbol{E}(\boldsymbol{r},t)\}$.

For the temporal pulse width considered here ($\Delta t = 280\,\mathrm{fs}$), the envelope $u(t)$ varies on much greater time scales than the optical oscillation period ($2\pi/\omega_L = 3.5\,\mathrm{fs}$), which allows us to write the vector potential to leading order as

$$\begin{aligned} \boldsymbol{A}(\boldsymbol{r},t) &= \Re\left\{\frac{\boldsymbol{E}(\boldsymbol{r},t)}{i\omega_L}\right\} \\ &= -\frac{\mathcal{E}_0 \boldsymbol{e_x}}{\omega_L} g(x,y) \sin\left[\omega_L\left(t \mp \frac{z}{c}\right)\right] u\left(t \mp \frac{z}{c}\right) \end{aligned} \tag{2.34}$$

Plugging this into Eq. (2.30), the scattering phase becomes

$$\begin{aligned} \varphi_v(\boldsymbol{r}) &= -\frac{e^2\mathcal{E}_0^2 g^2(x,y)}{2m_e\gamma\hbar\omega_L^2} \int dt'\, u^2\left(t' \mp \frac{z+vt'}{c}\right) \\ &\quad \times \sin^2\left[\omega_L\left(t' \mp \frac{z+vt'}{c}\right)\right] \\ &= -\frac{e^2\mathcal{E}_0^2 g^2(x,y)}{2m_e\gamma\hbar\omega_L^2(1 \mp \beta)} \int dt\, u^2(t) \sin^2(\omega_L t). \end{aligned} \tag{2.35}$$

In the last line, we substitute $t' \mp (z+vt')/c \to t$ and introduce $\beta = v/c$. As a next step, we can write $\sin^2(\omega_L t) = [1 - \cos(2\omega_L t)]/2$ and neglect the integral over $u^2(t)\cos(2\omega_L t)$ due to the slowly varying pulse envelope, which leaves us with the ponderomotive scattering phase averaged over the fast optical oscillation,

$$\varphi_v(x,y) \approx -\frac{e^2\mathcal{E}_0^2 g^2(x,y)}{4m_e\gamma\hbar\omega_L^2(1 \mp \beta)} \int dt\, u^2(t). \tag{2.36}$$

Notice that the phase no longer depends on the z-coordinate, which is consistent with the paraxial regime for both light and electron waves.

Finally, we can express the laser field amplitude in terms of a more directly accessible parameter. To this end, consider the field energy flowing through the xy-plane per unit area and time, as described by the Poynting vector $\boldsymbol{S} = \Re\{\boldsymbol{E}\} \times \Re\{\boldsymbol{H}\}$ with $\boldsymbol{H} = c\varepsilon_0 \boldsymbol{e_z} \times \boldsymbol{E}$ to leading order. The measured laser pulse energy E_L is obtained by taking the integral of $|\boldsymbol{S}|$ over the plane and over time, which leads to

$$\begin{aligned} E_L &= c\varepsilon_0 \mathcal{E}_0^2 \int dt\, u^2(t) \cos^2(\omega_L t) \int dxdy\, g^2(x,y) \\ &\approx \frac{c\varepsilon_0}{2} \mathcal{E}_0^2 \int dt\, u^2(t) \int dxdy\, g^2(x,y), \end{aligned} \tag{2.37}$$

assuming once again a slow temporal pulse profile. We can now eliminate this profile and the field strength in the ponderomotive phase (Eq. (2.36)) and simplify

$$\boxed{\varphi_v(x,y) = -\frac{\alpha}{2\pi(1 \mp \beta)} \frac{E_L}{E_e} \frac{\lambda_L^2 g^2(x,y)}{\int dxdy\, g^2(x,y)}}, \tag{2.38}$$

where α is the fine structure constant and $\lambda_L = 2\pi c/\omega_L$ the pulse wavelength. The transverse light beam profile $g^2(x,y)$ is divided by its integral and can thus be given in arbitrary units. Moreover, the phase is Lorentz covariant since it reads the same in the electron rest frame where $\beta' = 0$, $E'_e = m_e c^2$, $\lambda'_L = \lambda_L \sqrt{(1 \pm \beta)/(1 \mp \beta)}$, and $E'_L = E_L \sqrt{(1 \mp \beta)/(1 \pm \beta)}$.

For a Gaussian laser beam, Eq. 2.38 takes the following form:

$$\varphi_v(x,y) = -\frac{\alpha}{2\pi(1 \mp \beta)} \frac{E_L}{E_e} \lambda_L^2 \frac{e^{-(\frac{2x^2}{w_{00}^2} + \frac{2y^2}{w_{00}^2})}}{\pi w_{00}^2}, \tag{2.39}$$

where w_{00} is the Gaussian beam waist. In order for an electron at 30 keV to acquire a phaseshift of $\pi/2$ when traversing the center of a counter-propagating Gaussian laser focus with $w_{00} = 3.65\,\mu$m, a laser pulse energy of 30 pJ is required.

3 Experimental Setup

The Experiments are being conducted in a modified scanning electron microscope (SEM, FEI XL30). A custom has replaced the SEM's original door (see Fig. 3.1(left)), which allows us to mount the required optical setup directly underneath the objective lens of the SEM. In addition, a hole was cut into the bottom of the sample chamber so that we could operate the setup in transmission mode. To achieve the required high laser peak intensities for ponderomotive scattering, an ultrafast infrared laser (coherent Monaco) has been employed ($\lambda = 1035\,\mathrm{nm}$, repetition rate 1 Mhz, pulse length 280 fs, pulse energy $<40\,\mu\mathrm{J}$).

Figure 3.1 describes the experimental setup: the laser beam is split into two arms by a beam splitter (93/7). The less intense part of the laser beam is used to generate the fourth harmonic (258 nm) by using two nonlinear β-barium borate (BBO) crystals as follows: the infrared laser goes through a BBO crystal (EKSMA Optics, 6x6x3 mm, $\theta = 23.4$). The resulting output is a mixture of IR laser (1035 nm) and green laser (515 nm). The green laser beam is filtered out by a dichroic mirror and guided towards the second crystal (EKSMA Optics, 6x6x0.5 mm, $\theta = 49.6$), which is used to generate the ultraviolet (UV) light (258 nm). The resulting UV laser beam is filtered out from the green light and finally focussed by a 15 cm focal length lens on the Schottky gun of the electron microscope [HSATK06]. This generates pulsed electrons, which propagate in the z-direction towards a counter-propagating, spatially shaped laser focus.

The intense part of the IR laser ($<17.2\,\mu\mathrm{J}$) is used to generate the required field amplitudes for the ponderomotive scattering experiments. First, the IR beam goes through a delay stage that allows adjusting the timing with respect to the electron pulse. Second, the laser beam is transferred from the initial optical table to the electron microscope table (see Fig. 3.2). Both IR and UV laser beams pass through a beam stabilization system (Aligna, TEM-Messtechnik) equipped with two piezo actuators. One actuator is placed on the optical initial optical table and the other one is placed on the electron microscope table. This is used to counteract the pointing instabilities ($25\,\mu\mathrm{rad}$) of the laser, mechanical/thermal vibrations and drifts within the beam path. In addition, it makes the experiment easier to operate because it realigns the laser beams at the beginning of a new experiment. Third, the IR laser is expanded to a diameter ($1/e^2$) of 7.5 mm and is diffracted from the SLM phase mask, forming the first shaped intensity distribution in the focal plane of a lens (of focal length $f = 200\,\mathrm{mm}$). The shaped distribution is further demagnified 5x by a 4f system (250mm lens and 50 mm lens) and is brought to the interaction plane by a gold mirror on a copper substrate to interact with the counter-propagating electron pulse (see Fig. 3.4). A 1.5 mm hole is drilled in the gold

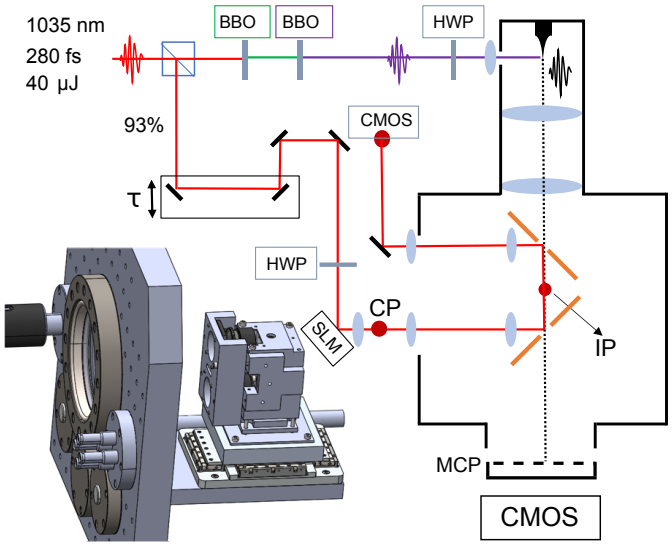


Figure 3.1: Experimental setup: Programmable ponderomotive deflection of electrons in free space. Outside the vacuum chamber, the SLM-shaped laser distribution is formed in the conjugate plane (CP). In the specimen chamber, the electron beam interacts with a counter-propagating laser pulse in the IP. The induced electron phase modulations are proportional to the local laser pulse energy. (left) The modified SEM chamber door (bottom, left) allows for in and outcoupling the shaped light fields. Reprinted from [CMWS+22].

mirror to allow the electrons to pass through. After the interaction, the laser beam is outcoupled from the SEM chamber and used further for alignment purposes. Both UV and IR power levels are independently controlled by placing motorized polarizing beam splitters along their beam paths.

3.1 Noise sources in the SEM region

Two primary noise sources identified in our lab can cause decoherence in the electron beam and degradation of the instrument resolution. One noise source is related to stray electromagnetic fields in the microscope region, and the other comes from mechanical vibrations that couple to the SEM column. One of the requirements for achieving a good resolution in electron microscopes is to have stray electromagnetic fields below 0.1 mG root mean square [MG01]. Active shielding uses a magnetic field compensation system (Stefan Meyer Instruments) to tackle the stray magnetic fields issue. Vibrations that couple to the SEM column are reduced passively. The SEM table legs are placed directly on the concrete floor (instead of on the laboratory flooring), and the SEM itself is placed on an air-damped table. We found that the air-damped table's pressure must be set carefully to about ~ 5 bar to optimize its damping behavior.

3.2 The procedure of creating the pulsed electron beam

The alignment procedure of the UV laser beam at the electron gun [KMS+18] is done by first heating the tip to a temperature (T>1500 K) such that the naked eye can see the black body radiation emitted in the visible spectrum. We first align the radiated light to pass through the center of two irises placed at ~ 1 m distance from each other. The light intensity that passes through the irises is optimized by detecting the signal with a CMOS camera (FLIR, BFS-U3-50S5). Afterward, we align the UV laser beam to the same two irises. Finally, the precise position of the UV focal spot at the electron gun is tuned by optimizing the electron intensity detected at the MCP assembly. The sensitivity of the fine alignment can be increased by using higher laser pulse energies up to ~ 10 nJ, optimizing the lens position, removing the aperture of the SEM objective lens, focussing the electron beam to a small (<1 mm) spot at the detector plane, biasing the MCP assembly to be sensitive to single electrons. Note that the electrons are triggered only when the focal point is precisely at the tip of the electron gun. Furthermore, the exposure time of the CMOS is set to ~ 0.2 s.

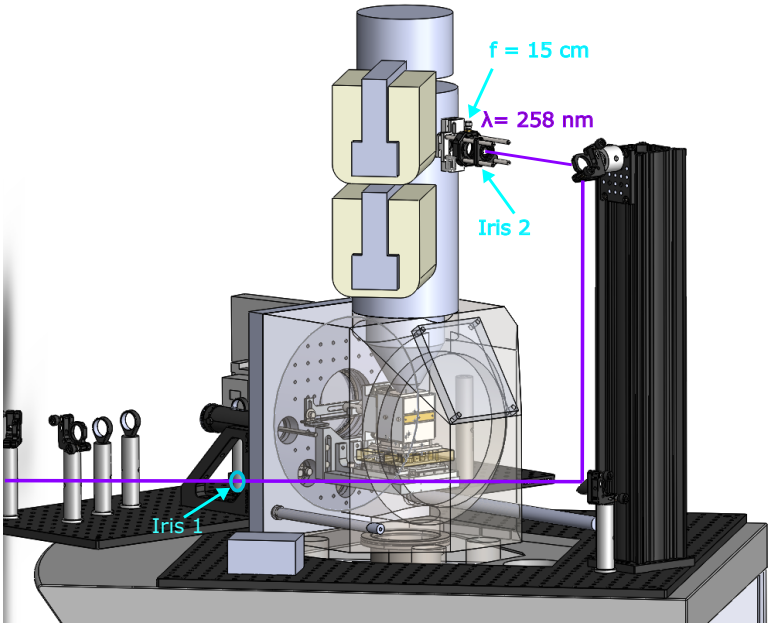


Figure 3.2: Experimental setup (back view). The UV light is brought to the electron gun height level with two mirrors attached to a vertical support rail (Thorlabs, CFB1500). Furthermore, a cage system is mounted directly on the SEM column and holds the focussing lens and an iris used for alignment. The UV laser beam hits the electron gun laterally through a window and triggers the ultrashort electron pulses. 3D drawing made by Philipp Weber. I only designed the 3D drawing of the optical setup outside vacuum.

Thus, the risk of missing the triggering event when changing the position of the UV

laser beam by the mirror close to Iris 2 (see Fig.3.2) is minimized. The polarization of the UV laser is aligned parallel to the Schottky gun to maximize the electron emission [HSATK06]. Figure 3.2 shows the back view of the electron microscope.

3.3 Electron detection system

The electrons are detected using a microchannel plate assembly (Tectra Gmbh, MCP-025-D-L-F-V-P43-6MI). The assembly is in vacuum and consists of two MCPs (18.8 mm active area) with a channel diameter of 6 μm installed in a chevron configuration and read out by a phosphor screen (P43). The MCP is usually biased at 1300 V and the P43 at 3500 V. Due to the potential difference between the second MCP plate and the P43, the amplified electrons (gain $\sim 5\times10^6$, according to the datasheet [MCP]) at the MCP output start to accelerate towards the P43, where the deposited position-dependent energy is converted into light (peak wavelength of emission 545 nm). Finally, the scintillated light is collected by a lens (Kowa, LM35HC) that is attached to a CMOS (FLIR, GS3-U3-23S6M-C) camera (outside vacuum). The CMOS peak sensitivity matches the emission wavelength of the P43. The CMOS can detect single electron events with a finite resolution ($\sim$ 100 μm) determined by the measured point spread function (see Appendix C in [CMWS+22]). Also, the detected electron beam images were processed after the acquisition with a 2x2 median filter to avoid dead pixels from the CMOS. The schematic of the electron detection system can be seen in Fig. 3.3.

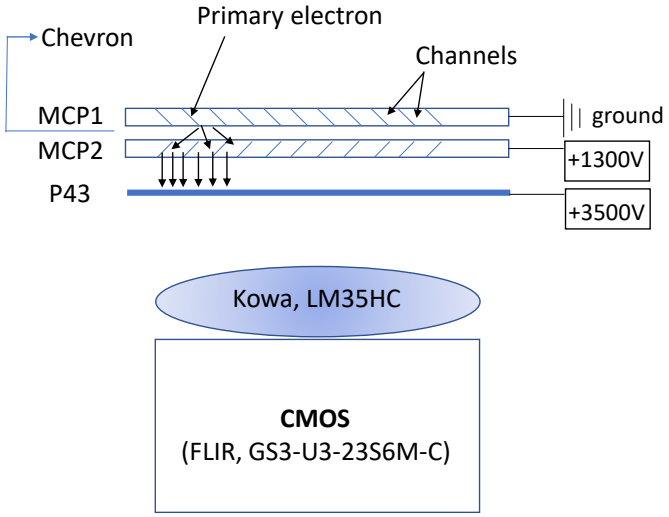


Figure 3.3: Electron detection system. Inside vacuum: a primary electron is impinging onto the first MCP disk triggering an electron avalanche. The electron signal is further amplified by a second MCP and eventually accelerated on the P43 screen. The scintillated light from the P43 is captured outside the vacuum by an objective lens coupled to a CMOS camera.

3.4 Optical setup

The original SEM door has been replaced by a custom one, which holds the optical components required to couple the light in and out of the vacuum chamber. The door is made of aluminum and has a CF 100 transparent window to allow light to enter and exit the vacuum chamber. In addition, it has multiple ports for electrical feedthroughs and threaded holes across the surface that would enable the optical components to be mounted directly to the door.

Figure 3.4(left) shows the SLM optics mounted on a breadboard outside the vacuum and attached directly to the SEM door by two Brackets (Thorlabs, VB01). Figure 3.4(right) features the optical setup inside the vacuum chamber that is also attached to the SEM door and brought close to the objective lens of the SEM. The whole structure is mounted on a 2D piezo stage to facilitate alignment with the electrons. The green and blue arrows indicate the position of the lenses and mirrors that couple in and out the laser beam. The mirrors have an unprotected gold layer on top of a copper substrate to avoid charging effects. Also, 1.5 mm holes are drilled into the mirrors to allow the electron beam to pass through. With everything set, the shaped IR laser beam enters the SEM chamber through the CF 100 window, modulates the electron beam in the interaction plane (see red spot in 3.4), and is afterward out-coupled from the chamber. Figure 3.5 shows a photograph of the experimental setup with the SLM optics mounted on a breadboard and attached to the custom-made SEM door.

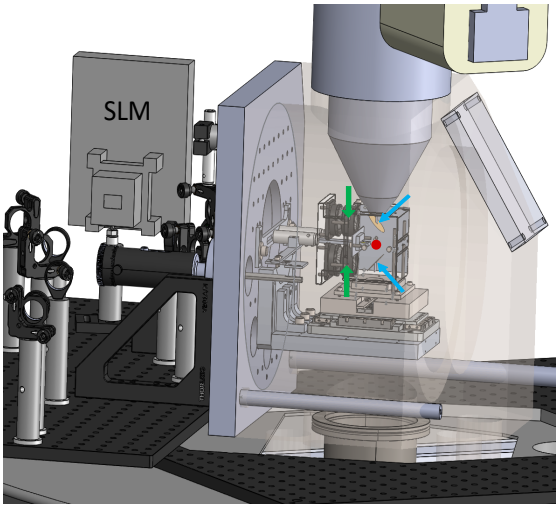


Figure 3.4: Experimental setup (3D drawing, side view). (left) The breadboard holds the SLM optics and is attached to the modified SEM door. (right) The optical setup inside the vacuum is placed close to the SEM objective lens. The whole structure is attached to the SEM door and features a 2D piezo stage to establish the alignment with the electron beam. The figure has been reprinted from [CMWS+22]. 3D drawing made together with Philipp Weber.

Additionally, a mechanical stage is installed to fit into the interaction region (see Fig. 3.6) in-between the lenses. This is particularly important for establishing the temporal and spatial overlap between the laser and electron pulses since it can host a scintillator, TEM grid, or a miniaturized CMOS camera.

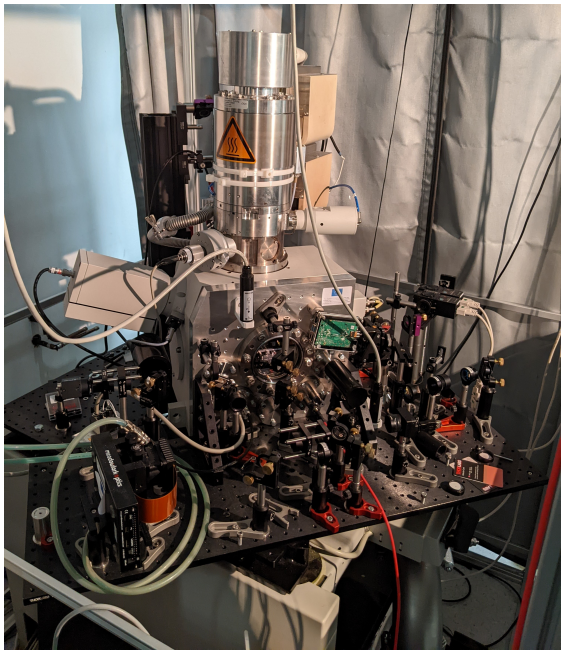


Figure 3.5: Experimental setup (front view). The modified SEM door holds the breadboard with the water-cooled SLM and the optical components.

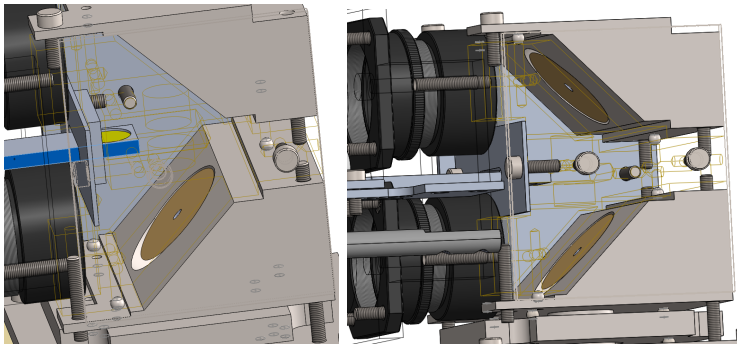


Figure 3.6: 3D drawing of the optical setup in the interaction region taken at different angles. The mechanical stage in-between the lenses with a scintillator (yellow) is marked in blue (left). The non-magnetic titanium components holding the gold mirrors can be seen on the right (top, and bottom). A 1.5 mm hole has been drilled in the 45° mirrors to allow the electron beam to pass through. 3D drawing is made by Philipp Weber.

4 Wavefront Shaping of the Laser Beam

4.1 Spatial Light Modulator

Spatial light modulators are devices that can modulate the properties (phase, amplitude, polarization [OMNA$^+$09]) of a laser beam [NAL90] as a function of position. In recent years, spatial light modulators have revolutionized the field of optics with applications in astronomy [KBB$^+$03], deep-tissue imaging [WLM$^+$14], two-photon imaging [NWA$^+$08] optical microscopy [MJBRM11b], aberration correction [Lov97, VMPA98, RDFB$^+$16], femtosecond pulse shaping [Wei00], exotic beams generation [CRC$^+$03, FDM16, MJF$^+$07], atom physics [MSM$^+$03] and many others [RDFB$^+$16].

We use a phase-only water-cooled SLM (Meadowlark optics [Mea22], 1920x1152 pixels, $9.2\,\mu\text{m}^2$ pixel size) based on individually programmable liquid crystal (LC) pixels. Incident polarized light enters the cover glass of the SLM and goes through a layer of LC pixels, is reflected afterward from the pixels electrodes, and leaves the device following the same path. The resulting wavefront acquires a phase shift from 0 to 2π depending on the orientation of the LCs, which can be independently controlled by the electric field between the cover glass and pixel electrode. Hence, the SLM is used as an adaptive diffractive optical element that can host arbitrarily programmable phase masks. Even though versatile, there are also some current issues with the SLMs. The SLMs have limited diffraction efficiency and respond only to linearly polarized light. Furthermore, the liquid crystals inside the SLM can be damaged if a specific peak intensity value is exceeded.

4.2 The Gerchberg Saxton algorithm (GSA)

Intensity distributions can be shaped by diffracting the light beam off a specific phase mask followed by light propagation in the far field [BW13]. For generating an arbitrary intensity distribution, iterative algorithms like the ones described in [Ger72] and [Fie82] can calculate the required phase mask. For our experiments, we use the GSA [Ger72] to calculate the needed phase of a complex wave in the space domain (hologram plane) that will generate the desired amplitude distribution after propagation to Fourier space (target plane). The phase retrieval algorithm is initiated with the desired amplitude in the target plane and then iteratively propagates the wave function to the hologram plane and back using Fourier transforms. In the hologram plane, the calculated amplitude of the wave function is replaced by the source amplitude, while in the target plane, the calculated amplitude is replaced by the desired amplitude. After several iterations, the algorithm

converges to a solution where the source amplitude and calculated phase in the hologram plane will yield the desired intensity distribution in the Fourier space.

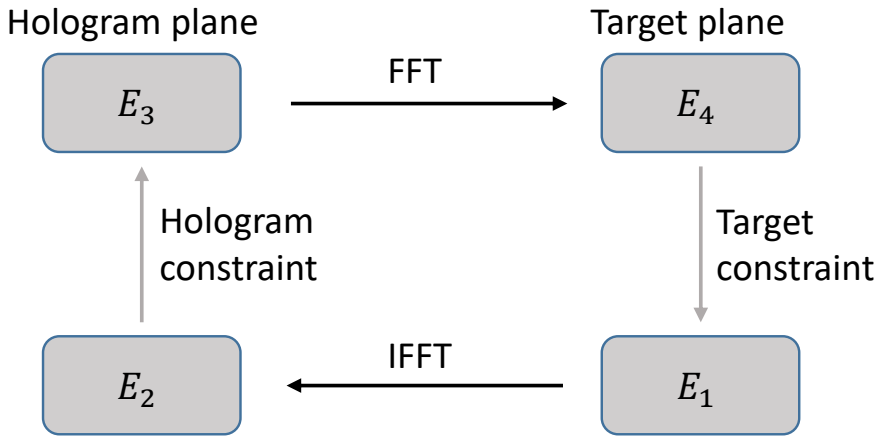


Figure 4.1: Schematic of the Gerchberg-Saxton algorithm. The algorithm is initiated in the target plane with desired electric (E_1) field amplitude and phase. The electric field is then propagated to the hologram plane with an IFFT function. Here, the hologram constraint is applied such that the amplitude of E_2 is replaced with the source amplitude, whereas the phase is kept. Further, the electric field E_3 is propagated to the target plane using an FFT function. Here the amplitude of E_4 is replaced by the desired amplitude while keeping the phase, and the iteration continues until the reconstructed amplitude in the target plane equals the desired amplitude.

4.3 Modified Gerchberg-Saxton algorithm

4.3.1 Inclusion of elements in the iterative algorithm with Fresnel propagation

In order to couple the laser beam to the electrons, 45° mirrors (CO2 laser mirrors, Thorlabs NB05-L01) are installed before and after the interaction plane. Small holes (1.5 mm) are drilled into the mirrors, such that the electron beam can pass through. A standard GSA would lead to significant light intensity impinging on those holes. This would cause a loss of light and heating within the vacuum chamber. We, therefore, implement a beam block in the GSA such that the iterative algorithm converges towards solutions with no light intensity on the hole. While the original algorithm is implemented using fast Fourier transforms, we are now using Fresnel transforms to be able to include additional elements into the algorithm if needed. The propagation algorithm has been written in Matlab and adapted from [Voe11].

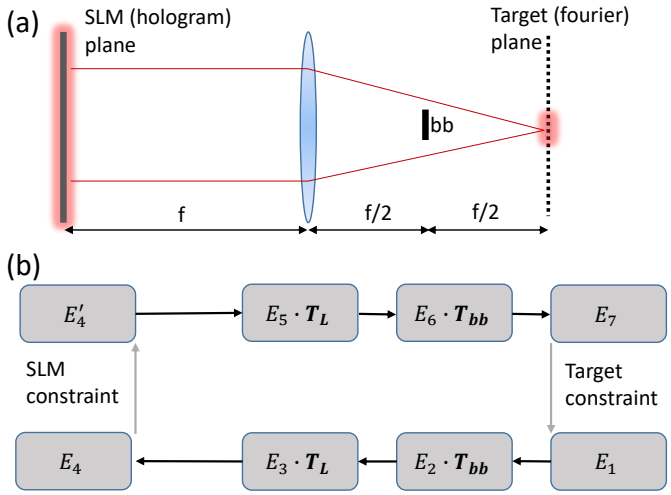


Figure 4.2: Reprinted from our paper [CMWS+22]. (a) Optical setup used to generate the desired laser intensity distribution. For the electrons to pass through the optical system, a 1.5 mm hole is drilled in the mirrors before and after the interaction plane. A beam block (bb) can be implemented in the algorithm to minimize the laser intensity losses at the hole and facilitate diffraction around it. (b) The schematic of the adapted iterative GSA. The Fresnel transfer function propagates the electric field from one plane to another. The Fresnel implementation allows for introducing additional elements, like the beam block, in the iterative algorithm.

The electric field of the laser in the plane j is characterized by the amplitude $A(x, y)$ and phase $\phi(x, y)$ distribution:

$$E_j(x, y) = A(x, y)e^{i\phi(x,y)}. \tag{4.1}$$

It is propagated to a plane $j+1$ by

$$E_{j+1}(x, y) = \mathcal{F}^{-1}[\mathcal{F}[E_j(x, y)\mathcal{T}(f_x, f_y)]], \tag{4.2}$$

where

$$\mathcal{T}(f_x, f_y) = e^{ikz} \exp(-i\pi\lambda_L z(f_x^2 + f_y^2)), \tag{4.3}$$

is the Fresnel transfer function and $\mathcal{F}$ is the Fourier transform operation, λ_L the light wavelength, z is the propagation distance and $k = 2\pi/\lambda_L$ the wavenumber. The spatial and frequency coordinates are discretized on a square grid with

$$x \to \frac{-L_x}{2} : \Delta x : \frac{L_x}{2} - \Delta x, \tag{4.4}$$

$$y \to \frac{-L_y}{2} : \Delta y : \frac{L_y}{2} - \Delta y, \tag{4.5}$$

$$f_x \rightarrow \frac{-1}{2\Delta x} : \frac{1}{L_x} : \frac{1}{2\Delta x} - \frac{1}{L_x}, \tag{4.6}$$

$$f_y \rightarrow \frac{-1}{2\Delta y} : \frac{1}{L_y} : \frac{1}{2\Delta y} - \frac{1}{L_y}, \tag{4.7}$$

with $L_x = N_x \Delta x$. The iterative algorithm starts in the Fourier plane by choosing the target amplitude and initial phase of the electric field $E_1 = E_1(x, y) = A_{\text{Target}}(x, y)e^{i\phi_{\text{initial}}(x,y)}$ (see Fig. 4.2). Second, the field propagates back for $z = -f/2$ and is (optionally) multiplied by the transmission function of the beam block (T_{bb}). Third, the field propagates for $z = -f/2$ and is multiplied by the transmission function of the lens (T_L). The transmission functions of the beam block and lens are defined as follows:

$$T_{\text{bb}} = \begin{cases} 1 & \text{for } \sqrt{x^2 + y^2} \geq 0.75\,\text{mm} \\ 0 & \text{for } \sqrt{x^2 + y^2} < 0.75\,\text{mm} \end{cases} \tag{4.8}$$

$$T_L(x, y) = T_p(x, y) \exp(\frac{-ik}{2f}(x^2 + y^2)), \tag{4.9}$$

$$T_p = \begin{cases} 1 & \text{for } \sqrt{x^2 + y^2} < 12.5\,\text{mm} \\ 0 & \text{for } \sqrt{x^2 + y^2} \geq 12.5\,\text{mm} \end{cases} \tag{4.10}$$

where T_p is the pupil function of the lens. Fourth, the field propagates for $z = -f$ to the hologram (SLM) plane, where the amplitude distribution is replaced by the source amplitude (Gaussian), which is defined as below:

$$A_{\text{source}} = \sqrt{\exp(-(\frac{2x^2}{\sigma^2} + \frac{2y^2}{\sigma^2}))}, \tag{4.11}$$

where σ is the beam waist defined where the amplitude has dropped to $1/e^2$. Afterward, the field propagates back to the target plane, following the same path. Note, that the sign of z is reversed when the electric field changes direction. The arriving field at the target plane is $E_7 = A_7 e^{i\phi_7(x,y)}$. If the resulting amplitude $A_7(x, y) \approx A_{\text{Target}}(x, y)$, the phase distribution of E_4 is extracted and used as the computer-generated hologram. Otherwise, the Fourier constraint is applied, and the iteration continues until the algorithm eventually converges.

Signal and Noise region of the laser's electric field

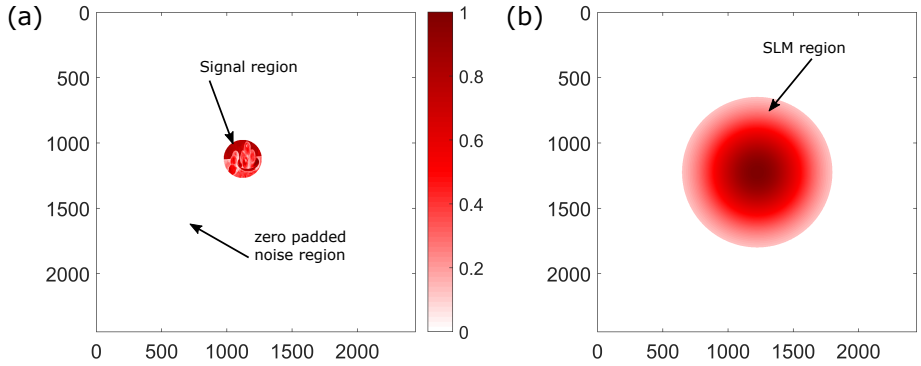


Figure 4.3: Regions of interest defined when using the modified GSA. (a) The off-centered intensity distribution of the target image ($|E_{\text{Target}}(x,y)|^2$) in the Fourier plane. The target image is intentionally off-centered to avoid interference with the unmodulated light. The Matrix I contains a signal region, where the target image is defined, and a noise region (zero padded) to maintain the sampling condition ($N_x = \lambda_L z/\Delta x^2$). (b) The Gaussian source intensity ($|A_{\text{source}}|^2$, $\sigma = 7.5\,\text{mm}$) is constrained within the dimensions of our SLM ($R_{SLM} = 5.3\,\text{mm}$).

For our applications, the target image is defined within a matrix window $I = |E(x,y)|^2$ that contains $N_x \times N_y$ pixels. The number of pixels in I is kept constant at $N_x = N_y = 2446$ to ensure that the sampling condition $N_x = \lambda_L z/\Delta x^2$ is preserved for all our programmed phase masks. The spacing between pixels ($\Delta x = 9.2\,\mu\text{m}$) is chosen to match our SLM's pixel size. If the diameter of shaped field in the Fourier plane has to be smaller than I, the target image's size is less than $N_x \times N_y$. For all our experiments, the shaped field is smaller than I. Thus, the matrix I is split into two regions (see Fig. 4.3(a)). First is the signal region (S), where the desired amplitude is defined. Second is the noise region (N), which is padded with zeros for maintaining the sampling condition. Also, the defined ($1/e^2$, 7.5 mm diameter) Gaussian source intensity in the algorithm is constrained (see Fig. 4.3(b)) within the dimension of our SLM ($R_{\text{SLM}} = 5.3\,\text{mm}$). The pupil function of the SLM (T_{SLM}) is applied to A_{source} in the SLM plane during the iterative process to match the experimental conditions:

$$T_{\text{SLM}} = \begin{cases} 1 & \text{for } \sqrt{x^2+y^2} < R_{\text{SLM}} \\ 0 & \text{for } \sqrt{x^2+y^2} \geq R_{\text{SLM}} \end{cases} \tag{4.12}$$

The initial phase and the amplitude constraint of the laser's electric field

The initial phase that is used for starting the iterative algorithm can take the following spatial distribution [PWCD16a]:

$$\phi_{\text{initial}} = \begin{cases} \text{random} \\ \text{quadratic} \\ \text{constant} \end{cases} \tag{4.13}$$

The random phase is $\phi_r = \text{rand}(N_x, N_y)$, where $\text{rand}(N_x, N_y)$ is the Matlab function that generates random values between 0 and 1. Furthermore, the quadratic phase is $\phi_q = C_1 x^2 + C_2 y^2$, where C_1 and C_2 are object-dependent coefficients. To optimize the coefficients, one should check that the spectrum ($\text{FFT}[|(A_{\text{Target}})| \exp(i\phi_q)]$) is smooth and within the bandwidth of the defined source field at the SLM plane [PWCD16b]. The constant phase is defined as $\phi_c = 1$.

In the classical GSA the amplitude in the Fourier plane is constrained in the whole matrix I:

$$A(x, y) = A_{\text{Target}}(x, y) \qquad \text{for } x, y \in I. \tag{4.14}$$

Alternatively, one can constrain the amplitude only in the signal region:

$$A(x, y) = \begin{cases} A_{\text{Target}}(x, y) & \text{for } x, y \in S \\ A(x, y) & \text{for } x, y \in N. \end{cases} \tag{4.15}$$

The goal is to shape the source intensity into a new high-quality distribution. The following sub-chapters discuss when a specific initial phase should be implemented. Furthermore, we will discuss when the implementation of Eq. 4.15, which deviates from the classical GSA, is useful.

Quality of the reconstructed image

To assess the quality of the reconstructed intensity, we use the two-dimensional Matlab correlation function (f_{corr}) and the diffraction efficiency (d_{eff}), defined as follows:

$$f_{\text{corr}} = \frac{\sum_{\text{m}} \sum_{\text{n}} (A_{\text{mn}} - \overline{A})(B_{\text{mn}} - \overline{B})}{\sqrt{(\sum_{\text{m}} \sum_{\text{n}} (A_{\text{mn}} - \overline{A})^2)((\sum_{\text{m}} \sum_{\text{n}} (B_{\text{mn}} - \overline{B})^2))}}, \tag{4.16}$$

with A_{mn} and B_{mn} are the components of the target and reconstructed intensity, where m and n indicate the number of rows and columns. The $\overline{A}$ and $\overline{B}$ calculates the the mean value of all matrix components.

$$d_{\text{eff}} = \frac{\sum_{x,y \in S} I}{\sum I}. \tag{4.17}$$

4.3.2 Speckle suppression of the desired intensity distribution with an initial quadratic phase

Speckle suppression without the implementation of a beam block in the GSA

An SLM [MJBRM11b] displays the iteratively calculated hologram (see section 4.3.1), which imprints phase shifts onto the source field such that the desired intensity distribution is generated in the Fourier plane of the SLM. However, a common issue [PWCD16b] with the GSA is that the phase changes erratically with each iteration, and the resulting hologram will contain neighboring phase values differing by close to π, which can lead to local destructive interference (speckles) in the intensity distribution. Figure 4.4 shows holograms (50 iterations) that are calculated with ϕ_q (a) and ϕ_r (b).

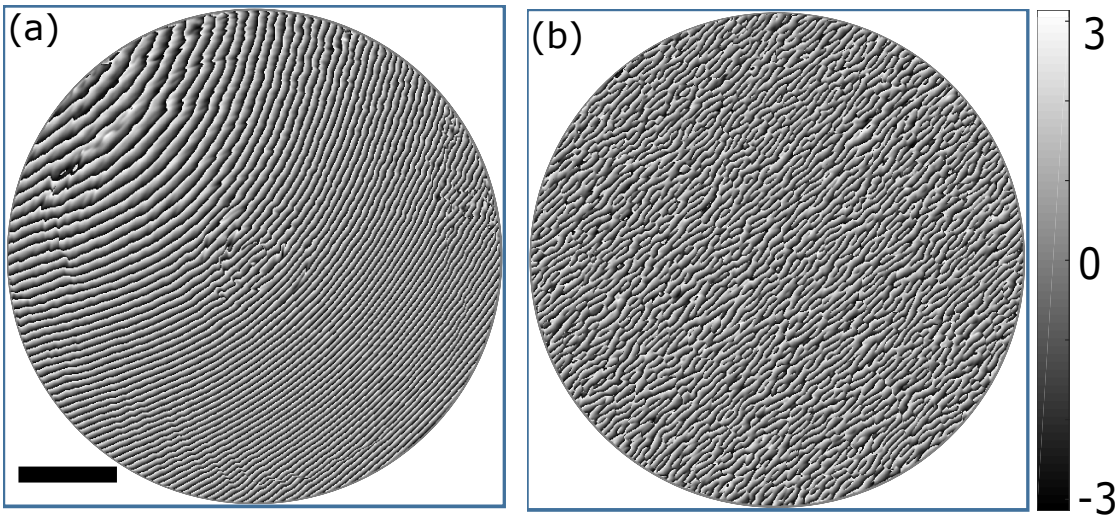


Figure 4.4: (a) Hologram (scalebar 211 μm) calculated as described in section 4.3.1 by using ϕ_q and by constraining the amplitude only in the signal region. The ϕ_q ensured that there are no unwanted π jumps between neighboring phase values in the hologram. (b) Hologram calculated by using ϕ_r.

The speckles in the reconstructed image can be suppressed by initiating the algorithm with a quadratic phase rather than a random or constant phase and by restricting the amplitude in the Fourier plane only in the signal region (see Eq. 4.15). Constraining the amplitude only in the signal region has the advantage of applying fewer restrictions to the algorithm. The initial quadratic phase facilitates a smooth transition between neighboring values of the hologram during the iterative process. The method described here is similar to the studies in [SKE+15, PWCD16b], with the difference that we do not put constraints on the phase during the iterative process. Figure 4.5(right) shows a target image ($|A_{\text{Target}}|^2$, 150×150 pixels) selected to be reconstructed in the CP. First, the ϕ_r (see Fig. 4.5(a)) has been chosen as a starting phase to reconstruct the images in Figs. 4.5(b)-(d), whereas

(d) shows the experimentally measured intensity. Figures 4.5(b)($f_{\text{corr}} = 93\,\%$, $d_{\text{eff}} = 89\,\%$) and (c)($f_{\text{corr}} = 96\,\%$, $d_{\text{eff}} = 82\,\%$) are the reconstructed images with the Fourier constraint in the I (b), and in the signal region (c). We see that the division into a signal and noise region, leads to a higher correlation coefficient at the expense of lower efficiency.

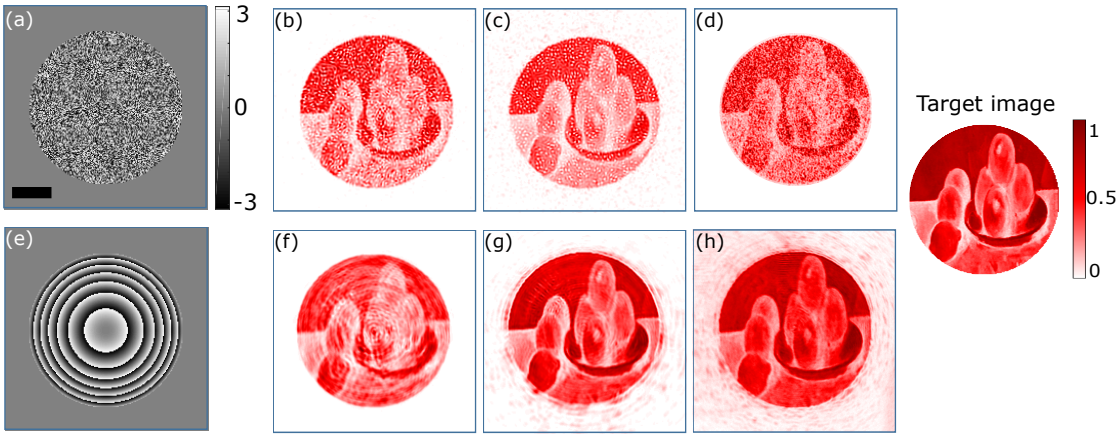


Figure 4.5: The target image (right) that needs to be reconstructed. (a) ϕ_r (scalebar 345 μm). (b) The reconstructed intensity while using ϕ_r and Eq. 4.14. (c) The reconstructed intensity while using ϕ_r and Eq. 4.15. (d) The experimentally measured reconstructed image (from (b)) with the CMOS. (f) The reconstructed intensity while using ϕ_q (from (e)) and Eq. 4.14. (g) The reconstructed intensity while using ϕ_q (from (e)) and Eq. 4.15. (h) The experimentally measured reconstructed image (from (g)) with the CMOS in the CP. Both ϕ_q and amplitude constraint in the signal region have to be implemented to achieve a speckle-free image.

Second, the ϕ_q (see Fig. 4.5(e)) has been chosen to initiate the modified GSA for the Figs. 4.5(f)-(h). The coefficients of the ϕ_q are optimized to $C_1 = C_2 = 8.2 \times 10^7$. Figure 4.5(f)($f_{\text{corr}} = 95\,\%$, $d_{\text{eff}} = 95\,\%$) is the reconstructed image with the Fourier constraint in I. Figures 4.5(g) ($f_{\text{corr}} = 99\,\%$, $d_{\text{eff}} = 88\,\%$) and (h) are the reconstructed and experimentally measured speckle-free images, respectively. Note that the NA should be high enough to image the pattern from the CP to the IP for the ponderomotive experiments.

Speckle suppression with the implementation of a beam block in the GSA

In the following, the influence of the beam block's diameter (D_{bb}) on the quality of the reconstructed intensity is investigated for two target images having different diameters in the signal region. The target image from Fig. 4.5(right) is now reconstructed in Fig. 4.6(b)-(e) and (g)-(j), while implementing various D_{bb} (see Fig. 4.2) in the modified

GSA. Furthermore, when resizing the images in the signal region from 150× 150 to 40×40, the coefficients of the ϕ_q need to be adjusted. For the ϕ_q in Fig. 4.6(f) the coefficients have been optimized to $C_1 = C_2 = 3.2 \times 10^8$. Table 4.1 shows the correlation and the diffraction efficiency between the target and reconstructed images as a function of beam block diameter.

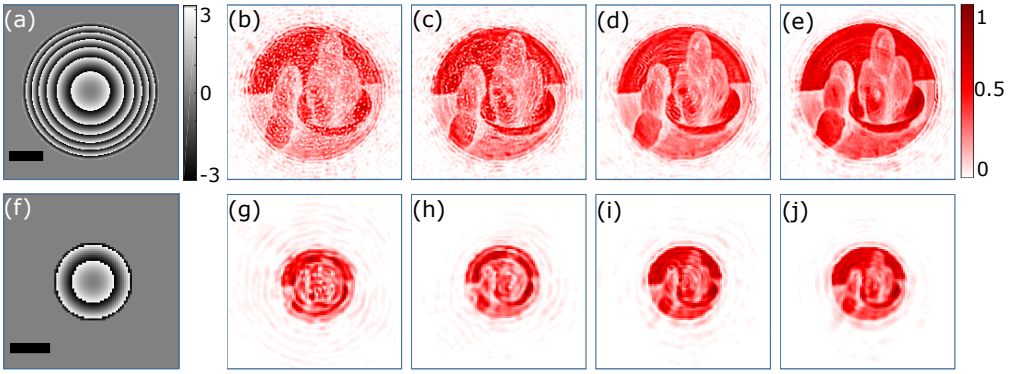


Figure 4.6: The influence of the size of the beam block on the quality of the reconstructed intensity (50 iterations). (a) The ϕ_q shown here is the same as in Fig. 4.5(e) (scalebar 345 μm). (b)-(e) The reconstructed images (150×150 pixels) for $D_{\text{bb}} = 2\,\text{mm}$(b), $D_{\text{bb}} = 1.5\,\text{mm}$(c), $D_{\text{bb}} = 1\,\text{mm}$(d), $D_{\text{bb}} = 0.5\,\text{mm}$(e). (f) The ϕ_q (scalebar 184 μm) used to reconstruct the images (g)-(f). (g)-(j) The reconstructed images (40×40) for decreasing D_{bb}.

The speckle suppression method described here has yet to be further implemented for electron beam shaping. In our experiments $D_{\text{bb}} = 1.5\,\text{mm}$, which drastically affects the reconstructed image's quality and makes the speckle suppression method impractical. Nevertheless, the hole size (simulated here as a beam block) in the mirror that allows the on-axis interaction between electron and laser pulses could be reduced in future setups. According to the data in table 4.1, a small D_{bb} would improve the correlation and diffraction efficiency.

D_{bb} [mm]	2	1.5	1	0.5
f_{corr} from Fig. 4.6(b)-(e)	93%	96%	98%	99%
d_{eff} from Fig. 4.6(b)-(e)	73%	76%	81%	86%
f_{corr} from Fig. 4.6(g)-(j)	93%	94%	98%	99%
d_{eff} from Fig. 4.6(g)-(j)	62%	74%	81%	84%

Table 4.1: Evaluating the quality of the reconstructed images for different beam block sizes. Both f_{corr} and d_{eff} improve with the decrease of the D_{bb}. The d_{eff} is higher when reconstructing 150×150 compared to 40×40 pixels images. The f_{corr} seems not to be affected by the size of the target image, and shows promising results for $D_{\text{bb}} < 1\,\text{mm}$.

4.3.3 Shaping the laser beam for electron deflections

This sub-chapter describes how the laser beam is shaped into small signal regions to be used for the ponderomotive experiments in chapter 6. The phase shift 2.36 induced to the electrons is inversely proportional to the integrated laser beam intensity; therefore, if the laser phase plate is spanned over a big area, no modulation of electrons would be visible at the detector plane. The MCP resolution necessitates ($\delta x = \theta_{x,f} \cdot d = 181\,\mu\text{rad} \cdot 55\,\text{cm}$) $\sim 0.1\,\text{mm}$ scale electron deflections to observe a change in electron intensity distribution. The deflection angle of the electrons is denoted by $\theta_{x,f}$ and the distance from the interaction plane to the MCP by d. One can use Eq. 5.7 (defined in a later chapter) to calculate the maximum laser beam diameter ($16\,\mu\text{m}$) that can be used at $E_L = 17.2\,\mu\text{J}$ to get $\theta_{x,f} = 181\,\mu\text{rad}$. With an NA of 0.2 we can use ~ 14 pixels for deflection. Thus, we selected target images that contain a limited number of pixels. Figure 4.7 shows the shaped laser intensity distributions resembling the letters 'ψ', 'O', and 'Smiley', which have been later used to deflect the electrons.

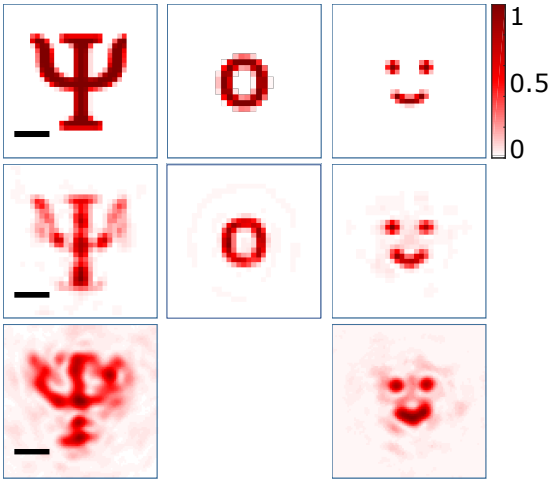


Figure 4.7: Intensity profiles are obtained with the modified GSA. (top row) The desired target images resemble the letter 'Psi', 'O' and a 'Smiley' (scalebar $66\,\mu\text{m}$). (center row) The resulting simulated, reconstructed images after 20 iterations with the modified GSA (scalebar $66\,\mu\text{m}$). (bottom row) The intensity distributions are measured with the CMOS in the conjugate plane (scalebar $70\,\mu\text{m}$) before being demagnified 5x in the interaction plane. The measured intensity of the letter 'O' is missing. Unwanted intensity fluctuations are present in the simulated reconstructed image and in the CMOS-measured intensity distribution of the letter 'ψ'. The reasons for intensity fluctuations are the small number of pixels used for defining the target image and the implementation of the $1.5\,\text{mm}$ beam block in the GSA.

To calculate the required phase mask to be displayed on the SLM, the modified GSA from section 4.3.1, with the implementation of a beam block (D_{bb}), is used. The iterative

process can also be visualized in Fig. 4.2. For target images that contain only a few pixels, the modified GSA with an initial phase ϕ_c showed the best experimental results. Also, during the iterations, the amplitude is constrained (see Eq. 4.14) in the whole matrix I to facilitate the diffraction efficiency.

The calculated phase masks (ϕ_{GSA}) displayed on the SLM that shape the source field into the desired intensity distributions (see Fig. 4.7) in the CP are shown in Fig. 4.8. The target image is defined off-center at the SLM to separate the reconstructed image from the unmodulated light reflected off the SLM. For demagnifying (5x) the reconstructed focal shapes from the CP to the IP, a 4f system ($f_2 = 250\,\text{mm}$ and $f_3 = 50\,\text{mm}$)) is used. Note that the demagnification introduces additional aberrations into the optical beam path. To minimize the aberrations, an additional hologram (see Fig. 4.8(d)) has been superposed to the calculated holograms (see Figs. 4.8(a), (b), (c)).

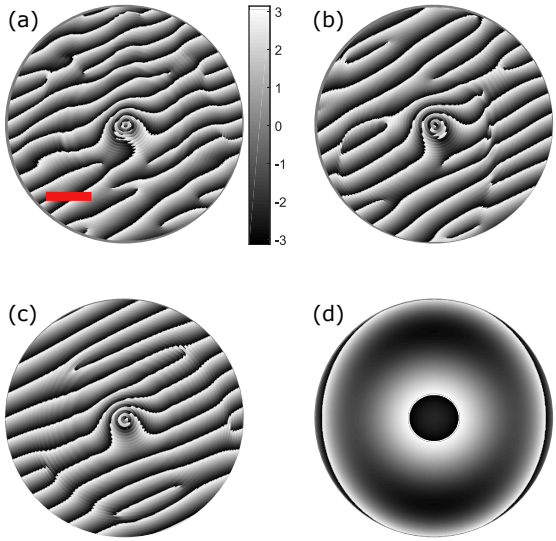


Figure 4.8: (a)(b)(c) The calculated holograms with the modified GSA (see Fig. 4.2) for shaping the Gaussian laser distribution into a letter (a) 'Psi', (b) 'Smiley', and (c) letter 'O' (scalebar 2.1 mm). The algorithm converged after 20 iterations. Note that the target images used here have pixel numbers <20; therefore, no initial quadratic phase can be used to start the GSA. Thus, the reconstructed images can suffer from speckles. The holograms have been displayed on the SLM to shape the source intensity into the desired intensity distributions. (d) An additional correcting hologram (ϕ_{cor}) is superimposed onto the GSA-calculated holograms when transferring the light intensity distributions from the CP to the IP.

This step is required to minimize the aberrations introduced by the additional optical elements along the beam path from the CP to the IP. For the correction phase mask in Fig. 4.8(d) following Zernike polynomials have been added: $\phi_{\text{cor}} = (1.3 \times \pi \times Z_0^4 +$

$0.5 \times \pi \times Z_2^2$). The Zernike polynomials are defined in a later chapter (see table 6.1). The coefficients of the Zernike polynomials have been optimized by measuring the laser focal shape in the interaction plane with a miniaturized (OV5647) CMOS. Figure 4.7(center),(bottom) shows the simulated reconstructed intensities and the measured intensities with the CMOS in the conjugate plane, respectively.

The quality of the reconstructed image from Fig. 4.7 is shown in table 4.2. One can see that the correlation could be better. The imperfections in the reconstructed images are due to the implementation of the beam block in the iterative algorithm and the small number of pixels in the target image.

-	letter Psi	Smiley	letter O
d_{eff}	91%	90%	91%
f_{corr}	92%	89%	87%

Table 4.2: The quality of the reconstructed (simulated) images from the conjugate plane. The comparison is made between the target intensities and the reconstructed intensities after diffraction from the phase mask calculated with the modified GSA. The algorithm converged after 20 iterations. More iterations slightly improve the reconstructed image's correlation coefficient; however, the measured intensity distributions start to degrade due to the emergence of speckles.

Intensity loss at the beam block implemented in the modified GSA

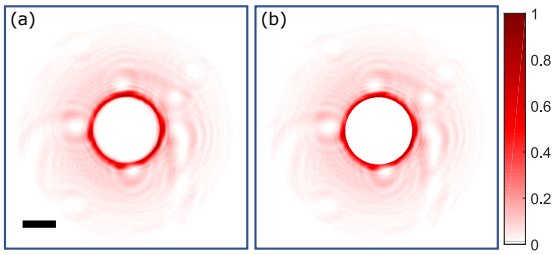


Figure 4.9: (a) The simulated intensity distribution (scalebar 0.75 mm) at $f/2$ distance away from the probe forming light lens in the CP. (b) The intensity distribution from (a) superimposed with the 1.5 mm diameter beam block. Five % ($I_{(b)}/I_{(a)}$) of the total intensity is lost in the beam block. The hole in the last mirror allows the collinear interaction of the laser pulse with the counter-propagating electron pulse because the electrons need to pass through the mirror. The beam block implemented in the modified GSA simulates the hole in the mirror which has a diameter of 1.5 mm.

To evaluate the effectiveness of the 1.5 mm beam block implemented in the modified GSA, we first calculate the phase mask with the modified GSA (see Fig. 4.2) to diffract and

shape the initial source Gaussian beam into the smiley shown in Fig.4.7. We start from the SLM plane and propagate the field up to the beam block (at f/2 after the lens) and get the absolute squared value of the field to see how the intensity is distributed around the beam block. The intensity distribution in the plane of the beam block can be seen in Fig. 4.9 and indicates that the beam block is implemented successfully into the iterative algorithm. However, five % loss at the beam block can induce thermal instabilities if high pulse energy is used.

For our proof-of-concept experiments, the shaping method described here is sufficient. Nevertheless, we do aim to generate laser phase plates of larger areas in the future. For those experiments, the speckle correction scheme described in sub-chapter 4.3.2 will be useful.

4.3.4 The Laguerre Gauss beam of charge one

It is shown in a later chapter (6) that the Laguerre-Gauss beam can be used to create a convex light-based lens for electrons. This section describes the practical challenges of creating a Laguerre-Gauss beam experimentally. Mathematically, the electric field of Laguerre-Gauss modes is defined as [UKS22]:

$$\begin{aligned} E_{LG}(r,z) =& \frac{w_0}{w(z)} \left(\frac{\sqrt{2}r}{w(z)} \right)^{|\ell|} L_p^{|\ell|} \left(\frac{2r^2}{w^2(z)} \right) \exp\left(-\frac{r^2}{w^2(z)} \right) \\ & \times \exp\left[\frac{ikr^2}{2R(z)} + i\ell\phi + i(2p+|\ell|+1)\eta(z) \right] \end{aligned} \tag{4.18}$$

where p is the radial index, l is the azimuthal, r the radial distance and z the axial distance from the center of the beam. $L_p^{|\ell|}$ represent the Laguerre polynomials [Lag], $w(z) = w_0\sqrt{1+z^2/z_{\mathrm{R}}^2}$ is the radius of the beam along the z coordinate, w_0 the radius where the amplitude drops to $1/e^2$, and $z_{\mathrm{R}} = \pi w_0^2/\lambda_L$ is the Rayleigh range. Furthermore, $R(z) = z\left(1 + z_{\mathrm{R}}^2/z^2\right)$ is the radius of curvature, $\eta(z) = \tan^{-1}\left(z/z_{\mathrm{R}}\right)$ is the Gouy phase, and ϕ the helical phase factor. For p=0, the intensity of the Laguerre-Gauss modes in focus becomes:

$$I_{LG}(r,0) = I_0 \left(\frac{r\sqrt{2}}{w_0} \right)^{2|l|} \exp\left(\frac{2r^2}{w_0^2} \right) \tag{4.19}$$

The donut beam (Laguerre-Gauss beam of charge one, LG10) profile has $p = 0$ and $l = 1$, whereas the Gaussian beam (LG00) has $p = 0$ and $l = 0$.

Donut beams are widely used in super-resolution microscopy [KEH01], like stimulated emission depletion microscopy (STED) and optical tweezers [SAP96]. Tuning the donut profile to achieve the highest resolution requires a careful alignment procedure. While

the Gaussian beam is more sensitive to odd aberrations, the LG10 mode is sensitive to both even and odd azimuthal aberrations [BN06] and hence prone to minor phase errors that can lead to a distorted intensity profile.

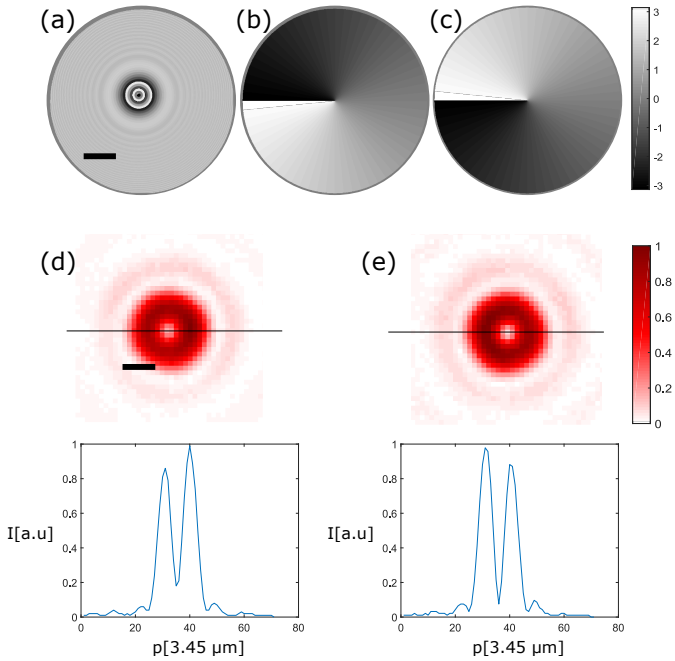


Figure 4.10: Experimentally measured LG10 beam. Two phase masks are calculated to shape the Gaussian source beam into a distribution with a singularity in the center. (a) First, the back-propagation code calculates a phase mask (scalebar = 1.9 mm) that diffracts the light around the 1.5 mm hole and separates the undiffracted, reflected light off the SLM. (b), (c) Second, a vortex phase mask with ramping values from $-\pi - \pi$ has to be added to the initially calculated phase mask shown in (a). In (d)(top), (e)(top)(scalebar = 24 μm), the measured intensity distributions are shown when using the vortex phase masks from (b) and (c), respectively. The intensity plotted along a line from (d), (e)(top) as a function of pixels are shown in (d), (e) bottom. The residual intensity in the center of the donut beam is minimized to 7.6% when using the inverted vortex phase in (c). The residual is 18% when applying the vortex phase mask from (b).

Furthermore, it is common for experimentally generated LG10 profiles to show a residual intensity in the center of the LG10. Reasons for the residual intensity in the center include sampling issues in the profile measurement, imperfect alignment, and in the case of high NA also the polarization [GGG03, NCS+13]; whereas a right circular polarized beam can lead to minimal residuals. For small and moderate NAs (<0.2) used for our ponderomotive experiments, a linearly polarized beam should be good enough to get a residual-free LG10 mode [PM18]. If the beam block implementation is not required in the

hologram calculation, a so-called forked grating is enough to diffract a source beam into a donut mode. The forked grating is a sum between a blazed grating and a vortex phase plate.

While earlier techniques involved material phase plates in inducing the vortex phase onto the incident expanded Gaussian beam, nowadays, SLMs are used [JSF$^+$07] to create donut beams. The phase masks displayed on the SLM for the generation of LG10 modes in our experiments are depicted in Fig. 4.10. First (Fig. 4.10(a)), a phase mask (ϕ_G) is calculated using a back-propagation of the Gaussian field from the Fourier plane to the SLM. As in the GSA in Fig. 4.2, the back-propagation includes the beam block and offsets the target from the optical axis to separate the diffracted beam from the reflected beam off the SLM. Second, a vortex phase plate ($\phi_{V10} = \text{atan2}(\text{Y}, \text{X})$) (Fig. 4.10(b), (c)) with ramping values from $-\pi$ to π is superimposed to the ϕ_G ($\phi_{\text{LG10}} = \text{modulo}2\pi[\phi_G + \phi_{\text{V10}}]$), and displayed on the SLM. The 'atan2(Y,X)' Matlab function is the four-quadrant inverse tangent used to create vortex phase distributions of different charges.

The intensity distributions along a line profile in the donut beams shown in Fig. 4.10 (d),(e),(top) are plotted in Fig. 4.10 (d),(e),(bottom). Interestingly, when the sign of the vortex phase plate is inverted (Fig. 4.10(c)), the residual in the center of the donut drops to 7.6%, whereas using the non-inverted phase mask (Fig. 4.10(b)) leads to a donut profile with a residual of 18%. For high NA$\sim$ 1 optical systems, the intensity at the center of a LG10 goes to zero only if the orientation of the topological charge is aligned with the right-handed circularly polarized light. However, in our setup we have a low NA, and the polarization should not influence the residual in the center of the LG10 [PM18]. Thus, we do not completely understand why the orientation of the topological charge matters.

5 Spatial and temporal overlap between electrons and light pulses without an energy filter

Initially, we tried to synchronize the laser and electron pulses in the IP directly by going for ponderomotive interaction. However, this was unsuccessful because it is challenging to accurately calculate the arrival time of the electrons in the IP. Furthermore, the pulse length of the electrons in the IP is $< 1\,\mathrm{ps}$, and a timing mismatch $> 1\,\mathrm{ns}$ could lead to thousands of delay scan points that are required to synchronize the pulses in time. In addition, the cumbersome delay scan must be carried out at high laser pulse energy. To avoid the long delay scans and work with high laser pulse energy, we developed a step-wise method for establishing the timing and spatial overlap described in this chapter.

5.1 Reducing the timing mismatch between the laser and electron pulse

The timing overlap between laser and electron pulses in an electron microscope is usually achieved by doing pump-probe measurements and measuring the energy loss spectrum of the electrons [PLZ10]. More recently, the temporal overlap has also been achieved without an energy filter [OVDL22]. Here, we achieve temporal and spatial overlap without an energy filter by following a multi-step process. First, a fast-timing scintillator (BC-408) is placed in the interaction plane. A silicon photomultiplier measures the delay between electron-triggered photons from the scintillator and the transmitted laser pulse. The timing mismatch is reduced to 200 ps. Second, pump-probe measurements are carried out with a copper grid in the interaction plane. At t0, substantial electron beam distortions can be observed due to generated electron and ion clouds. Third, the grid is removed, and the overlap between electrons and laser pulses is confirmed by measuring strong electron beam deflections due to ponderomotive scattering.

5.1.1 Fast-timing scintillators

For ultra-fast timing applications in high-energy physics [Bir13], plastic scintillators convert the deposited energy into visible light with the timing resolution of detection systems well below 100 ps [LP91, BGM$^+$14]. A scintillator used for fast timing should have a high light yield and fast temporal response characterized by a short rise and decay time. The intrinsic temporal response of common fast-timing scintillators has been

studied in [DWMD00, SSVDS12]. Moreover, plastic scintillators read out by low-intensity light detectors [AFG+14] can be used for particle identification, event sorting, and signal triggering [ZSS+20]. Generally, plastic scintillators are not used in electron microscopes due to concerns about beam-induced damage [Kha19]. For this reason, inorganic scintillators like Yttrium aluminum perovskite (YAP:Ce) [BBd+95], or P47 [WKBV14] are preferred when timing applications are less crucial. However, at low beam currents (below 1 pA) used in pulsed electron microscopes [YMZ10] the plastic scintillator BC-408 shows no degradation over beam exposure. We used a gold coated ($\sim 5\,$nm, to avoid charging) BC-408 as an ultra-fast timing scintillator. While BC-422 would have a slightly faster response [BGM+14], BC-408 provided an economical option with sufficient resolution to reduce timing mismatch to less than 200 ps. This is within one scan range of our delay stage, which can then be used for fine delay adjustments based on the measurements described in sub-chapter 5.2. The scintillation properties of a few fast scintillators are listed below:

Scintillator	Anthracene	BC-408	BC-422	YAP:Ce	P43	P47
Type	organic	plastic	plastic	inorganic	inorganic	inorganic
Light yield, % Anthracene	100	64	55	109-117	483-725	145-156
Rise time	2.8 ns	0.9 ns	0.35 ns	0.38 ns	-	6.7 ns
Decay time	30 ns	2.1 ns	1.6 ns	27 ns	>1 ms	70 ns
λ_{max} emission [nm]	447	425	370	370	545	430

Table 5.1: Scintillator properties are taken from [OKK70, BBd+95, SG2, WKBV14]. The plastic scintillators show better timing response and are much cheaper than the organic ones.

5.1.2 Ultra-low light intensity detection with Silicon Photomultipliers

Silicon photomultipliers (SiPM) or multi-pixel photon counters (MPPC) are solid-state devices with internal gain that can detect single photons [Ren06, SSR+07, SSS12, CDGG+14, DFI15]. One SiPM sensor consists of a dense array of avalanche photodiodes, operated in Geiger mode and individually sensitive to single photons. The sensors are robust, cheap, immune to magnetic fields, require low bias voltage, and have high detection efficiency and excellent time resolution. The SiPMs are a great replacement [AFG+14] for photomultiplier tubes, avalanche photodiodes, or PIN diodes. For our experiments, we use a SiPM sensor (Ketek, PM1125-WB PIN, gain$\sim 10^6$, bias voltage $\sim 30\,$V) to detect the ultra-low light intensity generated when the pulsed electrons hit the plastic scintillator. The SiPM sensor is mounted outside the vacuum chamber on a read-out board (KETEK, PEPCB-EVAL-MCX-RES-P). The analog output signal from the read-out board is further amplified by a factor of 100x (voltage amplifier, FEMTO HSA-Y). The waveform is acquired subsequently with the digital oscilloscope (Infiniium Keysight, MSOX3104T). The arrival time of the photons triggered by the scintillator and

the IR laser is read out directly from the oscilloscope signal. Note that the out-coupling optics that transfer the scintillated light from the IP to the SiPM sensor should match a central wavelength of emission of the scintillator used. The bottom of the scintillator is wrapped in aluminum foil to maximize the light output. Also, the OA has been removed to increase the number of electrons impinging on the scintillator. We are using a relatively moderate NA (0.2) to outcouple the light; however, this might be increased in future setups. After the timing measurement, the delay stage, which is placed on the IR arm, is adjusted accordingly. A sketch of the experimental setup used for time-stamping the signals is shown in Fig. 5.1.

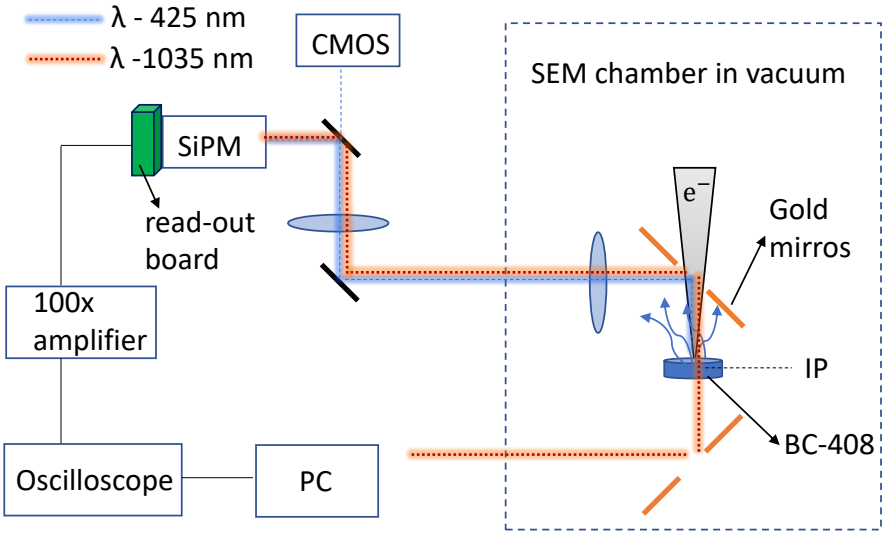


Figure 5.1: Time delay measurement between the electron and IR laser pulse. An ultrafast timing scintillator is placed in the interaction plane. As electrons start to hit the scintillator, photons with a central wavelength at 425 nm are released and transferred to hit a SiPM outside vacuum. The read-out electronics of the SiPM consist of a PCB board, voltage amplifier, oscilloscope, and PC. The arrival time of the scintillated photons is compared with the arrival time of the IR laser to reduce the timing mismatch and synchronize the pulses in the interaction plane. Both scintillated light and IR laser undergo the same path from the IP to the SiPM sensor.

5.1.3 Quantitative time delay measurement

The time delay ($t_{\mathrm{IR}} = -5.32\,\mathrm{ns} \pm 0.13\,\mathrm{ns}$) between the IR laser beam and a fixed trigger signal is determined with the scheme shown in Fig. 5.1. The output of the IR laser has been used as the trigger signal. A trace of the t_{IR} measurement can be seen in Fig. 5.2(a), where 1229 waveforms are acquired to build statistics and extract the timing information. Next, the IR laser beam is turned off. The electron-triggered photons from

the scintillator in the IP are recorded with respect to the same trigger signal. A trace of the electron-triggered photons can be seen in Fig. 5.2(b). Due to the ultra-low scintillated signal, the time delay between the first leading edge (purple in Fig. 5.2) and the trigger signal is estimated at ($t_{\mathrm{SciTil}} \sim -9.3\,\mathrm{ns}$). Finally, the time-delay stage is adjusted by $t_{\mathrm{SciTil}} - t_{\mathrm{IR}} \sim -4\,\mathrm{ns}$. This turned out to be an essential step since the final t0 between the laser and electron pulse is established only 200 ps away from the position estimated with the SiPM and scintillator method.

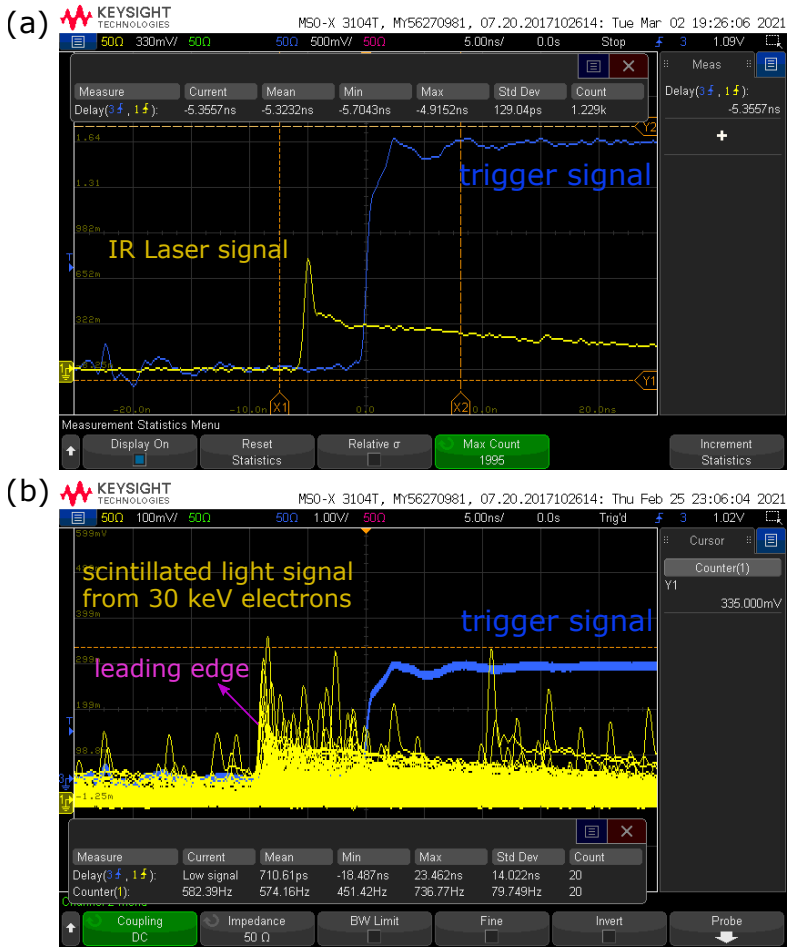


Figure 5.2: Oscilloscope trace of the time delay measurement between a fixed trigger signal and (a) the IR laser beam and (b) the 30 keV electron-triggered photons from the BC-408. (b) The leading edge of the electron-triggered photons (yellow trace) is at about −4 ns away from the IR laser beam. Stray photons are also present outside the leading edge, most likely due to the afterpulsing and crosstalk of the SiPM sensor.

5.2 Pump-probe measurement with a copper grid to establish the spatial and temporal overlap

For the routine establishment of pulse overlap between electrons (probe) and laser (pump), metal mesh grids [DHE+06, DJH+07], pinholes [DHN+06], or silver needles [PHW+05] have been successfully employed. Early experiments [FLIB84] with short femtosecond laser pulses on tungsten have shown that photo-electrons start to leave the metal at peak intensities $\sim 5\,\mathrm{GW/cm^2}$ with a damage threshold of $\sim 200\,\mathrm{GW/cm^2}$. Our experiment uses a copper grid with $\sim 10\,\mu\mathrm{m}$ bar width. Given the photon energy of our IR laser (1.2 eV) and the work function of the copper grid ($\sim 4.5 - 4.6\,\mathrm{eV}$), at least four-photon excitation is required to eject one electron out of the copper grid [ASEA+95, EJR91].

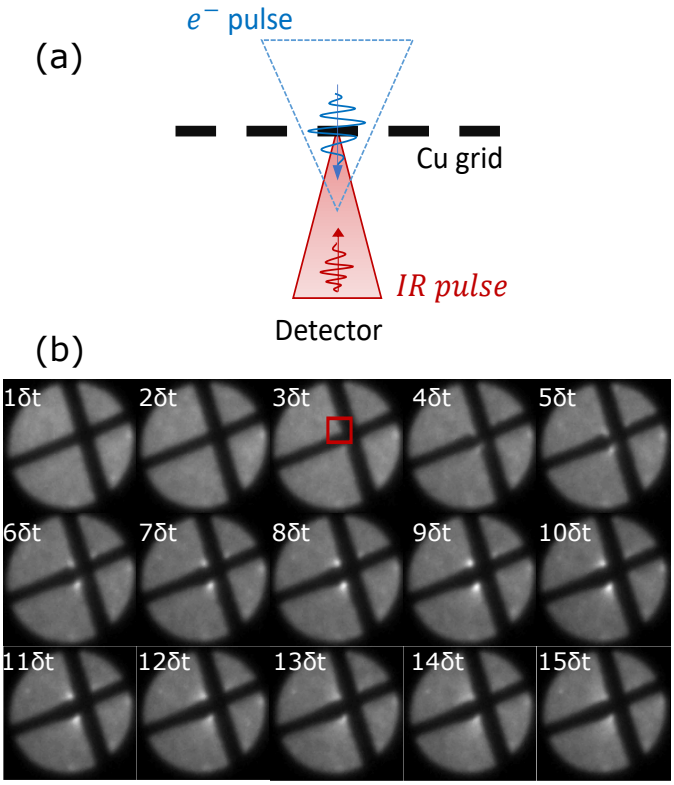


Figure 5.3: Pump-probe measurement with a copper grid in the interaction region. (a) A copper grid with thin bars ($\sim 10\,\mu\mathrm{m}$) is placed in the interaction region. The IR laser beam is focused on the grid generating a strong electron and ion cloud. The laser settings (100 nJ, $I \sim 500\,\mathrm{GW/cm^2}$) are set above the ablation threshold of the copper. When the pulses overlap in space and time, a strong distortion of the electron image can be observed. (b) Series of electron beam images are recorded at multiples of $\delta t = 1.33\,\mathrm{ps}$ delays. As the pulses start to overlap in time, an evident change in the electron image is observed. The exposure time for all images is 5s.

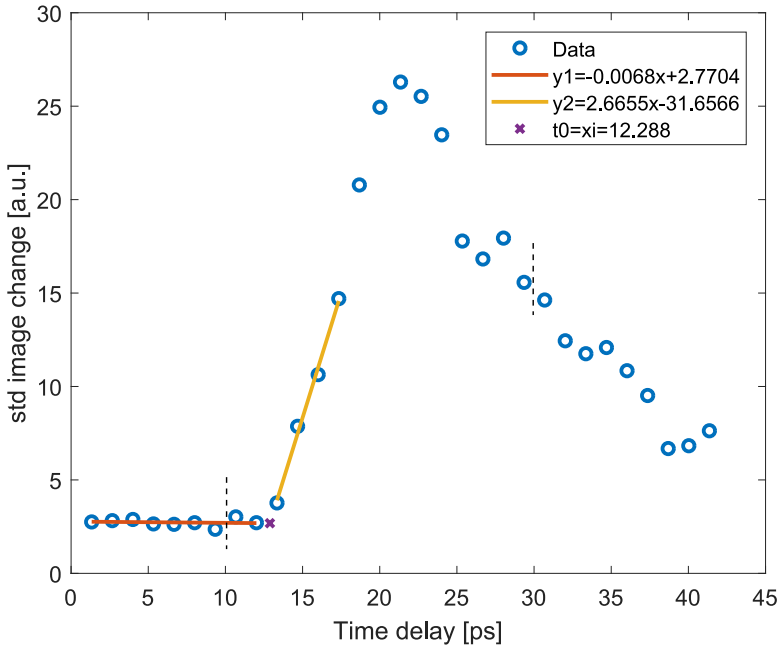


Figure 5.4: The standard deviation of the difference between images with the IR laser on and off is plotted against the time delay ($\delta t = 1.33$ ps steps). The temporal overlap can be found at the intersection point of the two fit functions (yellow and red). Setting $y1 = y2$ and solving for x yields $t0 = x_i = 12.88$. The data within the dashed lines in the plot is evaluated from the series of electron beam images shown in Fig. 5.3(b).

The electron beam at the grid plane has a diameter of $\sim 100\,\mu$m. The orientation of the grid is normal to the laser beam to maximize the electron emission. As the electron pulse starts to overlap with the laser pulse at the grid, strong electron beam deformations due to the generated electron and ion cloud are observed in Fig. 5.3 (b). For all the measurements in Figs. 5.3 and 5.4, the energy per pulse at the grid remains constant at 100 nJ. The shadow image of the pumped copper grid is recorded with the detector as a function of time delay (1.33 ps steps). The std values (see Fig. 5.3) stay above baseline for a long time (> 30 ps), which significantly reduces the delay scan steps that are required when the timing between the pulses is not known. To maximize the sensitivity of the measurement, a differential acquisition has been implemented by using the SLM as an IR beam chopper. For all the images acquired in this timing measurement by the CMOS, 5 s exposure time is used. This is much longer than the refresh rate of our SLM. According to the datasheet [MJBRM11a], the system frame rate is 25 ms. This means that one can switch fast between the optimal phase mask on the SLM that is focusing the laser beam to the grid, and a phase mask that induces a strong defocus of the laser beam such that no photo-electrons can be produced [ASEA$^+$95]. Therefore, an electron image with the laser-focused and defocused on the grid has been acquired at each time delay setting. The standard deviation of the difference between the images is plotted against the time delay

in Fig. 5.4. The precise time zero between the electron and laser pulse can be calculated by fitting the baseline and the rising edge of the distribution in Fig. 5.4 and extracting the time information from the intersection point (purple cross in Fig. 5.4) of the two fit functions [PHW+05]:

$$y_i(x) = a_i x + b_i, \quad \text{with} \quad i = 1, 2. \tag{5.1}$$

The two linear functions are used to fit the baseline and the rising edge of the distribution in 5.4 with $a_{1,2}$ the slopes, and $b_{1,2}$ the intercepts. The intersection point of the two functions will reveal the time zero delay between the electron and laser pulse and can be calculated by setting the fit functions equal $y_1(x) = y_2(x)$:

$$x_i = t_0 = \frac{b_2 - b_1}{a_1 - a_2}. \tag{5.2}$$

with t_0 the time zero delay. The uncertainty of the time zero determination is $s_{t_0} = 1.05$ ps and is calculated by the error propagation of the two linear fit functions coefficients [BRB+93], as follows:

$$s_{t_0} = \sqrt{(\frac{\partial t_0}{\partial b_2})^2 s_{b_2}^2 + (\frac{\partial t_0}{\partial b_1})^2 s_{b_1}^2 + (\frac{\partial t_0}{\partial a_1})^2 s_{a_1}^2 + (\frac{\partial t_0}{\partial a_2})^2 s_{a_2}^2}. \tag{5.3}$$

where $s_{a_{1,2}}, s_{b_{1,2}}$ are the standard deviations of the slopes and intercepts. With better scattering signal and smaller delay scan steps, the uncertainty of the time zero determination can be improved to be well below 1 ps [PHW+05, DHE+06].

5.3 Spatial and temporal overlap with ponderomotive deflection

After establishing the time zero delay and spatial overlap by measuring the time delay (see Fig. 5.1) and doing pump-probe measurements with the copper grid (see Fig. 5.2) in the interaction plane, the grid is removed. Subsequently, electron beam deflections in free space due to ponderomotive scattering are observed at the detector plane. The experimental setup of the ponderomotive scattering experiment inside the vacuum is depicted in Fig. 5.5 (a). The objective aperture (OA) is fixed to 100 μm for all the ponderomotive measurements. The SEM objective lens (OL) focuses the electron beam below the IP, having a working distance of $\sim$ 40 mm. From the IP, the electrons propagate further in free space for $d = 550$ mm to reach the detector. Figure 5.5 (b)(bottom) shows the electron beam distribution at the detector plane after the interaction with the laser beam 5.5(b)(top). The electron beam crossover for the experiment in Fig. 5.5(b) is located at $d_c = d/(\rho_s/\rho_0 - 1) = 5.9$ mm from the IP, which can be calculated by measuring the radius of the electron beam in the detector ($\rho_s = 1.65$ mm) and interaction plane ($\rho_0 = 17.5\,\mu$m). The laser pulse energy used for Fig. 5.5(b)(bottom) is 6 μJ. In a nutshell, the step-wise method of synchronizing the pulses in space and time has proved to be a handy tool for ponderomotive interaction.

Wave (top) and ray (bottom) optics simulations (see Fig. 5.5 (c)) of the electron light interaction for the detected electron distribution in Fig. 5.5 (b) yield similar results. The classical ray tracing method has been used for the ray optics simulation, where electrons are seen as ballistic particles and get deflected by the laser beam towards regions of lower field intensities [Kib66]. The motion of the electrons in the focal plane of the laser beam is disturbed by the transverse momentum kick induced, which is derived as follows [CMWS+22]:

$$\varphi = -\frac{1}{\hbar}\int U\,dt, \tag{5.4}$$

$$\hbar\nabla\varphi = -\int \nabla U\,dt. \tag{5.5}$$

Using the relation $\nabla U = -F$ and $\delta p_T = \int F\,dt$ gives:

$$\delta p_T = \hbar\nabla\varphi(x,y). \tag{5.6}$$

The equation is valid for the nonrelativistic laser fields $a \ll 1$, where $a = eE\lambda_L/(m_e 2\pi c^2)$ at low to moderate laser intensities ($I < 18 - 19\,\mathrm{W/cm^2}$), with e being the elementary charge, ϵ_0 the vacuum permittivity, ω the optical angular frequency, a the normalized field amplitude, E the electric field of the laser, λ_L the laser wavelength and m_e the electron mass. For the relativistic case (where the ultra-intense laser pulse not the case considered here exceeds $a \gg 1$), the magnetic field component of the laser field cannot be neglected anymore and has to be included in the derivation of the ponderomotive potential [SS70, QM98, MHS19].

The scattering angles of the electrons in x-y plane can be calculated by:

$$\theta_{x,f} = \theta_{x,i} + \hbar\nabla_x\varphi(x,y)/p_z, \tag{5.7}$$

$$\theta_{y,f} = \theta_{y,i} + \hbar\nabla_y\varphi(y,y)/p_z. \tag{5.8}$$

The initial angles are defined as $\theta_{x,i} = x/d_c$ and $\theta_{y,i} = y/d_c$ and p_z is the electron momentum in z direction. For the wave optics simulation shown in 5.5 (c)(top) the Fresnel diffraction of the electron wave after the interaction with the laser field has been simulated. For further details about the classical ray tracing and wave optics simulations, see [CMWS+22, Sch22a].

To constrain the interaction to take place in the focal region of the laser beam, the time delay has been optimized by reducing the electron beam radius at the IP to $\sim \rho_0 = 7\,\mu\mathrm{m}$ such that the scattering signal is maximized (see Fig. 5.5 (d)(left)). A series of deflected electron beam images at different time delays ($\tau = 666\,\mathrm{fs}$ steps) is acquired to show how the timing mismatch affects the electron distribution. The fact that the scattering signal

doesn't change much around $\pm\tau$, indicates that the pulses overlap entirely in time and suggests that the interaction takes place in the focal spot of the laser beam. The laser focal spot has a full width half maximum (FWHM) of 4.3 μm leading to a Rayleigh range of 41 μm. For all the measurements, the time delay of the laser pulse has been varied with respect to the electron pulse. It can be observed that a timing mismatch of $\pm\tau$ does not affect much the electron distribution because the interaction plane is shifted by $\delta z = v\tau/(1+v/c)$, and hence, the electrons see almost the same laser field and experience similar ponderomotive forces. On the other hand, if the time delay is too large ($> 3\tau$), the electron beam interacts with the laser beam in a plane where the laser beam is not focused, and therefore, the ponderomotive signature fades away (see Fig. 5.5(d)(left)(top and bottom)).

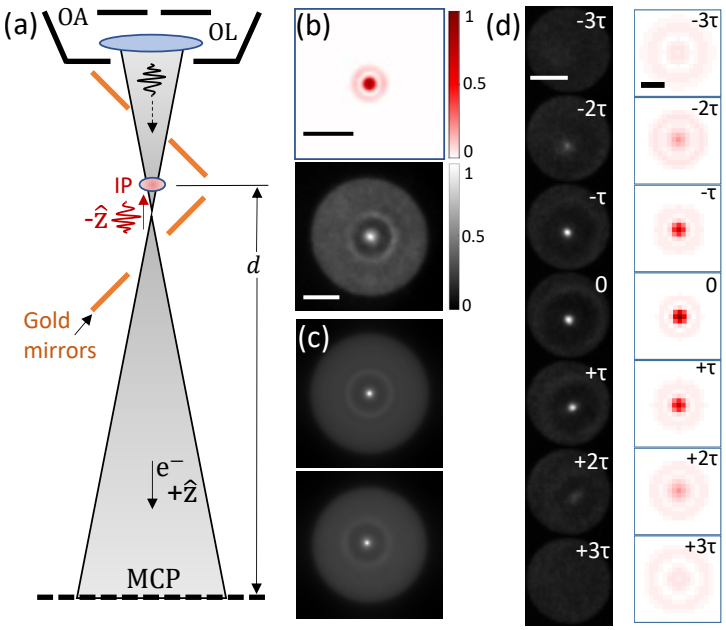


Figure 5.5: Ponderomotive electron-light interaction: (a) An SEM objective lens (OL) focuses the electron pulse to a crossover slightly below the IP. The OA is set to 100 μm. (b) (top) Light intensity distribution (scalebar 93 μm) before being demagnified (5x) to the interaction plane. (b)(bottom) Observed electron intensity distribution (scalebar 1 mm) at the detector plane. (c) wave optics (top) and ray optics (bottom) simulations of the detected electron beam are shown in (b). (d)(left) Detected electron distributions (scalebar 1.6 mm) when delaying the laser pulse with respect to the electron pulse by multiples of $\tau = 666$ fs. (d)(right) The delay causes the interaction to occur in a plane where the light is not focused. The new interaction plane occurs at multiples of $\delta z = v\tau/(1+v/c)$. The image has been reprinted from our publication [CMWS+22]. Matthias Schneller [Sch22a] has carried out the simulations in (c).

6 Transverse Phase Modulation of Electron-waves using Light

The following chapter describes the experimental realization of light-induced transverse spatial phase modulator of electrons and is based on our publication [CMWS+22]. The SLM-programmed laser intensity distributions imprint local phase shifts to the electron waves in free space. The shaped electron waves propagate freely and are detected by a position-sensitive MCP assembly. The interaction occurs in a high (up to $10\,\mu$J) laser pulse energy regime, so a clear electron intensity modulation is observed at the detector. However, for many wavefront shaping applications of electron waves, where small phase shifts up to 2π are required over a specific transverse area, less laser pulse energy is needed. The electron signal is kept low for all ponderomotive experiments to ~ 0.1 electrons per pulse (1 Mhz rep. rate) at the detector plane to minimize the pulse broadening.

The arbitrary local phase shift induced to the electron wave can be calculated using Eq. 2.38. Complex light-based electron beam modulation is shown in sub-chapter 6.1. Furthermore, both convex and concave laser-based lenses for electrons having focal lengths similar to current (S)TEMs, are demonstrated in sub-chapter 6.2.

6.1 Programmable electron beam shaping

To demonstrate programmable electron beam shaping, we selectively apply aberrations to our light pulse using the SLM, and show that this leads to characteristic distortions of our electron beam. Figure 6.1 shows a series of light intensity distributions measured in the conjugate plane (before 5x demagnification) using a CMOS camera. The phase masks required to diffract the source beam into those distributions are displayed on the SLM. The phase masks are programmed in the following way: First, a phase mask (ϕ_G) was calculated by back-propagation from the Fourier plane to the SLM plane. During this step, the beam block is implemented into the back-propagation (see Fig. 4.2 for details) to minimize losses along the beam path. Furthermore, using the back-propagation code, the laser focal spot is separated from the undiffracted SLM light, and the x-y position is optimized with respect to the electron beam. The algorithm automatically superposes the required blazed grating. Second, additional aberrations of the focal spot have been minimized by adding a correction phase ϕ_{cor} based on Zernike polynomials. Along the beam path towards the interaction plane, spherical aberrations and vertical astigmatism accumulated and had to be corrected. Third, the first 21 Zernike phase patterns ϕ_Z (see Fig. 6.2) have been added to the diffractive phase masks to intentionally aberrate the laser

spot (see Fig. 6.1) to investigate how the transverse modulation of the electron changes. The cartesian form of the first 21 Zernike polynomials used to generate the 2D phase mask and create the patterns in Fig. 6.1 are listed in table 6.1. The Zernike polynomials superposed to the phase mask are denoted as $a_{\mathrm{m,n}} \times Z_n^m$, whereas $a_{\mathrm{m,n}}$ represents the amplitude of the phase pattern and is set to a fixed value of π. A Matlab code has been adapted to generate the Zernike phase patterns [Fri]. The phase masks that give rise to the focal spots shown in Fig 6.1 have the following form:

$$\phi_{SLM} = \mathrm{modulo}2\pi[\phi_G + \phi_{\mathrm{cor}} + \phi_Z], \tag{6.1}$$

with $\phi_{cor} = (1.3 * \pi * Z_0^4 + 0.5 * \pi * Z_2^2)$ the correction phase mask. The coefficients of Zernike polynomials used to correct aberrations are optimized by measuring the laser focal spot directly in the interaction plane with a miniaturized CMOS (OV5647). Typical holograms (ϕ_Z) superimposed on the SLM used to modulate the electron beam in Fig. 6.3 are displayed in Fig. 6.2.

Figure 6.3 shows the electron distribution at the detector after propagation from the programmed, light-induced ($6\,\mu$J), phase modulated electron beams. The electron beam radius in the IP is set at $\rho_0 = 17.5\,\mu$m, whereas the distance from the IP to the electron focal spot is $d_c = 5.9\,$mm. Note that the scattered electron signal can also be used to evaluate the shape of the laser beam directly.

Arbitrary deflection of electron beams is shown in Fig. 6.4 by shaping the laser into arbitrary intensity profiles (see Fig. 4.7(top)). The modified GSA (20 iterations) has been used to shape the Gaussian source beam into a 'Smiley', letter 'O' and letter 'ψ'. The diffractive phase mask to be displayed on the SLM can be written as follows (see sub-chapter 4.3 for details):

$$\phi_{\mathrm{SLM}} = \mathrm{modulo}2\pi[\phi_{\mathrm{GSA}} + \phi_{\mathrm{cor}}], \tag{6.2}$$

where ϕ_{cor} has the same coefficients as in Eq. 6.1, and the ϕ_{GSA} is calculated as described in Fig. 4.2. Figure. 6.4 shows an electron distribution resembling a 'Smiley' ($\sim \rho_0 = 24\,\mu$m, $6\,\mu$J), letter 'O' ($\sim \rho_0 = 33\,\mu$m, $6\,\mu$J) and 'ψ' ($\sim \rho_0 = 46\,\mu$m, $10\,\mu$J) after interaction with the laser distribution in Fig. 4.7. For generating more complex electron intensity distributions, like the 'ψ' in Fig. 6.4(right), the reconstructed image suffers from unwanted intensity fluctuations. Having target images with only a few pixels and a beam block ($>D_{\mathrm{bb}} = 1\,$mm) in the iteration code (see sub-chapter 4.3.2 for details) make the speckle-suppression method inefficient.

Wavefront shaping applications of electrons require less pulse energy. Standard (S)TEM's provide sufficient coherence in the plane of phase shifting elements [VBMC+18] with an electron beam radius of $\rho_{\mathrm{coh}} \sim 25\,\mu$m. Thus, for wavefront shaping applications of electron beams, the radius of the shaped laser beam in the IP should be $\sim\rho_{\mathrm{coh}}$. Considering the finite resolution of our laser focal spot in the IP and the ρ_{coh} limit, we can individually program $\sim 10 \times 10$ pixels. For 30 keV, the pulse energy density required to induce

ponderomotive phase shifts of π is $0.29\,\mathrm{nJ}/\mu\mathrm{m}^2$. For shaping potentials on a disk over ρ_{coh} by π phase electron modulation, a pulse energy of $E_L = 0.57\,\mu\mathrm{J}$ is required.

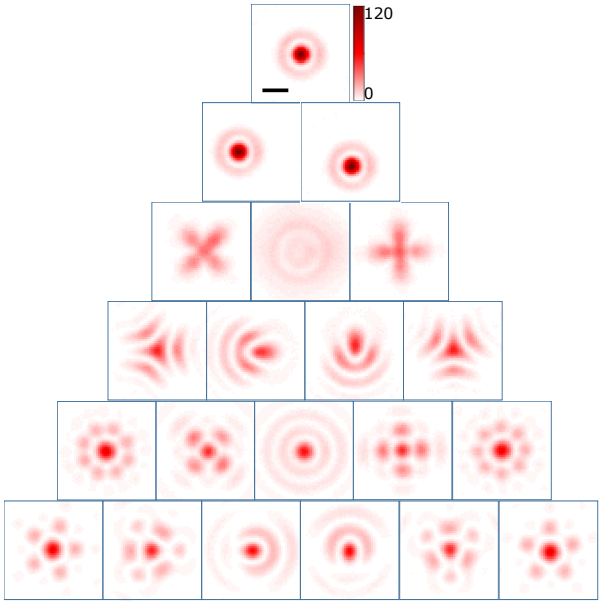


Figure 6.1: The intensity distribution of the intentionally aberrated focal spots is measured in the conjugate plane with the CMOS (scalebar 55 microns).

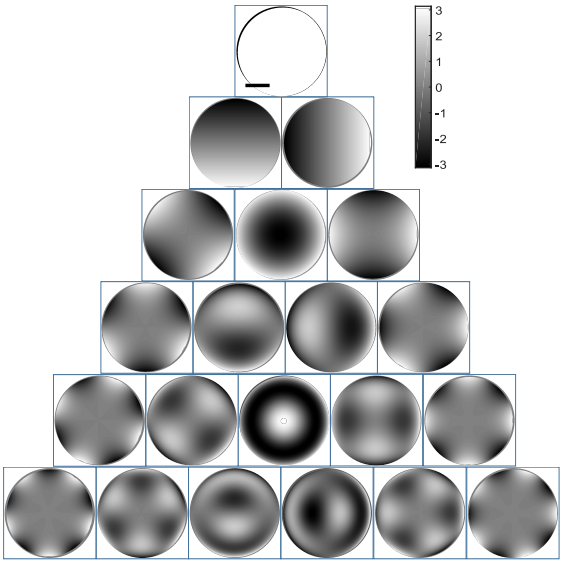


Figure 6.2: Phase masks superimposed on the SLM to modulate the electron beam with Zernike phase patterns. (scalebar 2.9 mm)

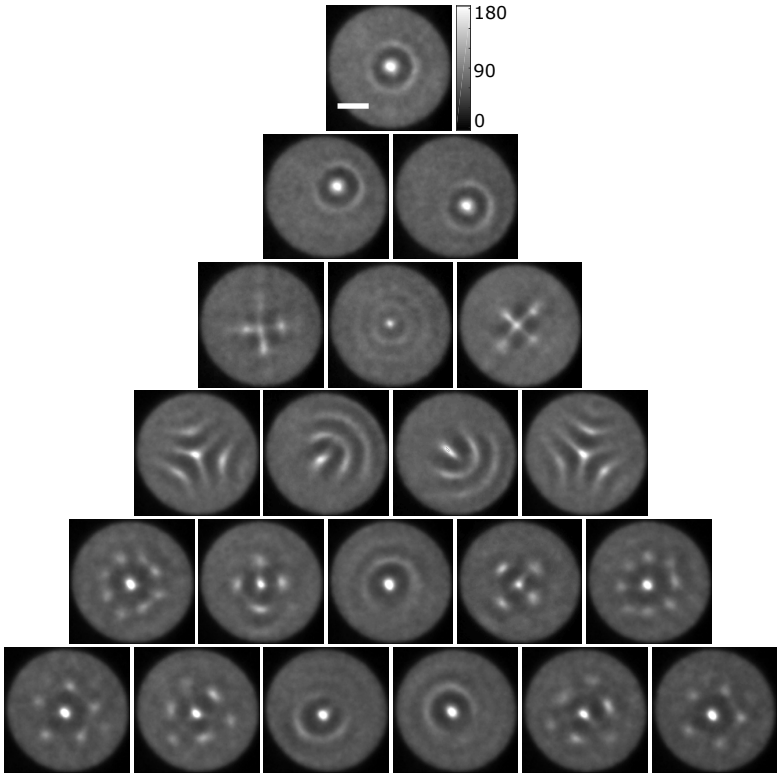


Figure 6.3: Ponderomotive phase modulation of electron beams at high laser beam intensities (6 μJ, scalebar 0.9 mm). Detected electron distribution at the screen after the interaction with SLM-shaped laser focal spots. The images resembling vertical astigmatism, trefoil, and coma have been reprinted from our publication [CMWS$^+$22].

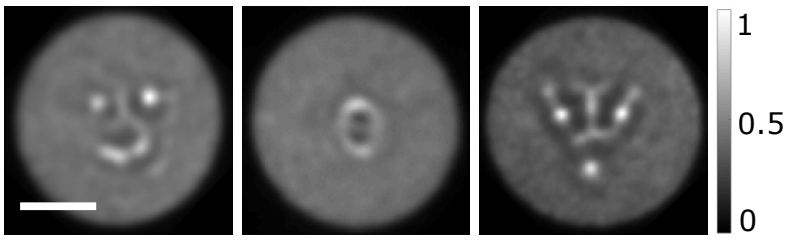


Figure 6.4: Arbitrary transverse phase modulation of electron waves. Electron distributions resembling a 'Smiley' (scalebar 1.2 mm), the letter 'O', and the letter 'ψ' were measured at the screen after light-induced transverse phase modulated electron beams. The 'Smiley' has been reprinted from our publication [CMWS$^+$22].

Cartesian form	n	m	Z_n^m
1	0	0	Z_0^0
x	1	-1	Z_1^{-1}
y	1	1	Z_1^1
2xy	2	-2	Z_2^{-2}
-1+2x^2 + 2y^2	2	0	Z_2^0
-x^2 + y^2	2	2	Z_2^2
-x^3 + 3xy^2	3	-3	Z_3^{-3}
-2x+3x^3 + 3xy^2	3	-1	Z_3^{-1}
-2y+3y^3 + 3x^2y	3	1	Z_3^1
y^3 − 3x^2y	3	3	Z_3^3
-4x^3y + 4xy^3	4	-4	Z_4^{-4}
-6xy+8x^3y + 8xy^3	4	-2	Z_4^{-2}
1-6x^2 − 6y^2 + 6x^4 + 12x^2y^2 + 6y^4	4	0	Z_4^0
3x^2 − 3y^2 − 4x^4 + 4y^4	4	2	Z_4^2
x^4 − 6x^2y^2 + y^4	4	4	Z_4^4
x^5 − 10x^3y^3 + 5xy^4	5	-5	Z_5^{-5}
4x^3 − 12xy^2 − 5x^5 + 10x^3y^2 + 15xy^4	5	-3	Z_5^{-3}
3x-12x^3 −12xy^2 +10x^5 +20x^3y^3 +10xy^4	5	-1	Z_5^{-1}
3y-12y^3 −12x^2y +10y^5 +20x^2y^3 +10x^4y	5	1	Z_5^1
-4y^3 + 12x^2y + 5y^5 − 10x^2y^3 − 15x^4y	5	3	Z_5^3
y^5 − 10x^2y^3 + 5y^4x	5	5	Z_5^5

Table 6.1: The first 21 Zernike polynomials are expressed in cartesian form. Algebraic expressions are taken from [LF11].

6.2 Ponderomotive lensing

In this chapter, we experimentally create both convex and concave laser-based electron lenses. The phase shift induced by an ideal lens for electrons of wavelength λ_e increases (concave) or decreases (convex) with the distance $\rho = \sqrt{x^2 + y^2}$ from the optical axis:

$$\varphi_{\text{lens}}(\rho) = -\frac{\pi}{f\lambda_e}\rho^2. \tag{6.3}$$

The sign of the focal length f is negative for concave and positive for convex lenses. Figure 6.5 shows the propagation (using Eq. 4.18) of an LG00 and LG10 beam and illustrates how the strong ponderomotive potentials affect the electrons. Note that the optical path lengths of the electrons from the lens to the focal spot have to be the same. This requires the effective index of refraction induced to the electrons by the electromagnetic field to be smaller than 1.

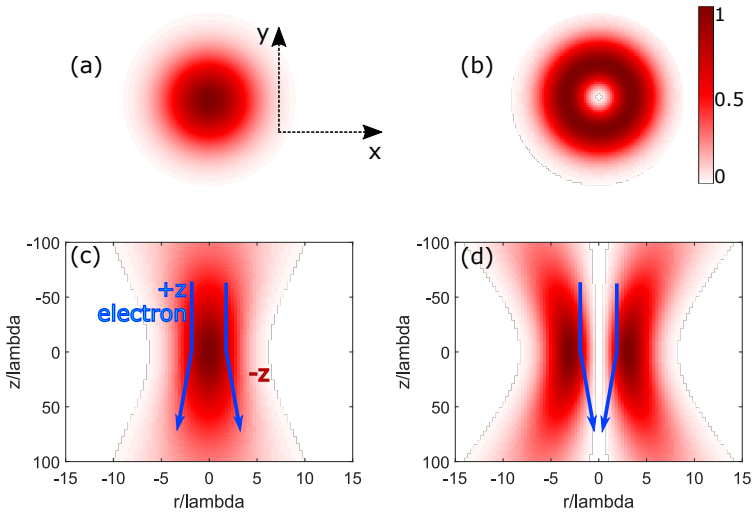


Figure 6.5: Ponderomotive Lensing. (a),(b) 2D cross-cut of the LG00 and LG10 focal spot in the transverse x-y plane. (c) 2D cross-cut of the LG00 mode ($w_0 = 3.7\,\mu$m, $\lambda_L = 1.035\,\mu$m) in the z plane. (d) 2D cross-cut of the LG10 mode ($w_0 = 4.5\,\mu$m, $\lambda_L = 1.035\,\mu$m) in the z plane. The blue arrows illustrate the change in electron trajectory due to the ponderomotive momentum kick. The electrons propagate in the opposite direction (+z) to the motion of light (-z) and are deflected towards regions of lower intensity. The electron trajectories are not to scale.

Conventional magnetostatic, radially symmetric electron lenses can only be constructed to be convex. Electrostatic lenses can also be built to be concave; however, in this case, the electron energy cannot be preserved.

6.2.1 Laser pulse energy loss along the beam path

There is significant pulse energy loss along the beam path towards the interaction plane. These losses are associated with the SLM, and finite reflectivity/transmissivity of used light optics.

The total efficiency of the specific shaped light distribution can be determined in a two-step process. First, a power meter will measure the total pulse energy before the SLM. Afterward, pulse energy in the interaction plane is measured with a calibrated CMOS camera. From this first step, the transmission $T_{\mathrm{C_L}} = 0.275$ is determined (see appendix 10.1 for details). However, not all of the light in the interaction plane is actually found within the desired light pattern. Scattering and inefficiencies in the wavefront shaping lead to additional losses, which have to measured carefully in order to correctly quantify the strength of the phase shifting light fields. This is especially important for pulse energy loss, which originates from the stray scattered light around the specific light distribution. This additional loss has been quantified only for the LG00 and LG10. The net usable pulse

energy in each mode is determined by fitting the LG00, or LG10 in the CP, and measuring it's residuals (see Fig. 6.6). The intensity inside the fit for LG00 (LG10) represents $T_{00} \sim 45\%$ ($T_{10} \sim 56\%$) of the total intensity shown in Fig. 6.6(a) (Fig. 6.6(e)). The net pulse energy transmission for the LG00 is $T_{\mathrm{LG00}} = T_{\mathrm{c_L}} \times T_{00} = 0.45 \times 0.275 = 0.123$. The net pulse energy transmission for the LG10 is $T_{\mathrm{LG10}} = T_{\mathrm{c_L}} \times T_{10} = 0.56 \times 0.275 = 0.154$. For example, in order to have $1.54\,\mu$J pulse energy in the LG10 for the ponderomotive interaction, we need $10\,\mu$J pulse energy outside vacuum before the SLM. The LG10 measured in Fig. 6.6(d) has a residual intensity in center, which deviates from the ideal LG10 distribution. Therefore, the distribution from Fig. 6.6(d) is fitted with a sum of LG10 and a LG00, which is illustrated by the orange curve in Fig. 6.6(e). We found out that the reason for this residual intensity is the sign of the vortex phase that was used to generate the LG10 mode. Unfortunately, this diagnosis came after we did all the ponderomotive scattering experiments. In the following sub-chapters 6.2.2,6.2.3 we will use the LG00 and LG10 shown here to create concave and convex electron lenses.

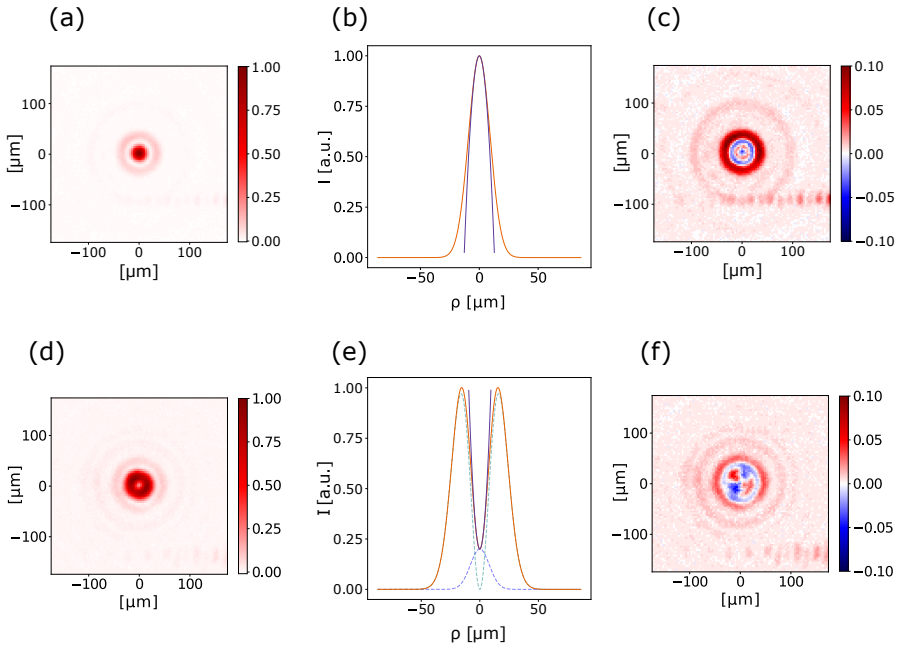


Figure 6.6: (a) Spatial intensity distribution of the LG00 beam measured in the conjugate plane. (b) Crosscut showing the fit (orange) of the LG00 mode and its quadratic Taylor expansion around $\rho = 0$ (violet). (c) Residuals of an LG00 fit to the distribution. (d) Spatial intensity distribution of the LG10 beam measured in the conjugate plane. (e) Crosscut showing the fit (orange), its LG10 (turquoise), and LG00 (blue) component, as well as the quadratic Taylor expansion around $\rho = 0$ (violet). (f) Residuals of a fit to the distribution. The fit function is a sum of a dominant LG10 mode and a minor LG00 mode. Figure reprinted from [CMWS+22].

6.2.2 Laser-based concave lens for electrons

Theoretical focal length derivation of the ponderomotive concave lens

The intensity distribution of a Gaussian laser beam can be calculated from Eq. 4.18 and takes the following form:

$$g_{00}^2(\rho) = \exp\left(-2\frac{\rho^2}{w_{00}^2}\right). \tag{6.4}$$

The Taylor expansion of the LG00 shows a quadratic spatial distribution close to the optical axis $g_{00}^2(\rho) \approx 1 - 2\rho^2/w_{00}^2 + \mathcal{O}(\rho^4/w_{00}^4)$.

We can determine the focal length of the ponderomotive concave lens in the following way. First, we plug Eq. 6.4 into the denominator of Eq. 2.38 and the first term of the Taylor expansion into the numerator. Second, we make a coefficient comparison between the quadratic term of the new Eq. 2.38 and Eq. 6.3, and we solve for the focal length f. We arrive at the analytical function, which is expressed as:

$$f_{00}(E_L) = -(1 \mp \beta)\frac{\pi^3 w_{00}^4 E_e}{2\alpha\lambda_L^2\lambda_e}\frac{1}{E_L}. \tag{6.5}$$

Experimentally determined focal length of the ponderomotive concave lens

The LG00 is placed right above the electron crossover ($d_c \sim 241\,\mu$m), whereas the electron beam is set to illuminate only the central ($R \sim 0.8\,\mu$m) part of the laser intensity where the quadratic distribution holds. Thus, a decreasing quadratic transverse phase shift from the optical axis is imparted to the electron wave function, such that a concave electron lens is created. Figure 6.7(d) shows the measured electron beam diameter $D = 2\rho_s$ at the screen (orange dots) as a function of E_L. The linear fit (orange line) and the theoretical dashed curve are also shown. Due to the 5% uncertainty in the w_{00} determination, an additional gray region was added to the theoretical curve. The analytical expression for the theoretical curve shown in Fig 6.7(d) is calculated as follows:

$$\rho_s(E_L) = \rho_0\left(1 - \frac{d}{f_{00}(E_L)}\right) + d \cdot \theta_{\rho,0}, \tag{6.6}$$

with the outermost incoming rays defined by ρ_0 and initial angle $\theta_{\rho,0}$.

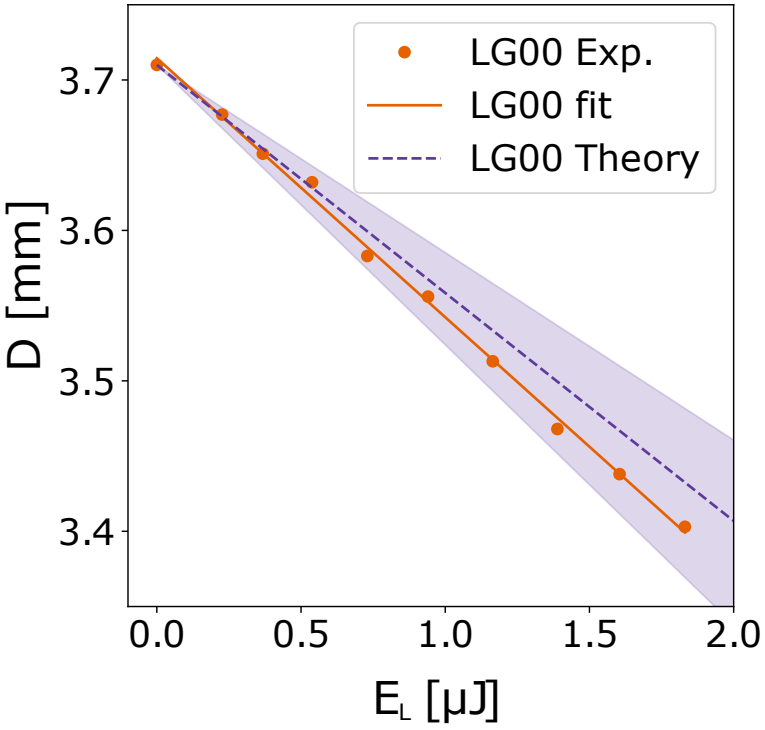


Figure 6.7: The diameter of the electron beam at the detector plotted as a function of laser pulse energy, along with the theory and a gray error region due to our error in determining the waist of the LG00 mode. Figure reprinted from [CMWS+22].

The measured electron beam diameter at the screen (see Fig. 6.7) has been determined by doing an ellipse fit to the raw electron images and extracting the minor and major axis. Further, the geometric mean of the minor and major axis will yield the D shown in Fig. 6.7. The analysis has been carried out using the Otsu segmentation method in the image processing tool Fiji [SACF+12].

Figure 6.8(a)(left) shows a simple schematic that illustrates how the electron beam is placed in the quadratic region of the LG00 mode. A ray optics model is used to determine the focal length of the ponderomotive lens:

$$\begin{pmatrix} \rho_s \\ \theta_s \end{pmatrix} = \begin{pmatrix} 1 & d \\ 0 & 1 \end{pmatrix} \begin{pmatrix} 1 & 0 \\ \frac{-1}{f} & 1 \end{pmatrix} \begin{pmatrix} \rho_0 \\ \theta_{\rho,0} \end{pmatrix}. \tag{6.7}$$

We eventually arrive at $f = d \cdot \rho_0/(\rho_0 - \rho_s + d \cdot \theta_{\rho,0})$, where θ_s is the convergence angle after the passing through the lens.

The laser-based lens is concave; however, because the LG00 is placed above the electron cross-over, a focusing effect is visible Fig. 6.8(b)(left) at the screen ($E_L = 2.5\,\mu$J) when compared to the electron distribution (Fig. 6.8(b)(center)) with the laser beam turned off.

Furthermore, Fig. 6.8(c)(blue, green, data sets) shows the concave ponderomotive lens's deducted negative focal length as a function of laser pulse energy. The analytical focal length (Eq. 6.5) is plotted against the measured E_L with a 5% error (gray area), which is determined from the uncertainty of the w_{00}.

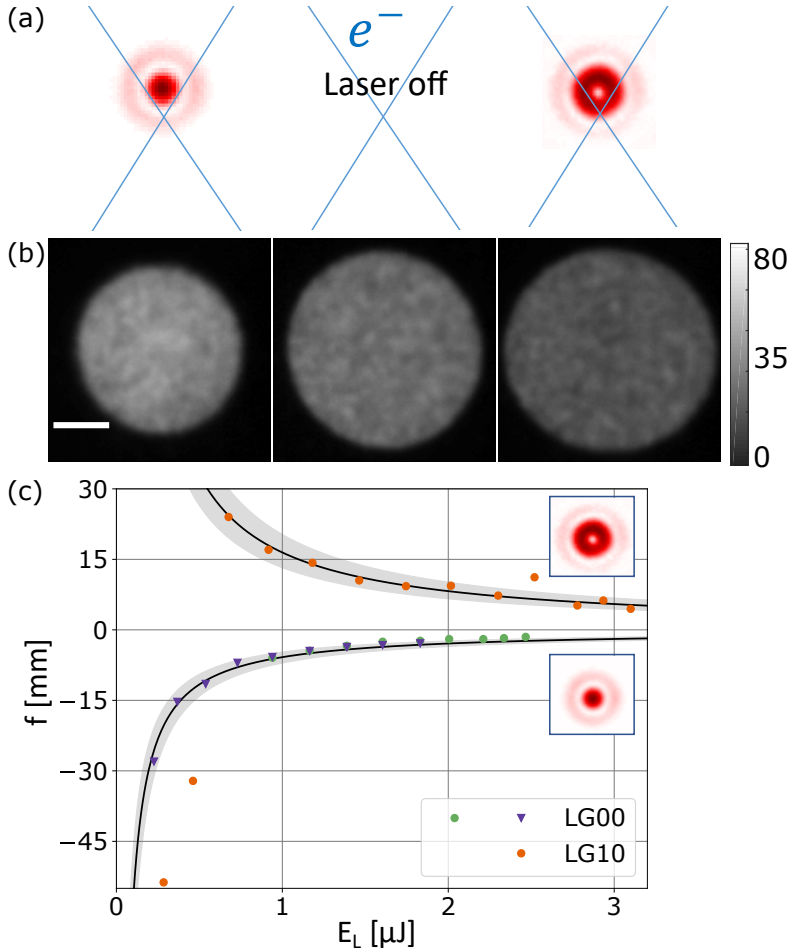


Figure 6.8: Light-based electron lenses: (a) Schematic of the experimental setup used for creating the ponderomotive lensing. The electron beam is focused slightly below the laser focal spot. (a),(left) The electron beam is placed in the quadratic region near the optical axis of a Gaussian beam. The laser was turned off in (a),(center). (a)(right) The electron beam is placed in the quadratic region near the optical axis of a LG10. (b) Detected electron distribution with concave (left, LG00), no (center), and convex (right, LG10) ponderomotive lens (scalebar 1 mm). (c) Focal length as a function of laser pulse energy for LG00 (green and violet) and LG10 (orange) mode. The inset shows the respective light intensity distributions, measured in a plane conjugate to the interaction plane. This figure is adapted from [CMWS+22].

6.2.3 Laser-based convex lens for electrons

Theoretical focal length derivation of the ponderomotive convex lens

Analogous to sub-chapter 6.2.2, we now derive the theoretical focal length of the convex laser-based lens for electrons. The intensity distribution of a Laguerre-Gaussian laser beam can be calculated from Eq. 4.18 and takes the following form:

$$g_{10}^2(\rho) = \frac{\rho^2}{w_{10}^2} \exp\left(-2\rho^2/w_{10}^2\right), \tag{6.8}$$

The Taylor expansion of the LG10 beam $g_{10}^2 \approx \rho^2/w_{10}^2 - \mathcal{O}(\rho^4/w_{10}^4)$ shows a quadratic spatial distribution close to the optical axis. Hence, if the electron beam is placed near the optical axis of a LG10 beam, an increasing quadratic transverse phase shift with the optical axis will be imparted onto the electron wave function. Thus, a convex electron lens is created. The analytical focal length takes the following form:

$$f_{10}(E_L) = (1 \mp \beta)\frac{\pi^3 w_{10}^4 E_e}{2\alpha\lambda_L^2\lambda_e}\frac{1}{E_L}. \tag{6.9}$$

Recall that the upper sign is for copropagating and the lower for counterpropagating laser and electron pulses.

Experimentally determined focal length of the ponderomotive convex lens

To create a convex light-based electron lens, we keep the same electron beam parameters that we have in sub-chapter 6.2.2. However, instead of LG00, we now place the LG10 right above the electron crossover ($d_c \sim 241\,\mu$m), whereas the electron beam illuminates the central ($R \sim 0.8\,\mu$m) part of the LG10. Figure 6.9(d) shows the measured electron beam diameter $D = 2\rho_s$ at the screen (orange dots) as a function of E_L. The linear fit (orange line) and the theoretical dashed curve are also shown. Furthermore, due to the 5% uncertainty in the w_{10} determination, an additional error (gray) region was added to the theoretical curve in Fig 6.9(d). As expected, the radius ρ_s of the electron beam measured at the screen increases linearly with the pulse energy.

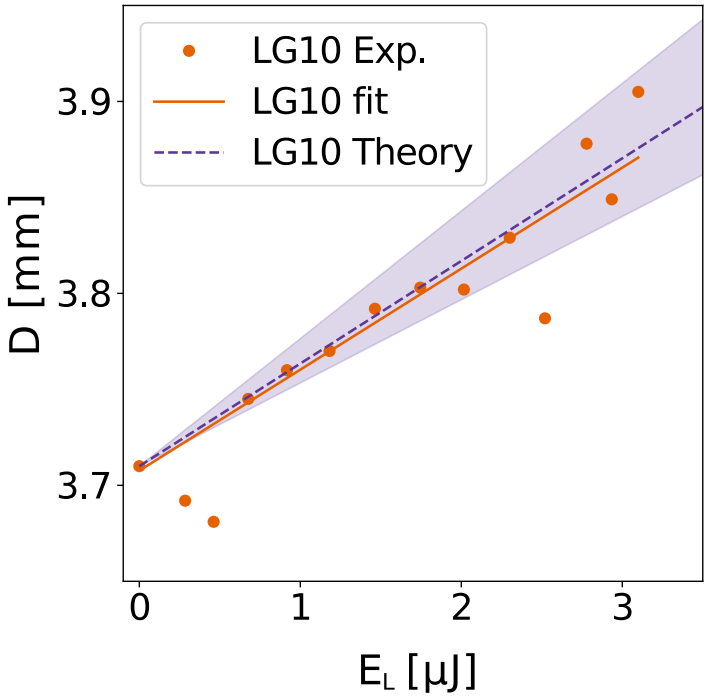


Figure 6.9: The diameter of the electron beam at the detector and its linear fit, plotted as a function of laser pulse energy, along with the theory and an error region due to our error in determining the waist of the dominant LG10 component. Figure reprinted from [CMWS+22].

In Fig. 6.8 we demonstrate the convex light-based lensing of electrons. Figure 6.8(a)(right) shows a simple schematic of the electron light interaction. Figure 6.8(b)(right) shows the measured electron distribution at the screen after interaction with the LG10 (3.1 μJ). The electron distribution in Fig. 6.8(b)(right) is slightly asymmetrical. The cylindrical lensing can be explained by the high sensitivity of the LG10 mode to astigmatism. Nevertheless, it should be possible in future experiments to optimize the shape of the light field directly by having the ponderomotive scattering signal as feedback.

Figure 6.8(c) shows the deducted focal length of the convex lens (orange data) as a function of pulse energy. The deducted focal length has been calculated analogously to sub-chapter 6.2.2. The solid black line in Fig.6.8(c)(top) is the analytical focal ($f_{10}(E_L)$, Eq. 6.9) length plotted together with the error (gray shaded area) as a function of pulse energy.

Our theoretical model explains the experimental data well, except for the data points taken for the convex lens for low pulse energy values. When the scattering angles are small, it becomes challenging to align the electron beam at the center of the LG10 beam, which can result in a change of sign in $f(E_L)$. Also, if the pulse energy is increased over

$\sim 2.4\,\mu$J, the laser beam becomes unstable (most likely due to thermal effects induced to the probe forming mirror). This increases the error in determining the ρ_s at the screen (see Fig. 6.9(d)) and, consequently, the $f(E_L)$. Nevertheless, at high laser pulse energies, focal lengths down to 1.6 mm are achieved, which is comparable to the performance of current (S)TEMs. Furthermore, with our current setup, $\sim 5\%$ of the pulse energy is lost in the beam hole at the mirror. The hole at the mirror could be reduced in diameter, and the coating optimized for higher reflectivity. Note that a reduction in hole size would also increase the diffraction efficiency of the back-propagation code. Furthermore, thermal effects can be minimized in future setups by replacing the copper mirrors with a substrate of low thermal expansion. Also, the laser beam size at the mirror surface could be increased, such that losses at the hole become negligible.

6.2.4 Moving the interaction plane in the z-direction

Next, we show that our setup allows altering the axial position of the interaction plane with very few adjustments. This could be used for aligning the interaction plane to the back focal plane of an electron objective lens.

Keeping the electron beam settings constant, we shift the interaction plane of the LG00 beam by first changing the delay ($\delta z = v\tau/(1 + v/c) = 837\,\mu$m, $\tau = 11.3$ ps) between the electrons and the light pulses, and then adding a defocus phase mask ($\phi_{\text{defocus}} = -7 \times \pi \times Z_2^0$) on the SLM. We demonstrate this in Fig. 6.10, where we see a focusing (Fig. 6.10(a)) and defocusing (Fig. 6.10(f)) effect on the detector plane. The electron beam settings are kept constant, as in Fig. 6.8.

-	Major [p_x]	Minor [p_x]	D [mm]
focusing	145.59	141.74	3.11
laser off	173.75	167.81	3.71
defocusing	203.1	193.81	4.3

Table 6.2: Determining the electron beam diameter at the screen for the focusing (Fig. 6.10(b),(left)), laser off ((Fig. 6.10(b),(center)), and defocusing ((Fig. 6.10(b),(center)) electron beam. The same LG00 is used at the shifted interaction plane.

The diameters of the electron distributions in Figs. 6.10 have been determined by fitting the data with an ellipse [Gal] and extracting the Major and Minor axis. The electron beam diameter at the screen is defined as the geometric mean of the Minor and Major axis of the ellipse fit $D = 2\rho_s = \sqrt{Major \times Minor} \times p_x$, where $p_x = 21.7 \times 10^{-6}$ is the calibrated pixel value from an image that contains the whole MCP disk. The values are listed in table 6.2.

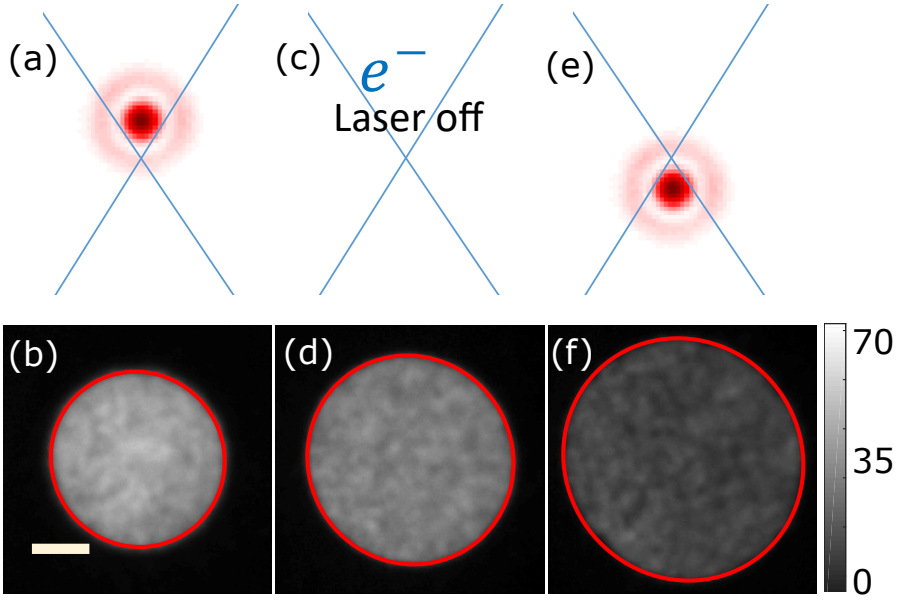


Figure 6.10: Changing the interaction plane of the concave ponderomotive lens. (a) Placing the LG00 above the electron crossover leads to a focusing effect of the electron beam on the screen (b). (c) and (d) are the schematic of the electron beam with the laser off and the corresponding electron distribution, respectively. (e) Placing the LG00 below the electron crossover leads to a defocusing effect of the electron beam on the screen (f). The diameter of the electron beam at the screen is determined by fitting the electron distribution with an ellipse where the rising edge is 40%. Electron distributions in (b) and (d) are the same as in Fig. 6.8(b),(left),(center), and are reprinted here to illustrate clearly how altering the axial position changes the propagation direction of electrons.

7 Diagnosis of electron microscope aberrations

Light-based transverse modulation of the electron phase could be used to correct the spherical aberrations of the electron beam and is a future application of our setup. However, when correcting for the aberrations of the electron probe-forming lens, it is essential to identify and characterize the aberrations. Coherent diagnostic techniques vary from measuring diffractograms [Sax00] to recording electron Ronchigrams from amorphous or crystalline samples [Cow79, LC86, KDL99, JB99, Liu05, YKKW06, SSH$^+$08, SRL$^+$18]. Furthermore, shadow images from fine [MPSC06] gratings can provide information about the properties of the focal spot where the coherent techniques are too challenging to be implemented [SF42, Rem85, RDSG97].

In this chapter, various parameters that influence the achievable electron probe size, as well as the Ronchigram method, are described. We will then explain how such measurements could be used to correct the aberrations of the electron beam with light-based phase plates.

7.1 Probe size limiting factors in electron microscopy

The electron microscope was invented by Knoll und Ruska [KR32], and shortly afterward, a theoretical paper was published by Scherzer [Sch36a] highlighting the inevitable spherical and chromatic aberrations of the electron lenses (see Fig. 7.1(b),(c)). This is known in the literature as the Scherzer theorem and states that rotationally symmetric, static, and free-of-charge lenses suffer from aberrations that limit the achievable resolution [Sch47] of the electron microscope. The first aberration correction has been realized in a low energy SEM [ZH95] at beam energies between $E = 0.5 - 1\,\mathrm{keV}$ while improving the spatial resolution of the instrument from 5.6 nm to $\sim 2\,\mathrm{nm}$. The first spherical aberration correction in a TEM that managed to improve the spatial resolution was realized shortly afterward [HRU$^+$98].

Without the aberrations, the theoretical diffraction-limited resolution of the electron microscope is given by [Sch49]:

$$d_d = 0.6\lambda_e / \sin\theta, \tag{7.1}$$

where $\theta \simeq R/f$ is the semi-convergence angle of the electron beam. In electron microscopy, chromatic and spherical aberrations are the dominant factors that degrade the achievable

resolution. Figure 7.1 shows a simplified ray optics sketch of how spherical and chromatic aberrations affect the size of the focal spot. An ideal convex lens will impart a quadratic phase shift to the electron wave that increases with distance from the optical axis (see 6.3), which would focus the electron to a diffraction-limited spot size (see Fig. 7.1). The blur caused by these aberrations can be estimated by [ZH95]:

$$d(C_c) = \sqrt{1.2\lambda_e \frac{\Delta E}{E} C_c}, \tag{7.2}$$

$$d(C_s) = \sqrt[4]{0.12\lambda_e^3 C_s}, \tag{7.3}$$

where λ_e is the electron wavelength, ΔE the energy spread of the electron beam, C_c the chromatic aberration coefficient, and C_s is the dominant third-order spherical aberration coefficient. The final achievable resolution (d_p) can be estimated by adding the resolution limits in quadrature [KCD$^+$08, Rei13]:

$$d_p = \sqrt{d_d^2 + d^2(C_s) + d^2(C_c)}. \tag{7.4}$$

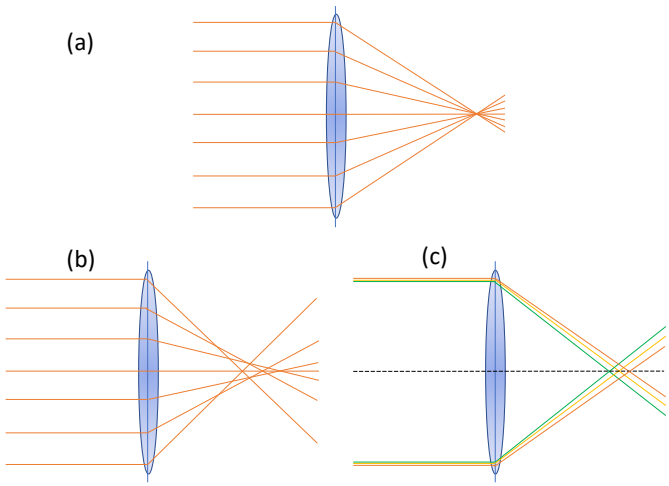


Figure 7.1: Primary aberrations of the electron probe-forming objective lens. (a) An ideal lens focuses the rays onto the Gaussian focal point achieving diffraction-limited probe size. (b) Spherical aberrations cause the incoming rays at the lens plane that are further apart from the optical axis to be focused before the Gaussian focal point. (c) Chromatic aberrations cause the electrons, which have a slightly different energy from the mean electron energy, to be focused before or after the Gaussian focal point.

Typical aberration coefficients (C_s, C_c) of scanning transmission electron microscopes (STEMs) and TEMs are in the order of millimeters. Note that at low electron energies $\sim 1\,\mathrm{keV}$, the resolution degradation due to chromatic aberrations (see Eq. 7.2) is more significant than the spherical aberrations; therefore, both types of aberrations must be

considered for an effective resolution improvement. Nowadays, there are hundreds of aberration correctors based on multipole lenses that are implemented all over the world in electron microscopes [HHM+09]. The first-order chromatic aberrations will induce a defocus δ_c due to the energy spread in the beam, as follows [ZH95]:

$$\delta_c = C_c \frac{\Delta E}{E} = C_c \frac{(E_i - E)}{E}, \tag{7.5}$$

where E is the mean electron energy and E_i the energy of each electron. From Eq. 7.5 it is clear that the defocus induced to the electron probe is proportional to the relative energy spread. Using a CFEG [HCW+18] and accelerating the electrons to higher energies will therefore minimize the chromatic contribution. Also, modern electron microscopes are equipped with monochromators [BRK12] which further reduce the energy spread at the cost of losing beam current.

Spherical aberrations will cause the marginal rays to focus before the image plane. In the wave picture, the spherical aberrations distort the electron phase in the following way:

$$\chi(\theta) = \frac{2\pi}{\lambda}(C_s\theta^4 - 2\Delta z\theta^2), \tag{7.6}$$

where the first term is due to the spherical aberrations and the second term is due to an intentionally induced defocus Δz. It is often set to the Scherzer defocus [Sch36b], which minimizes the spherical aberrations at the edge of the aperture:

$$\Delta z = 0.5 C_s \alpha_{max}^2. \tag{7.7}$$

where $\alpha_{\max}$ is the maximum convergence semi-angle. One can also rewrite Eq. 7.6 in terms of spatial frequency $k = \theta/\lambda$:

$$\chi(k) = \frac{\pi}{2}(C_s\lambda^3 k^4 - 2\Delta z\lambda k^2). \tag{7.8}$$

Neglecting the mechanical and electromagnetic stability and assuming a constant amplitude at the objective lens aperture and perfect electron beam coherence, the wave function of the focused probe at the sample plane is approximated by:

$$\psi_p(w) = FFT(e^{i\chi(\theta,\phi)}), \tag{7.9}$$

where $w = x_1 + y_1$ are the coordinates in sample plane. The generalized aberration function $\chi = \chi(\theta, \phi)$ is defined in Krivanek notation [KDL99] as a function of convergence and azimuthal (ϕ) angle:

$$\chi(\theta, \phi) = \frac{2\pi}{\lambda_e} \sum_{n,m} C_{n,m}\theta^{n+1} \frac{cos[m(\phi - \phi_{n,m})]}{n+1} \tag{7.10}$$

where n and m are the order and degree of the aberrations, respectively. The intensity of the electron probe becomes:

$$I(w) = |\psi_p(w)|^2. \tag{7.11}$$

The influence of partial coherence on the intensity of the electron probe

This section also considers the partial coherence of the electron beam to evaluate the probe size at the sample plane. The electron beam's partial coherence also limits the electron microscope's achievable resolution [HUZ00, ERKD09]. An increase in the energy spread of the electron beam will decrease the longitudinal coherence (L_c) of the electron beam according to the following equation:

$$L_c = \frac{\lambda_e^2}{\Delta\lambda_e}. \tag{7.12}$$

with $\Delta\lambda_e$ being the spectral spread of the electrons. The spectral spread for nonrelativistic electrons can be calculated if the electron energy and spread are known, as follows [NH93]:

$$\lambda_e = \frac{h}{\sqrt{2m_eE}}. \tag{7.13}$$

Now we differentiate the de Broglie wavelength, and we get:

$$\Delta\lambda = -\frac{1}{2}\frac{\Delta E}{E}\frac{h}{\sqrt{2m_eE}}. \tag{7.14}$$

If we plug Eq. 7.14 into Eq. 7.12 and neglect the negative sign, we get the following:

$$L_c = 2\frac{h}{\sqrt{2m_eE}}\frac{E}{\Delta E} \tag{7.15}$$

The van Cittert-Zernike theorem [LL07, KLKB13, MH22] makes the connection between the width W of an interference pattern and the effective source size s_0 of an emitter. The angular spatial coherence function $\mu_{\mathrm{sc}}(\Omega)$ can be directly derived:

$$\mu_{\mathrm{sc}}(\Omega) = \exp\left[-(\frac{\pi\Omega s_0}{\lambda_e})^2\right], \tag{7.16}$$

where $\Omega \sim W/b$ is the angle between two split rays that interfere at the distance b from a beam splitter. The effective source size can be experimentally determined by measuring the visibility $(I_{\max} - I_{\min})/(I_{\max} + I_{\min})$ of the measured interference pattern, where $I_{\max}$ and $I_{\min}$ are the maximum and minimum intensity of the adjacent fringes. The demagnified source size S_d at the specimen can be written as follows [RSL+21b]:

$$S_d = \sqrt{\frac{4I}{\pi^2 E B_r}}\frac{1}{\alpha_{\max}}, \tag{7.17}$$

where I is the beam current at the sample plane, and B_r is the beam brightness defined in terms of current density and solid angle:

$$B_r = \frac{I}{(\pi(\frac{s_0}{2})^2)\pi\alpha_{\max}^2}. \tag{7.18}$$

The spatial intensity profile of the electron probe at the sample plane, when taking into account also the finite coherence, changes from Eq. 7.11 to an incoherent sum over electron energies [ERKD09]:

$$I(\boldsymbol{w}, E_i) = \int_{-\infty}^{\infty} dE_i \, [|\psi(\boldsymbol{w}, E_i)|^2 \otimes S(\boldsymbol{w})] \frac{dT(E_i)}{dE_i}, \tag{7.19}$$

where $\otimes$ denotes the convolution, $S(\boldsymbol{w}) = \frac{1}{\sqrt{2\pi\sigma_S^2}} \exp\left(\frac{-ww^*}{2\sigma_S^2}\right)$ is the contribution from the partial transverse coherence with $\sigma_S^2 = S_d^2/(8\ln 2)$ and $\frac{dT(E_i)}{dE_i} = \frac{1}{\sqrt{2\pi\sigma_T^2}} \exp\left(\frac{-(E_i-E)^2}{2\sigma_T^2}\right)$ is the partial temporal coherence contribution with $\sigma_T^2 = \Delta E^2/(8\ln 2)$.

Pulse broadening of electrons

For pulsed electrons, broadening effects represent an additional source of error compared to continuous mode electrons. The velocity spread (Δv) in the electron beam leads to electron pulse broadening [HBBC12]:

$$\sigma(t) = t\frac{\Delta v}{v}. \tag{7.20}$$

with the nonrelativistic electron energy:

$$v_e = \sqrt{\frac{2E}{m}}. \tag{7.21}$$

Differentiating leads to:

$$\Delta v = \frac{1}{2}\sqrt{\frac{2}{m_e E}}\Delta E. \tag{7.22}$$

Now we can rewrite Eq. 7.20 into:

$$\sigma(t) = t\frac{1}{2}\frac{\Delta E}{E}. \tag{7.23}$$

Our ponderomotive experiments are conducted at an electron energy of 30 keV, representing the maximum energy available. Thus, the pulse-broadening effects due to the initial velocity spread of electrons are minimized. Assuming a typical energy spread of the SFEG of 1 eV [FBR+17] and neglecting the acceleration of electrons, we can estimate that the electron pulse broadens due to Δv with 73 fs after $t \sim d_{\mathrm{tip-IP}}/v_e = 4.38$ ns. The distance from the electron gun to the IP is $d_{\mathrm{tip-IP}} \sim 45$ cm. The broadening due to velocity spread is negligible for our experiment.

The electron pulse can also broaden due to Coulomb repulsion. For our experiments, the number of electrons per pulse at the sample plane is ~ 0.1 to minimize this dispersion in pulse length. Nevertheless, the broadening occurs shortly after the electrons are emitted, where the electron flux is much higher. It has been shown in [KMS+18] (similar settings to our experiment) that this space charge effect can cause an electron beam at 30 keV

with an initial pulse length of 100 fs to arrive at the sample plane with a broadened pulse length of 400 fs. In addition to pulse broadening, space charge effects can lead to spatial decoherence [MH22], which degrades the contrast of phase sensitive experiments.

7.1.1 Ronchigram Simulation

The electron Ronchigram method is a valuable tool in characterizing the electron focal spot because the diffraction pattern from an amorphous or crystalline sample recorded in bright field mode is susceptible to any change of phase shift caused by defocusing or aberrations of the probe-forming lens. Furthermore, the presence or absence of interference fringes in the recorded Ronchigram can indicate incoherence broadening due to mechanical instabilities, electro/magnetic noise sources, or finite source size of the electron gun [JB99].

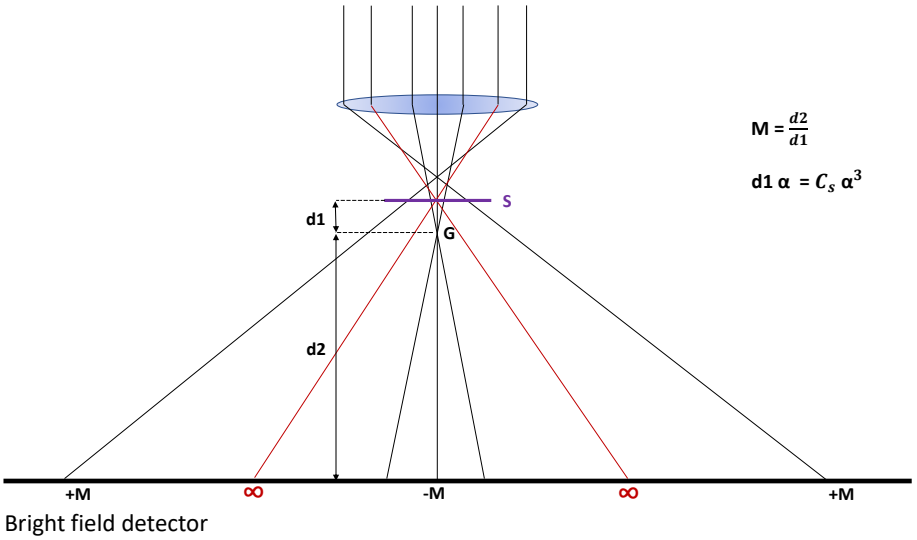


Figure 7.2: The electron Ronchigram schematic. An electron objective lens focuses the electron beam slightly below a sample containing a thin film of amorphous carbon. The shadow image of the carbon sample can be recorded in bright field mode by a position-sensitive detector. The magnification of the shadow image is given by the distance between the Gaussian focal point to detector and Gaussian focal point to the sample. As spherical aberrations make their presence, the rays further apart from the optical axis start to get focused above the Gaussian point until they are focused on the sample. When the rays reach the sample, the magnification is infinite and is illustrated in the shadow image by the rings of infinite magnification. As the rays progressively start to get focused above the sample, the magnification is reversed and starts decreasing. From a strongly defocused shadow image, the spherical aberration coefficient can be determined directly by measuring the radius of the rings with infinite magnification.

In this sub-chapter, Ronchigrams are simulated to find feasible experimental parameters that could be used for future proof-of-principle wavefront shaping experiments. For reasons of simplicity, the partial coherence contribution (see Eq.7.19) of the electron beam is not included in the simulations.

Figure 7.2 shows the schematic that allows visualizing aberrations in a STEM. The specimen 'S', e.g. a thin film of amorphous carbon, is placed slightly above the aberrated electron focal spot 'G' formed by the objective lens of the electron microscope. The paraxial magnification of the shadow image is $M = d2/d1$, where d2 is the distance between the Gaussian focal spot and detector, and d1 is the distance between the focal spot and the sample. The electron lens induces spherical aberrations to the electron beam, which causes the peripheral rays to be focused before the Gaussian focal spot. As the incident rays start to distance themselves from the optical axis, they get focused gradually above the Gaussian focal spot such that the magnification of the shadow image increases until infinity $d1- > 0$(see red rays in Fig. 7.2 that are focused onto the sample). When the crossover of the aberrated rays is at S, sharp rings with good contrast become visible.

The shadow image is reversed for the rays that form a crossover above the sample, and the magnification changes sign and starts decreasing. The third order spherical aberration coefficient can be determined directly by measuring the radius of the rings of infinite magnification and the paraxial magnification. The radius of the infinite magnification rings $d1\alpha$ can be set equal [Cow79] to $C_s\alpha^3$, and the third-order spherical aberration coefficient can be determined. Here, α is the angle formed by the optical axis with the cross-over (red in 7.2) at the sample plane. When the radius of infinite magnification is reduced to a minimum value, a region of uniform intensity is reached in the center of the Ronchigram, called the 'sweet spot'. From the radius of the sweet spot, the maximum aberration-free semi-angle can be determined. Also, the sweet spot appears at the optimum Scherzer defocus (see Eq. 7.7) used for phase-contrast imaging [Sch36a]. We now describe how an electron Ronchigram can be simulated. When an electron beam travels through a thin material film, it acquires a phase shift according to the following parameters [Rei13]:

$$\phi_s = \frac{2\pi}{\lambda_e}\frac{eU}{E}\frac{E_r + E}{2E_r + E}t_f, \tag{7.24}$$

where eU is the potential energy along a row of atoms, $E_r = m_0c^2$ is the rest energy of the electron, and t_f is the thickness of the thin film. The potentials for carbon and gold atoms are $U = 8\,\mathrm{V}$ and $U = 21\,\mathrm{V}$, respectively. An electron ($E = 30\,\mathrm{keV}$) that passes through a carbon thin film of $t_f = 10\,\mathrm{nm}$, which is coated with $t_f = 2\,\mathrm{nm}$ of gold, acquires an average phase shift of $\phi_s \sim 1.9\,\mathrm{radians}$. At the sample plane, the electron wave function (Eq. 7.9) is multiplied by the transmission function of the sample (T_s) and the modulus squared of the Fourier transform function yields the electron Ronchigram intensity (I_R) at the screen:

$$I_R = \sum_{i=1}^{n} |FFT[\psi_p(\boldsymbol{w}, E_i)T_s]|^2, \tag{7.25}$$

where E_i takes linearly spaced values between $[E - \Delta E, E + \Delta E]$ and the electron wavelength and the defocus (see Eq. 7.5) are energy dependent. The function T_s represents the maximum phase shift induced to the electron wave by the sample [SSH19]:

$$T_s = e^{-i\phi_s \Upsilon(\boldsymbol{w})}. \tag{7.26}$$

The parameter $\Upsilon(x_2, y_2)$ simulates the random phase induced by the amorphous carbon and is defined as:

$$\Upsilon(\boldsymbol{w}) = rand(N_x, N_y). \tag{7.27}$$

The real space units at the Ronchigram plane in Fig 7.3 are defined as:

$$x = \lambda_e f_2 \frac{1}{\Delta x} \frac{1}{N_x} [-\frac{N_x}{2} ... \frac{N_x}{2}], \tag{7.28}$$

$$y = \lambda_e f_2 \frac{1}{\Delta y} \frac{1}{N_y} [-\frac{N_y}{2} ... \frac{N_y}{2}], \tag{7.29}$$

where N_x and N_y are the total number of pixels in the matrix, $\Delta x = \Delta y$ is the spatial resolution in the sample plane.

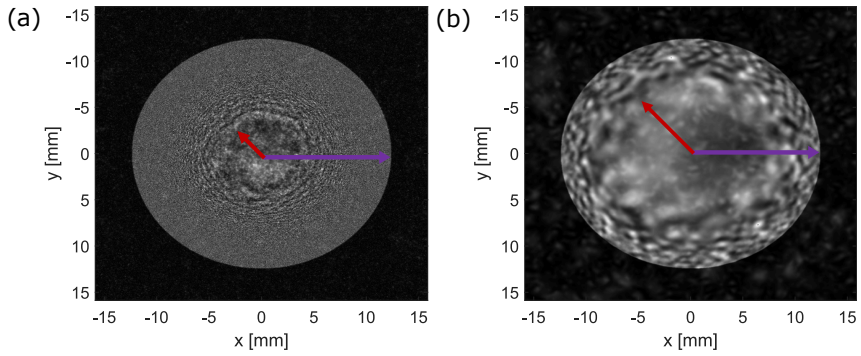


Figure 7.3: Ronchigram simulations. In-focus Ronchigram simulation from an amorphous thin film imprinting a random phase to the electron probe. The interference pattern is recorded on the screen. The purple arrow indicates the maximum convergence semi-angle (20 mrad), whereas the red arrow estimates the aberration-free semi-angle (5.5 (a) and 11.8 (b) mrad).

The following parameters were used for simulating the electron Ronchigram in 7.3: 30 keV electron beam energy, 200 μm objective lens aperture, a focal length of the objective lens $f_1 = 5$ mm, 20 mrad maximum convergence semi-angle, the free propagation distance

from the sample to the screen $f_2 = d1 + d2 = 62\,\text{cm}$, the defocus value is set to $C_{1,0} = C_c\frac{\Delta E}{E}$ with $C_c = 1\,\text{mm}$, $\Delta E = 1\,\text{eV}$ and the third order spherical aberration coefficient $C_{3,0} = 10\,\text{mm}$ for Fig. 7.3(a) and $C_{3,0} = 0.5\,\text{mm}$ for Fig. 7.3(b). When reducing the spherical aberration coefficient from 10 mm to 0.5 mm, it can be seen how the aberration-free semi-angle increases from $\sim 5.5\,\text{mrad}$ (see Fig 7.3(a), red arrow) to $\sim 11.8\,\text{mrad}$ (see Fig 7.3(b), red arrow). The finite coherence of the electron beam is not taken into account, which might affect the contrast in the Ronchigram. Nevertheless, the Ronchigram simulation shows that an effective C_s correction should lead to an increase of the sweet spot at the detector plane. Thus, the Ronchigram might be used for future proof-of-principle light-based electron wavefront shaping experiments.

7.1.2 Experimental Ronchigram measurement in continuous mode

The following parameters have been selected to measure an electron Ronchigram: the aperture of the objective lens was set to $200\,\mu\text{m}$, the electron beam energy to 30 keV, the working distance of the objective lens 4 mm, and an amorphous carbon sample ($t_f =\sim 10\,\text{nm}$) is used.

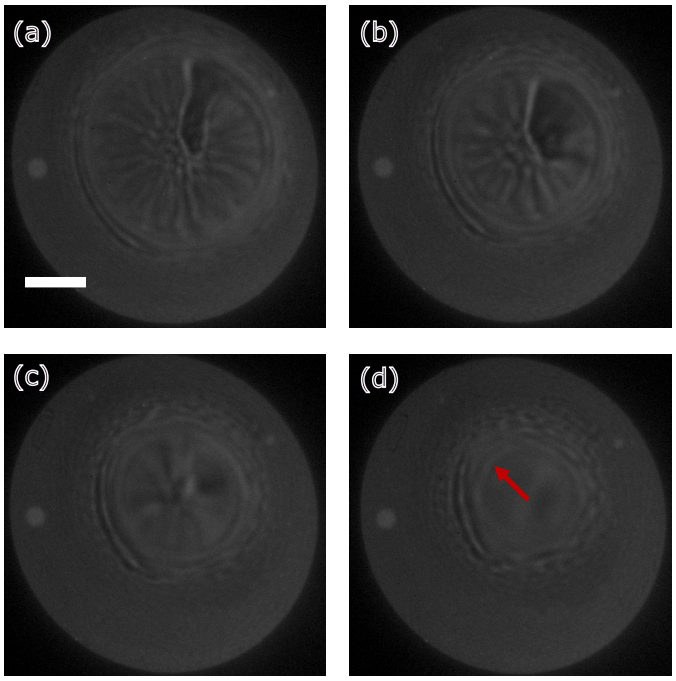


Figure 7.4: Experimentally recorded electron Ronchigrams in continuous mode, revealing spherical aberrations in the form of rings. (a)-(c) Ronchigram images recorded with the electron beam slightly defocused from the sample. (d) Ronchigram in focus, the aberration-free semi-angle is 6.1 mrad, whereas the maximum convergence semi-angle is 20 mrad (scalebar 5 mm).

We noticed that the contrast in the Ronchigram decreases when going to lower electron energies (<30 keV), most likely because of charging, increased inelastic scattering effects. After interaction with the sample, the electrons propagate in free space for $f_2 = 62$ cm and are detected with the MCP assembly. Note that the contrast in the electron Ronchigram image can be severely degraded by mechanical vibrations of the microscope or sample holder and stray electromagnetic fields [JB99].

Figure 7.4 shows a series of electron Ronchigrams recorded at the detector plane. The rings around the complex interference pattern arise from the spherical aberrations [Cow79]. Figure 7.4 shows a Ronchigram at zero defocus that shows the 'sweet spot'. By measuring the radius (r_{free}) of the region of uniform intensity (see Fig. 7.4(d)), one can determine the aberration-free semi-angle ($\alpha_{\text{free}} = r_{\text{free}}/f_2 = 6.1$ mrad). The maximum convergence semi-angle is $\alpha_{max} = \rho_s/f_2 = 20$ mrad. The radius (ρ_s) of the electron beam at the screen has been determined by fitting the electron distribution with an ellipse [Gal].

7.1.3 Experimental Ronchigram measurement in pulsed mode

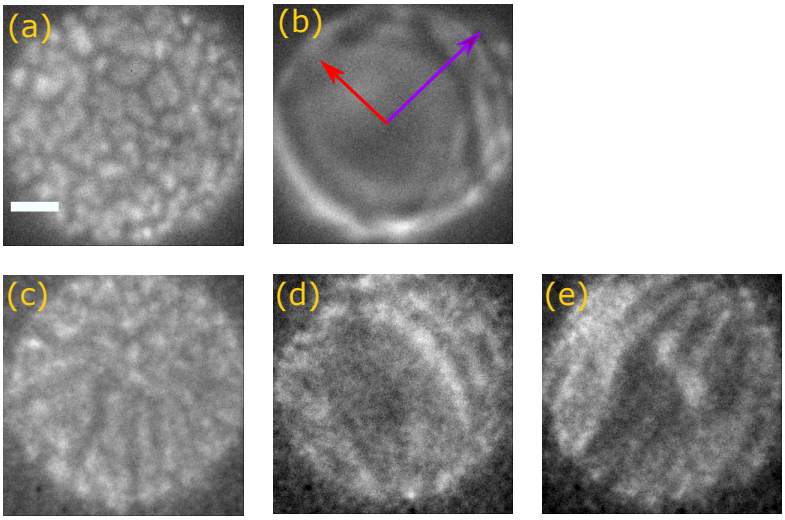


Figure 7.5: Experimentally measured Ronchigrams at 30 keV electron energy from gold-coated amorphous carbon sample. Shadow image (scalebar 1.1 mm) in continuous mode with the electron beam defocused (a) and focused (b) on the sample revealing the sweet spot in the electron Ronchigram. (b) The aberration-free semi-angle is $\sim$ 3.3 mrad (red arrow), whereas the maximum convergence semi-angle is $\sim$ 4.8 mrad (purple arrow). (c), (d) Same as (a) and (b) but now in pulsed mode. (e) Stigmating slightly the electron probe used in (d) to see a significant change in the Ronchigram is typical when infinite magnification is reached.

It has been shown in [EHE+15] that the spatial coherence is for the most part preserved when going from dc-emission to laser-triggered tungsten nano-tips. This motivated us to try and record a pulsed electron Ronchigram. To optimize further the contrast of the Ronchigram and reduce possible charging effects, we now coated an amorphous carbon sample ($t_f = 5\,\mathrm{nm}$) with a thin ($\sim 2\,\mathrm{nm}$) film of gold. Furthermore, the aperture of the objective lens is set to $100\,\mu\mathrm{m}$ (from OA = $200\,\mu\mathrm{m}$ used in the previous sub-chapter) to increase the coherence of the electron beam. Note that thicker ($>10\,\mathrm{nm}$) amorphous carbon samples coated with 2 nm gold showed less contrast, most likely because of the decoherence induced by inelastic and multiple elastic scattering effects. Lastly, the working distance has been increased from 4 to 23 mm to reduce the beam size at the screen and subsequently enhance the electron signal.

From a practical point of view, the best way of recording a Ronchigram in pulsed-mode is to optimize first the contrast of the Ronchigram in continuous mode. Afterward, at the same electron beam settings, the electrons can be triggered with the laser pulse, and a Ronchigram in pulsed mode should be visible within a reasonable defocus range. Figures 7.5(a) shows the shadow image of the sample recorded with the continuous mode electron beam defocused. The granularity (several nanometers) of the gold coating is visible. Furthermore, the sweet spot of the electron Ronchigram is shown in Fig. 7.5(b). Figure 7.5(c) shows the shadow image of the sample with the pulsed electrons defocused. Figure 7.5(d) reveals the sweet spot of the pulsed electron Ronchigram. Further, the electron probe from Fig. 7.5 is stigmated, and the new Ronchigram is recorded in Fig. 7.5(e). The induced astigmatism causes a significant change in the Ronchigram, which confirms that infinite magnification is reached.

At low electron currents, at ~ 0.1 electrons per pulse at the sample plane, space charge effects are avoided, decoherence minimized, but this leads to long acquisition times ($>5\,\mathrm{s}$), which degrade the contrast in the image due to instabilities and other noise sources. Nevertheless, to my knowledge, this is the first Ronchigram recorded in pulsed mode from an amorphous carbon sample. The results shown here confirm that coherent wavefront-shaping experiments are possible with pulsed electron beams in SEMs.

However, to show aberration correction with our light-based method, a Ronchigram should be recorded by placing the amorphous carbon sample under the IP. Also, Ronchigrams are recorded at high convergence angles; sometimes, even the aperture at the OL is removed. Since our laser-based electron modulator is placed after the SEM objective lens, the sample to be investigated would have to be placed at unpractical working distances of $\sim 70\,\mathrm{mm}$. At such long working distances, an electron Ronchigram does not reveal itself. For this reason, we installed an electrostatic lens (electron energies up to 6 keV) after the IP such that we could eventually be able to have optimal conditions (high convergence angles) for recording the Ronchigram. So far, we could not measure any electron Ronchigram in pulsed mode with the triggered electrons at 6 keV, not even when placing the amorphous carbon sample directly under the magnetostatic objective lens.

Further studies are required to measure an electron Ronchigram in pulsed mode at $E < 30\,\mathrm{keV}$. This could include: an increase in the electron current by using a higher repetition rate of the UV laser, focusing the UV to a smaller beam waist at the tip (to minimize the electron emission area), optimizing the thickness of the amorphous carbon sample, recording an edge Ronchigram from a silicon crystal, and reducing further the noise sources that might degrade the contrast and optimizing the electron beam settings for maximum transverse coherence (similar to [FBdS+17]).

7.2 Light-based electron optics for spherical aberration correction of electron beams

As discussed in previous sub-chapters, the spherical aberrations of electrons limit the achievable electron probe size. In principle, the corrective light-based phase mask should satisfy the relation $\varphi_{Laser} = -\chi$, where φ_{Laser} is proportional to the spatial energy distribution of the light in the aperture plane of the electron microscope's OL.

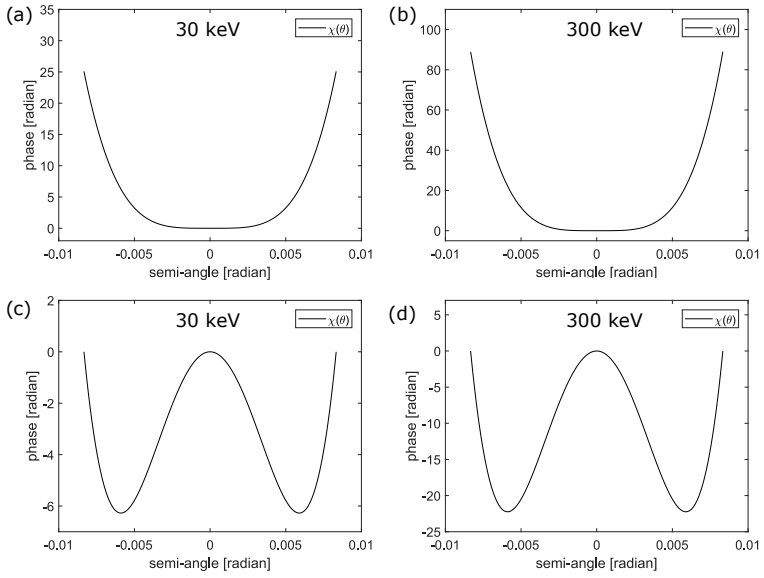


Figure 7.6: The electron phase distortion due to spherical aberration at the objective lens of a (S)TEM without and with Scherzer defocus. The phase values are plotted against the convergence semi-angle θ. (a) Acquired phase distortion of a 30 keV beam with defocus $D_z = 0$. (b) Acquired phase distortion of a 300 keV beam with defocus $D_z = 0$. (c),(d) are the acquired phase distortion at Scherzer defocus (see Eq.7.7) of 30 keV and 300 keV, respectively. When using the Scherzer defocus, the absolute value of the phase distortion is minimized by almost 4x.

The phase distortion of the electron wave due to the lens aberration is investigated for typical electron energy used in SEM and TEM (see Fig. 7.6). The simulations are carried out for electron energy of 30 keV (see Fig. 7.6 (a),(c)) and for 300 keV (see Fig. 7.6 (b),(d) without (top), and with (bottom) Scherzer defocus. Figure 7.6 shows the distortion of the electron phase as a function of convergence semi-angle (see Eq. 7.6). Apart from the electron energy and Scherzer defocus, all other parameters of the aberrations function are kept the same, as follows: $C_s = 5.78\,\text{mm}$, $\alpha_{max} = 8.3\,\text{mrad}$, $f = 3\,\text{mm}$ and $OA = 50\,\mu\text{m}$. For convenience reasons, the parameters have been chosen such that the average phase distortion over the OA is $|\bar{\phi}| \sim \pi$ when using the Scherzer defocus and 30 keV electrons. The data in Fig. 7.6 shows that by applying the Scherzer defocus on top of the spherical aberration, the phase distortion is reduced by almost 4x.

In this chapter, methods of creating a laser intensity distribution that has the same shape as the spherical aberrations pattern simulated in Fig. 7.6, are discussed. Typical electron wavefront-shaping techniques set an upper limit of $\rho_s \sim 25\,\mu\text{m}$ on the area that can be shaped. The question is what wavefront shaping technique should be used to create the required light distribution for correcting the electron beam aberrations over such an area. For a high NA light optical system with sufficient individually controlled pixels, the modified GSA described in sub-chapter 4.3.2 would provide good results. However, it is challenging to build a high NA optical system inside a microscope. Furthermore, a high NA might introduce further constraints on the pulse length of electrons and light.

The modified GSA is not the optimal wavefront shaping technique for aberration correction of electron focal spots when having a low optical NA. In our setup, the resolution of the laser focal spot is $4.3\,\mu\text{m}$ (FWHM), which allows us to control individually only $\sim 10 \times 10$ pixels over $\rho_s \sim 25\,\mu\text{m}$. Thus, we propose two different light wavefront shaping techniques for aberration correction of electron lenses that do not suffer from the limited number of pixels and can be used with low NA systems. They are based on shaping the source Gaussian beam with vortex phases and Zernike polynomials to have the required spatial distribution.

Laguerre Gauss modes to correct for the spherical aberrations of electron beams

It has been theoretically shown in [UKS22] that a LG10 light-based electron lens induces negative spherical aberration coefficients, which in combination with traditional electron lenses that have positive coefficients, could form an aberration-free lens system. However, the correction with LG10 is based on strong electron deflection and requires high laser pulse energy. Furthermore, it is shown in [Sch22a] that the intensity distribution of a LG20 beam has a r^4 dependence close to the optical axis. Placing the electron beam under the r^4 region of the LG20 beam should induce the negative phase shift $\varphi_{\text{Laser}}(r) = -\chi(r)$ required to correct the spherical aberrations.

Moreover, it has been theoretically shown recently [dAK21] that a LG30 could be used to correct for the spherical aberrations. Their model uses co-propagating electron

and laser pulses and calculates the induced phase shift by integrating the vector potential over the whole propagation distance. In our model, the ponderomotive interaction occurs only in the laser beam's focal plane. The LG30 has a r^6 distribution near the optical axis and, therefore, cannot be implemented using our model.

Note that all low-charge LG modes are highly susceptible to both odd and even aberrations [BN06, DMG15]. Thus, it is challenging to experimentally generate aberration-free low charge LG modes in the IP, mainly because we have a 1.5 mm beam block (aperture in the mirror) along the optical path. Nevertheless, more research is required to establish the most efficient method of electron aberration correction with LG modes.

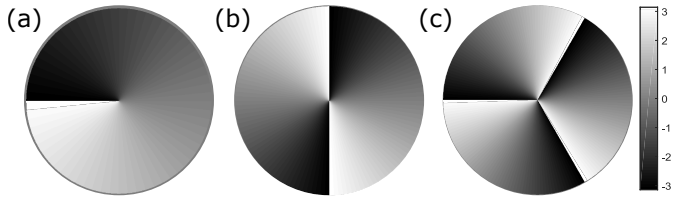


Figure 7.7: The LG modes can be easily generated by placing the appropriate phase mask along the Gaussian laser beam path. (a) The phase mask ϕ_{V10} used to generate an LG10 mode. (b) The phase mask ϕ_{V20} used to generate an LG20 mode. (c) The phase mask ϕ_{V30} used to generate an LG30 mode. The dimension of the phase masks shown here should be equal to the expanded source intensity distribution.

Figure 7.7 shows the phase mask (ϕ_{Vl0}) that can be displayed on the SLM to generate the LGlp modes, where l is the charge of the specific mode and $p = 0$. The vortex phase plates can be mathematically created as follows: $\phi_{\mathrm{Vl0}} = l \times \mathrm{atan2}(Y, X)$ and could be superimposed to the phase mask calculated for the backpropagation of the Gaussian and further correction (see chapter 4).

Shaping the laser beam with Zernike polynomials to correct the spherical aberrations

In the following, we shape the Gaussian beam with Zernike polynomials to achieve a laser distribution for spherical aberration correction. This method might be less susceptible to aberrations and more energy efficient than shaping the Gaussian into low-charge LG modes.

Furthermore, we have seen from Fig. 7.6 that applying a Scherzer defocus to the spherical aberration function reduces the amount of phase shift required to flatten the phase. A phase mask having a distribution described by Eq. 7.6 has been successfully applied in a TEM [SRL$^+$18] to experimentally correct for the spherical aberrations of the electron probe forming lenses. The diffractive phase mask is based on Silicon Nitride thin films [SRL$^+$18]. Here, our goals is to reproduce the analytical pattern of a spherical aberration function with Scherzer defocus (Eq. 7.6) by shaping the laser beam with radially symmetric Zernike polynomials. The aberrated phase should be flattened at the

lens by setting $\varphi_{\text{Laser}}(r) = -\chi_{\text{Scherzer}}(r)$.

Figure 7.8(a) shows the intensity distribution measured with the CMOS in the CP after shaping the expanded Gaussian beam with a diffractive phase mask displayed on the SLM $\phi_{\text{Scherzer}} = \text{modulo}2\pi[\phi_G + \phi_{\text{sp}}]$ (b), whereas $\phi_{\text{sp}} = (0.5 \times \pi \times Z_4^0 - 0.86 \times \pi \times Z_6^0)$. The coefficients of the Zernike phase patterns have been optimized by trial and error until the measured intensity distribution is similar to the aberrated electron phase distribution. Figure 7.8(c) is the extracted region of interest from Fig. 7.8(a). Figure 7.8(d) shows the target intensity distribution that has to be reproduced to correct the aberrations. Figure 7.8(e) shows the normalized intensity data along a line in Fig. 7.8 and the analytical aberration function. The diffraction efficiency in the region of interest is $I_{\text{eff}} = I_{\text{ROI}}/I = \sim 58\%$.

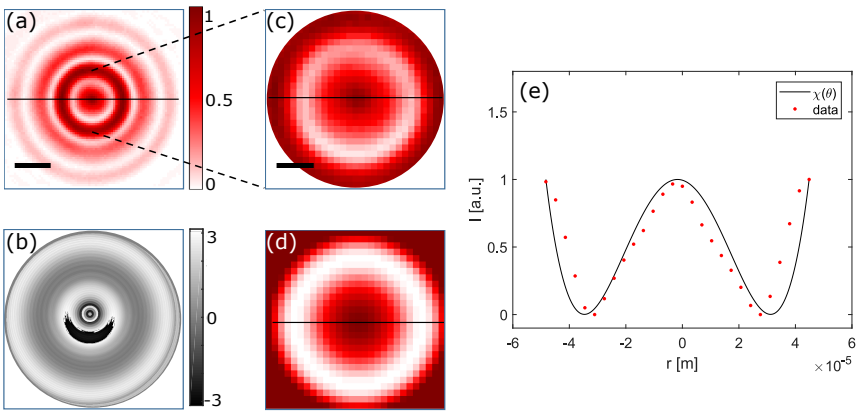


Figure 7.8: Laser phase plate pattern including Scherzer defocus to correct for the spherical aberrations of the electron beam. (a) (scalebar 55 μm) The experimentally measured intensity distribution formed in the CP when diffracting the Gaussian off the phase mask shown in (b). (b) The phase mask displayed on the SLM contains the off-centered Gaussian ϕ_G phase masks calculated with a simple backpropagation from 4.2 superimposed with the Zernike phase mask. (c) This image represents the extracted region of interest (scalebar 21 μm) from (a). (d) The analytical intensity distribution of a spherical aberration function with Scherzer defocus. (e) Data plotted from the line in (c) and the analytical distribution from the line in (d).

Shaping the Gaussian beam with Zernike polynomials might improve the efficiency of the laser phase plate compared to other methods; however, more research is required to optimize the Zernike coefficients. It can be seen in Fig. 7.8(e) that the analytical function does not perfectly go through the data points. The exact deviation from the analytical function has yet to be quantified since it is the subject of future research. Nevertheless, these preliminary measurements show that the required laser-phase plate for aberration correction could be generated by applying the right combination of Zernike polynomials.

8 Discussion

In this thesis, it is experimentally demonstrated that the spatially induced ponderomotive phase shift can scatter the electrons into almost arbitrary transverse profiles. The created electron beam shapes are limited by light diffraction and artifacts caused by the 1.5 mm hole in the mirror that brings the laser onto an axis collinear with the electrons. The artifacts could be minimized in future setups by reducing the diameter of the hole or by increasing the laser beam size at the mirror. Better resolution in the electron phase modulation could be achieved either by increasing the numerical aperture of the optical setup or by using a laser with a shorter wavelength. However, the relatively small numerical aperture (NA) ensures that the Rayleigh range of the laser beam is longer than the spatial dispersion of the electron wave packet and the distance the electrons travel during the interaction. Thus, a high optical NA might affect the pulse length requirements of electrons and light because now we consider that the interaction takes place within the focal spot of the laser.

Ponderomotive phase modulation of electrons requires high laser intensities. In continuous-wave mode, the required intensities for $\pi/2$ phase shifts of a single pixel have been achieved only by using enhancement cavities [SAC+19]. In contrast, arbitrary shaping in free space is realistically compatible only with pulsed systems. One way to avoid using an enhancement cavity would be to increase the interaction time between the electrons and light, use a longer laser wavelength, and place the modulator in a low electron energy region. However, increasing the interaction time is only an option for low-NA optical fields with long focus range. To be noted that in our derivation with co- or counter propagating pulses, the phase shift scales with λ_L^2, but so does the minimal focal spot size. Therefore, a longer λ_L will increase the induced electron phase shift only for applications where the laser beam waist has to be constrained to a specific value. A realistic setup could include a long wavelength nondiffracting Bessel beam co-propagating with the electron beam over a long enough distance.

The experiments have been carried out in a high-power regime to induce high scattering phase shifts (up to 950 radians) to the electrons, eventually creating a measurable transverse intensity change at the detector plane. However, wavefront shaping techniques require less laser pulse energy, depending on the diameter of the electron beam that needs to be modulated. To shift the phase of an electron at 30 keV by 2π over an area of $1\,\mu\text{m}^2$, a pulse energy of 0.58 nJ is needed. Furthermore, the transverse coherence of the electron beam limits the area that can be shaped. This study [VBMC+18] mentions that a disk with $\rho_s \sim 25\,\mu$m can be illuminated with sufficient coherence. Surprisingly, it has been recently shown [RSL+21a] that a thin film phase plate has been used to correct

the spherical aberrations of a probe forming electron lens over a disc with a diameter of $150\,\mu$m. The maximum pulse energy reaching our setup's interaction region is $17.2\,\mu$J. This enables shaping the phase of electrons over a disc with a radius of $R \leq 97\,\mu$m with having $\sim (2 \times R/FWHM)^2 = 1607$ programmable pixels.

Most importantly, the interaction of electrons with light is lossless and does not introduce inelastic scattering or sub-aperture diffraction. This is in contrast to state-of-the-art competing technologies [VBMC$^+$18, SRL$^+$18]. Lossless wavefront shaping is particularly important for ultrafast electron microscopes, where a low electron signal (usually single electron per pulse at the source) requires a long acquisition time and ultimately limits the spatial resolution.

An appealing application would be light-based aberrations correction of magnetic or electrostatic electron lenses. During the last century, many attempts [Ros09] have been made to correct the spherical aberrations that could eventually lead to sub-A resolution. The first effective correction has been realized by [HRU$^+$98], which revolutionized material science [Cou18] and enabled atomic [ERKD09] resolution. Aberration correctors based on multipole lenses are now implemented successfully in many research laboratories [CEOa]. However, they are expensive, static, and can occupy a significant volume [CEOb], increasing the electron path length. This can corrupt the electron beam by making it more susceptible to noise [UMH$^+$13, LHU$^+$16] and pulse-broadening effects in the case of a pulsed electron beam. Nevertheless, more research is required to establish whether the light-based method's noise levels can outperform the noise in traditional multipole correctors.

It has been theoretically [KcvdA20, dAK21] demonstrated that an effective spherical aberration correction is possible without the need for complex multipole lenses. The experimental demonstration still needs to be included. For ponderomotive phase shifts of electron wavefronts by π at 30 keV in a TEM over a disc with $\rho_0 = 25\,\mu$m , a pulse energy of $\sim 0.57\,\mu$J is required. Unfortunately, we could not yet show aberration correction of the SEM objective lens in our setup. A standard way to see and measure the aberrations in an electron beam is to measure electron Ronchigrams as described in chapter 7. Pulsed Ronchigrams have been recorded at 30 keV with the sample directly after the OL; however, not after the IP. We attributed this to vibrations, and stray fields, which become more prominent with increased work distance and degrade the contrast when longer acquisition times are required.

Two possible methods have been identified for creating the required laser distribution that could correct the spherical aberrations. First, a GSA could be used to control individual pixels in the laser phase plate pattern; however, in this case, the resolution of the reconstructed pattern is limited by the FWHM of the laser. Second, the laser beam can be shaped with vortex phase plates or Zernike polynomials to induce the required $\varphi_{\text{Laser}} = -\chi$ corrective phase shift. The spatial intensity transition between values is

free of speckles, demonstrating the advantage of not having to use an iterative algorithm for phase mask design. Preliminary results suggest that shaping the laser beam with Zernike polynomials is an efficient way of generating a corrective laser-based phase mask for electrons; however, the Zernike coefficients need more optimization.

The pulse energy stability of our laser is $\sim 1.5\%$ r.m.s and is of no concern for our experiments. The beam-pointing stability of our laser is $6\,\mu$rad/K right after the beam stabilization system. However, in our setup, the laser beam propagates for $\sim 1\,$m after passing through the stabilization system. It should be noted that the stabilization system cannot compensate for vibrations that are induced after the sensor. Therefore, the system should be ideally installed in a future setup as close as possible to the interaction plane.

Furthermore, there are also thermal drifts induced by the mirror with the hole, which makes the collinear interaction with the electrons possible. These thermal instabilities are especially of concern when increasing pulse energy in the shaped beam above $\sim 2\,\mu$J. The instability is visible in the raw data of convex laser-based lens in Fig. 6.9. Nevertheless, thermal effects from the mirror could be minimized in future setups by reducing the hole size, increasing the beam size at the mirror surface, better coating, and using a mirror substrate with low thermal expansion [TAC$^+$21].

Concave lensing is currently impossible with static cylindrically symmetric and energy-preserving electro- and magnetostatic lenses. Both convex and concave ponderomotive lensing with focal lengths comparable with traditional electron optics has been demonstrated, whereas the concave lens could find applications in spectroscopy. Also, combining convex and concave lenses could de- or magnify an electron beam over smaller distances. Furthermore, a light-based lensing system could be implemented in ultrafast Lorenz microscopes [dSMF$^+$18], where the objective lens is usually turned off to avoid corrupting the magnetic properties of the sample to be investigated; the current resolution is rarely better than 100 nm. Most importantly, the size of the current microscopes could be dramatically reduced if an electron microscope contained an aberration corrector made out of light. A current limitation in obtaining competing high resolution with our ponderomotive lens is the small NA of the light-based electron lens (0.5 mrad). Nevertheless, the NA could be significantly increased by by carefully adjusting the parameters in Eq. 6.2.2.

Most importantly, a significant advantage of our wavefront shaping scheme compared to the current aberration correction scheme is that we can shape the wavefront arbitrarily. The adaptive method could be used for the generation of laser phase plates to enhance the sensitivity of weakly scattering specimens in electron phase microscopy [SAC$^+$19]. Furthermore, it could also be used for probe engineering [HPA$^+$14, OCP$^+$16] to adjust the electron beam to a specific area on the sample while maximizing the information extracted and limiting the electron dose. Also, it can be used for the generation of exotic beams [GKG$^+$14, VBLL$^+$13]. We note that our wavefront-shaping method is lossless, and does not introduce inelastic scattering.

In most experiments that show ponderomotive scattering, the laser beam propagates orthogonally to the electron beam [SAC+19, ACS+20], or under an angle [KSH18]. In those cases, the laser beam's polarization can play a role [ACS+20]. In our setup, the laser and electron beam propagate on the same axis, so any linear polarization of the laser beam is orthogonal to the electron beam and, therefore, induces the same phase shift. A laser beam polarized in the z-direction would cause a suppressed phase shift by $1/\gamma^2$. However, since we use a low NA (< 0.2), the relative intensity contribution of the z-polarized electric field component (at the highest spatial frequency) is $E_z^2/E_r^2 < 0.04$. Therefore we assume the paraxial approximation for both electron and light beam and neglect the z-component. Nevertheless, it would have been interesting to report a negative result on polarization dependence. This might include placing a rotating half-wave plate on the laser beam path and measuring whether it affects the interaction with the electrons.

Sculpting electron beams with light opened up a new research direction. In the future, parts of electron microscopes might be made out of optical systems to improve the resolution and contrast of electron images.

9 Conclusion and Outlook

While most experiments with ultrafast electrons in free space have shaped the longitudinal [RK20] wave function component, this thesis describes a setup built from scratch to show programmable transverse electron beam modulation with light. The interaction takes place in free space without being assisted by any material. Thus, the interaction is lossless and does not cause inelastic scattering. The light fields are shaped by diffracting the light at programmable phase masks which the SLM displays. The arbitrary laser pattern applied to the electron beam can be switched fast, limited by the frame rate of the SLM (frame rates up to 1430 Hz). A Gerschberg-Saxton algorithm has been modified to calculate the required phase masks, considering the hole in the probe forming mirror. Furthermore, the diffraction effects in the laser pattern can be suppressed if the hole in the mirror is reduced to $< 1\,\mathrm{mm}$. For speckle suppression, the GSA is initiated with an object-dependent quadratic phase, and the amplitude in the Fourier plane is constrained in the signal region during the iterative process.

The spatial and temporal overlap between the electron and laser pules is established in a novel way without using an energy filter. First, a fast-timing scintillator with a single photon detector is used to timestamp the pulses. Afterward, pump-probe measurements with a copper grid reduce the timing mismatch to 1 ps uncertainty. With the pulses synchronized at the IP, different laser-based phase masks are imparted to the electron beam and generate almost arbitrary electron distributions. Also, both convex and concave lensing is demonstrated, the latter being impossible to achieve with electro- and magnetostatic, energy-preserving lenses.

Finally, chapter 7 discusses the dependence of various parameters on the electron probe size. One future application of our light-based electron wavefront shaping technique is aberrations correction. For this reason, electron Ronchigrams have been simulated and experimentally measured in continuous and pulsed mode to quantify the spherical aberrations and show coherent wavefront shaping. Unfortunately, we saw pulsed electron Ronchigrams only with the sample placed before the IP. Further work is needed to combine the ponderomotive experiments with pulsed electron Ronchigrams to show coherent manipulation of electron-waves.

Bibliography

[ACS+20] Jeremy J Axelrod, Sara L Campbell, Osip Schwartz, Carter Turnbaugh, Robert M Glaeser, and Holger Müller. Observation of the relativistic reversal of the ponderomotive potential. *Physical review letters*, 124(17):174801, 2020.

[AFG+14] Fabio Acerbi, Alessandro Ferri, Alberto Gola, Massimo Cazzanelli, Lorenzo Pavesi, Nicola Zorzi, and Claudio Piemonte. Characterization of single-photon time resolution: from single spad to silicon photomultiplier. *IEEE Transactions on Nuclear Science*, 61(5):2678–2686, 2014.

[ASEA+95] M Aeschlimann, CA Schmuttenmaer, HE Elsayed-Ali, RJD Miller, J Cao, Y Gao, and DA Mantell. Observation of surface enhanced multiphoton photoemission from metal surfaces in the short pulse limit. *The Journal of chemical physics*, 102(21):8606–8613, 1995.

[Bar67] Lawrence S Bartell. Reflection of electrons by standing light waves: a simple theoretical treatment. *Journal of Applied Physics*, 38(4):1561–1566, 1967.

[BBd+95] S Baccaro, K Blaŝek, F de Notaristefani, P Maly, J.A Mares, R Pani, R Pellegrini, and A Soluri. Scintillation properties of yap:ce. *Nuclear Instruments and Methods in Physics Research Section A: Accelerators, Spectrometers, Detectors and Associated Equipment*, 361(1):209–215, 1995.

[BCE89] Peter Buseck, John Cowley, and LeRoy Eyring. *High-resolution transmission electron microscopy: and associated techniques*. Oxford University Press, 1989.

[BFZ09] Brett Barwick, David J Flannigan, and Ahmed H Zewail. Photon-induced near-field electron microscopy. *Nature*, 462(7275):902–906, 2009.

[BGM+14] SE Brunner, Lukas Gruber, Johann Marton, Herbert Orth, and K Suzuki. Time resolution below 100 ps for the scitil detector of panda employing sipm. *Journal of Instrumentation*, 9(03):C03010, 2014.

[Bir13] John Betteley Birks. *The theory and practice of scintillation counting: International series of monographs in electronics and instrumentation*, volume 27. Elsevier, 2013.

[BMM+18] G Berruto, I Madan, Y Murooka, Giovanni M Vanacore, E Pomarico, J Rajeswari, R Lamb, P Huang, AJ Kruchkov, Y Togawa, et al. Laser-induced skyrmion writing and erasing in an ultrafast cryo-lorentz transmission electron microscope. *Physical review letters*, 120(11):117201, 2018.

[BN06] Bosanta R Boruah and MAA Neil. Susceptibility to and correction of azimuthal aberrations in singular light beams. *Optics express*, 14(22):10377–10385, 2006.

[BPC+16] K Bücker, M Picher, O Crégut, T LaGrange, BW Reed, ST Park, DJ Masiel, and F Banhart. Electron beam dynamics in an ultrafast transmission electron microscope with wehnelt electrode. *Ultramicroscopy*, 171:8–18, 2016.

[BRB+93] Philip R Bevington, D Keith Robinson, J Morris Blair, A John Mallinckrodt, and Susan McKay. Data reduction and error analysis for the physical sciences. *Computers in Physics*, 7(4):415–416, 1993.

[BRK12] David C Bell, Christopher J Russo, and Dmitry V Kolmykov. 40 kev atomic resolution tem. *Ultramicroscopy*, 114:31–37, 2012.

[BRT68] LS Bartell, RR Roskos, and H Bradford Thompson. Reflection of electrons by standing light waves: experimental study. *Physical Review*, 166(5):1494, 1968.

[BSB88] P. H. Bucksbaum, D. W. Schumacher, and M. Bashkansky. High-intensity kapitza-dirac effect. *Physical Review Letters*, 61(10):1182–1185, 1988.

[BVBVTV14] Armand Béché, Ruben Van Boxem, Gustaaf Van Tendeloo, and Jo Verbeeck. Magnetic monopole field exposed by electrons. *Nature Physics*, 10(1):26–29, 2014.

[BW13] Max Born and Emil Wolf. *Principles of optics: electromagnetic theory of propagation, interference and diffraction of light*. Elsevier, 2013.

[BYZ07] Peter Baum, Ding-Shyue Yang, and Ahmed H Zewail. 4d visualization of transitional structures in phase transformations by electron diffraction. *science*, 318(5851):788–792, 2007.

[CDGG+14] Paolo W Cattaneo, Matteo De Gerone, Flavio Gatti, Miki Nishimura, Wataru Ootani, Massimo Rossella, and Yusuke Uchiyama. Development of high precision timing counter based on plastic scintillator with sipm readout. *IEEE Transactions on Nuclear Science*, 61(5):2657–2666, 2014.

[CEOa] Aberration correctors. `https://www.ceos-gmbh.de/de/literatur`. Accessed: 2022-08-16.

[CEOb] Volume of correctors. `https://www.ceos-gmbh.de/de/produkte/temkorrektoren/salve`. Accessed: 2022-08-16.

[CMWS+22] Marius Constantin Chirita Mihaila, Philipp Weber, Matthias Schneller, Lucas Grandits, Stefan Nimmrichter, and Thomas Juffmann. Transverse electron-beam shaping with light. *Phys. Rev. X*, 12:031043, Sep 2022.

[Cou18] Rachel Courtland. The microscope revolution that's sweeping through materials science, nov 2018.

[Cow79] JM Cowley. Adjustment of a stem instrument by use of shadow images. *Ultramicroscopy*, 4(4):413–418, 1979.

[CPH+22] Usama Choudhry, Fengjiao Pan, Xing He, Basamat Shaheen, Taeyong Kim, Ryan Gnabasik, Geethal Amila Gamage, Haoran Sun, Alex Ackerman, Ding-Shyue Yang, et al. Persistent hot carrier diffusion in boron arsenide single crystals imaged by ultrafast electron microscopy. *Matter*, 2022.

[CRC+03] Narupon Chattrapiban, Elizabeth A Rogers, David Cofield, Wendell T Hill III, and Rajarshi Roy. Generation of nondiffracting bessel beams by use of a spatial light modulator. *Optics letters*, 28(22):2183–2185, 2003.

[CT79] YW Chan and WL Tsui. Classical theory of scattering of an electron beam by a laser standing wave. *Physical Review A*, 20(1):294, 1979.

[dAK21] F Javier García de Abajo and Andrea Konečná. Optical modulation of electron beams in free space. *Physical Review Letters*, 126(12):123901, 2021.

[DFI15] Sergei Dolinsky, Geng Fu, and Adrian Ivan. Timing resolution performance comparison of different sipm devices. *Nuclear Instruments and Methods in Physics Research Section A: Accelerators, Spectrometers, Detectors and Associated Equipment*, 801:11–20, 2015.

[DHE+06] Jason R Dwyer, Christoph T Hebeisen, Ralph Ernstorfer, Maher Harb, Vatche B Deyirmenjian, Robert E Jordan, and RJ Dwayne Miller. Femtosecond electron diffraction:'making the molecular movie'. *Philosophical Transactions of the Royal Society A: Mathematical, Physical and Engineering Sciences*, 364(1840):741–778, 2006.

[DHN+06] A Dolocan, M Hengsberger, HJ Neff, M Barry, C Cirelli, T Greber, and J Osterwalder. Electron–photon pulse correlator based on space-charge effects in a metal pinhole. *Japanese journal of applied physics*, 45(1R):285, 2006.

[DJH+07] Jason R Dwyer, Robert E Jordan, Christoph T Hebeisen, Maher Harb, Ralph Ernstorfer, Thibault Dartigalongue, and RJ Dwayne Miller. Experimental basics for femtosecond electron diffraction studies. *Journal of Modern Optics*, 54(7):923–942, 2007.

[DMG15] Awakash Dixit, Sanjay Kumar Mishra, and Arun Kumar Gupta. Sensitivity of singular beams in the presence of zernike aberrations. *Optics and Lasers in Engineering*, 71:74–84, 2015.

[dSMF+18] Nara Rubiano da Silva, Marcel Möller, Armin Feist, Henning Ulrichs, Claus Ropers, and Sascha Schäfer. Nanoscale mapping of ultrafast magnetization dynamics with femtosecond lorentz microscopy. *Physical Review X*, 8(3):031052, 2018.

[DWMD00] SE Derenzo, MJ Weber, WW Moses, and C Dujardin. Measurements of the intrinsic rise times of common inorganic scintillators. *IEEE Transactions on Nuclear Science*, 47(3):860–864, 2000.

[Ege11] Ray F Egerton. *Electron energy-loss spectroscopy in the electron microscope*. Springer Science & Business Media, 2011.

[EHE+15] Dominik Ehberger, Jakob Hammer, Max Eisele, Michael Krüger, Jonathan Noe, Alexander Högele, and Peter Hommelhoff. Highly coherent electron beam from a laser-triggered tungsten needle tip. *Physical review letters*, 114(22):227601, 2015.

[EJR91] J.H. Eberly, J. Javanainen, and K. Rzażewski. Above-threshold ionization. *Physics Reports*, 204(5):331–383, 1991.

[ERKD09] Rolf Erni, Marta D Rossell, Christian Kisielowski, and Ulrich Dahmen. Atomic-resolution imaging with a sub-50-pm electron probe. *Physical review letters*, 102(9):096101, 2009.

[FAB01] Daniel L Freimund, Kayvan Aflatooni, and Herman Batelaan. Observation of the kapitza–dirac effect. *Nature*, 413(6852):142–143, 2001.

[FB02] Daniel L Freimund and Herman Batelaan. Bragg scattering of free electrons using the kapitza-dirac effect. *Physical review letters*, 89(28):283602, 2002.

[FBdS+17] Armin Feist, Nora Bach, Nara Rubiano da Silva, Thomas Danz, Marcel Möller, Katharina E Priebe, Till Domröse, J Gregor Gatzmann, Stefan Rost, Jakob Schauss, et al. Ultrafast transmission electron microscopy using a laser-driven field emitter: Femtosecond resolution with a high coherence electron beam. *Ultramicroscopy*, 176:63–73, 2017.

[FBR+17] Armin Feist, Nora Bach, Nara RubianodaSilva, Thomas Danz, Marcel Möller, Katharina E. Priebe, Till Domröse, J. Gregor Gatzmann, Stefan Rost, Jakob Schauss, Stefanie Strauch, Reiner Bormann, Murat Sivis, Sascha Schäfer, and Claus Ropers. Ultrafast transmission electron microscopy using a laser-driven field emitter: Femtosecond resolution with a high coherence electron beam. *Ultramicroscopy*, 176:63–73, 2017. 70th Birthday of Robert Sinclair and 65th Birthday of Nestor J. Zaluzec PICO

2017 – Fourth Conference on Frontiers of Aberration Corrected Electron Microscopy.

[FDM16] Andrew Forbes, Angela Dudley, and Melanie McLaren. Creation and detection of optical modes with spatial light modulators. *Advances in Optics and Photonics*, 8(2):200–227, 2016.

[FES+15] Armin Feist, Katharina E Echternkamp, Jakob Schauss, Sergey V Yalunin, Sascha Schäfer, and Claus Ropers. Quantum coherent optical phase modulation in an ultrafast transmission electron microscope. *Nature*, 521(7551):200–203, 2015.

[Fie82] James R Fienup. Phase retrieval algorithms: a comparison. *Applied optics*, 21(15):2758–2769, 1982.

[FLIB84] JG Fujimoto, JM Liu, EP Ippen, and N Bloembergen. Femtosecond laser interaction with metallic tungsten and nonequilibrium electron and lattice temperatures. *Physical Review Letters*, 53(19):1837, 1984.

[Fri] Paul Fricker. Zernike polynomials. `https://de.mathworks.com/matlabcentral/fileexchange/7687-zernike-polynomials?focused=6779418&tab=function`. MATLAB Central File Exchange. Retrieved August 31, 2022.

[FYSR20] Armin Feist, Sergey V Yalunin, Sascha Schäfer, and Claus Ropers. High-purity free-electron momentum states prepared by three-dimensional optical phase modulation. *Physical Review Research*, 2(4):043227, 2020.

[Gal] Ohad Gal. fit ellipse. `https://www.mathworks.com/matlabcentral/fileexchange/3215-fit_ellipse`. MATLAB Central File Exchange. Retrieved August 31, 2022.

[GBLM+17] Giulio Guzzinati, Armand Béché, Hugo Lourenço-Martins, Jérôme Martin, Mathieu Kociak, and Jo Verbeeck. Probing the symmetry of the potential of localized surface plasmon resonances with phase-shaped electron beams. *Nature Communications*, 8(1):1–8, apr 2017.

[GCGK+14] Vincenzo Grillo, Gian Carlo Gazzadi, Ebrahim Karimi, Erfan Mafakheri, Robert W. Boyd, and Stefano Frabboni. Highly efficient electron vortex beams generated by nanofabricated phase holograms. *Applied Physics Letters*, 104(4):043109, 2014.

[GdAKcv21] F. Javier García de Abajo and Andrea Konečná. Optical modulation of electron beams in free space. *Phys. Rev. Lett.*, 126:123901, Mar 2021.

[Ger72] Ralph W Gerchberg. A practical algorithm for the determination of phase from image and diffraction plane pictures. *Optik*, 35:237–246, 1972.

[GGG03] Djenan Ganic, Xiaosong Gan, and Min Gu. Focusing of doughnut laser beams by a high numerical-aperture objective in free space. *Optics express*, 11(21):2747–2752, 2003.

[GHH+07] Stefan Gerlich, Lucia Hackermüller, Klaus Hornberger, Alexander Stibor, Hendrik Ulbricht, Michael Gring, Fabienne Goldfarb, Tim Savas, Marcel Müri, Marcel Mayor, et al. A kapitza–dirac–talbot–lau interferometer for highly polarizable molecules. *Nature Physics*, 3(10):711–715, 2007.

[GKG+14] Vincenzo Grillo, Ebrahim Karimi, Gian Carlo Gazzadi, Stefano Frabboni, Mark R. Dennis, and Robert W. Boyd. Generation of nondiffracting electron bessel beams. *Phys. Rev. X*, 4:011013, Jan 2014.

[GRP86] Phillip L Gould, George A Ruff, and David E Pritchard. Diffraction of atoms by light: The near-resonant kapitza-dirac effect. *Physical review letters*, 56(8):827, 1986.

[HBBC12] Peter Hansen, Cory Baumgarten, Herman Batelaan, and Martin Centurion. Dispersion compensation for attosecond electron pulses. *Applied Physics Letters*, 101(8):083501, 2012.

[HCW+18] F. Houdellier, G.M. Caruso, S. Weber, M. Kociak, and A. Arbouet. Development of a high brightness ultrafast transmission electron microscope based on a laser-driven cold field emission source. *Ultramicroscopy*, 186:128–138, 2018.

[HEH+06] Christoph T Hebeisen, Ralph Ernstorfer, Maher Harb, Thibault Dartigalongue, Robert E Jordan, and RJ Dwayne Miller. Femtosecond electron pulse characterization using laser ponderomotive scattering. *Optics letters*, 31(23):3517–3519, 2006.

[HHM+09] M Haider, P Hartel, H Müller, S Uhlemann, and J Zach. Current and future aberration correctors for the improvement of resolution in electron microscopy. *Philosophical Transactions of the Royal Society A: Mathematical, Physical and Engineering Sciences*, 367(1903):3665–3682, 2009.

[HPA+14] Tyler R Harvey, Jordan S Pierce, Amit K Agrawal, Peter Ercius, Martin Linck, and Benjamin J McMorran. Efficient diffractive phase optics for electrons. *New Journal of Physics*, 16(9):093039, sep 2014.

[HRU+98] Max Haider, Harald Rose, Stephan Uhlemann, Eugen Schwan, Bernd Kabius, and Knut Urban. A spherical-aberration-corrected 200 kv transmission electron microscope. *Ultramicroscopy*, 75(1):53–60, 1998.

[HSATK06] Peter Hommelhoff, Yvan Sortais, Anoush Aghajani-Talesh, and Mark A. Kasevich. Field emission tip as a nanometer source of free electron femtosecond pulses. *Phys. Rev. Lett.*, 96:077401, Feb 2006.

[HSB15] Jonathan Handali, Pratistha Shakya, and Brett Barwick. Creating electron vortex beams with light. *Optics Express*, 23(4):5236–5243, 2015.

[HSH+08] Christoph T Hebeisen, German Sciaini, Maher Harb, Ralph Ernstorfer, Thibault Dartigalongue, Sergei G Kruglik, and RJ Dwayne Miller. Grating enhanced ponderomotive scattering for visualization and full characterization of femtosecond electron pulses. *Optics express*, 16(5):3334–3341, 2008.

[HUZ00] M Haider, S Uhlemann, and J Zach. Upper limits for the residual aberrations of a high-resolution aberration-corrected stem. *Ultramicroscopy*, 81(3-4):163–175, 2000.

[IBV22] Francisco Vega Ibáñez, Armand Béché, and Jo Verbeeck. Can a programmable phase plate serve as an aberration corrector in the transmission electron microscope (tem)? *arXiv preprint arXiv:2205.07697*, 2022.

[JB99] EM James and ND Browning. Practical aspects of atomic resolution imaging and analysis in stem. *Ultramicroscopy*, 78(1-4):125–139, 1999.

[JSF+07] A Jesacher, A Schwaighofer, S Fürhapter, C Maurer, S Bernet, and M Ritsch-Marte. Wavefront correction of spatial light modulators using an optical vortex image. *Optics express*, 15(9):5801–5808, 2007.

[KBB+03] Peter A Krulevitch, Paul A Bierden, Thomas Bifano, Emily Carr, Clara E Dimas, Harold Dyson, Michael A Helmbrecht, Peter Kurczynski, Richard S Muller, Scot S Olivier, et al. Moems spatial light modulator development at the center for adaptive optics. In *MOEMS and Miniaturized Systems III*, volume 4983, pages 172–179. SPIE, 2003.

[KCD+08] OL Krivanek, GJ Corbin, N Dellby, BF Elston, RJ Keyse, MF Murfitt, CS Own, ZS Szilagyi, and JW Woodruff. An electron microscope for the aberration-corrected era. *Ultramicroscopy*, 108(3):179–195, 2008.

[KcvdA20] Andrea Konečná and F. Javier García de Abajo. Electron beam aberration correction using optical near fields. *Phys. Rev. Lett.*, 125:030801, Jul 2020.

[KD33] P L Kapitza and P A M Dirac. The reflection of electrons from standing light waves. *Mathematical Proceedings of the Cambridge Philosophical Society*, 29(02):297–300, 1933.

[KDL99] OL Krivanek, N Dellby, and AR Lupini. Towards sub-å electron beams. *Ultramicroscopy*, 78(1-4):1–11, 1999.

[KEH01] Thomas A Klar, Egbert Engel, and Stefan W Hell. Breaking abbe's diffraction resolution limit in fluorescence microscopy with stimulated emission depletion beams of various shapes. *Physical Review E*, 64(6):066613, 2001.

[KESH18] Martin Kozák, Timo Eckstein, Norbert Schönenberger, and Peter Hommelhoff. Inelastic ponderomotive scattering of electrons at a high-intensity optical travelling wave in vacuum. *Nature Physics*, 14(2):121–125, 2018.

[Kha19] Yu N Kharzheev. Radiation hardness of scintillation detectors based on organic plastic scintillators and optical fibers. *Physics of Particles and Nuclei*, 50(1):42–76, 2019.

[Kib66] T. W. B. Kibble. Mutual refraction of electrons and photons. *Phys. Rev.*, 150:1060–1069, Oct 1966.

[KLKB13] Friedrich O Kirchner, Stefan Lahme, Ferenc Krausz, and Peter Baum. Coherence of femtosecond single electrons exceeds biomolecular dimensions. *New Journal of Physics*, 15(6):063021, 2013.

[KLMS+20] Ofer Kfir, Hugo Lourenço-Martins, Gero Storeck, Murat Sivis, Tyler R Harvey, Tobias J Kippenberg, Armin Feist, and Claus Ropers. Controlling free electrons with optical whispering-gallery modes. *Nature*, 582(7810):46–49, 2020.

[KMS+18] M. Kozák, J. McNeur, N. Schönenberger, J. Illmer, A. Li, A. Tafel, P. Yousefi, T. Eckstein, and P. Hommelhoff. Ultrafast scanning electron microscope applied for studying the interaction between free electrons and optical near-fields of periodic nanostructures. *Journal of Applied Physics*, 124:023104, 7 2018.

[KO22] Martin Kozák and Tomáš Ostatnickỳ. Asynchronous inelastic scattering of electrons at the ponderomotive potential of optical waves. *Physical Review Letters*, 129(2):024801, 2022.

[Koz19] M Kozák. All-optical scheme for generation of isolated attosecond electron pulses. *Physical Review Letters*, 123(20):203202, 2019.

[Koz21] Martin Kozak. Electron vortex beam generation via chiral light-induced inelastic ponderomotive scattering. *ACS Photonics*, 8(2):431–435, 2021.

[KR32] Max Knoll and Ernst Ruska. Das elektronenmikroskop. *Zeitschrift für physik*, 78(5):318–339, 1932.

[KR85] H Kohl and H Rose. Theory of image formation by inelastically scattered electrons in the electron microscope. In *Advances in electronics and electron physics*, volume 65, pages 173–227. Elsevier, 1985.

[KRBD17] Maryam Khoshouei, Mazdak Radjainia, Wolfgang Baumeister, and Radostin Danev. Cryo-em structure of haemoglobin at 3.2 å determined with the volta phase plate. *Nature communications*, 8(1):1–6, 2017.

[KSH18] M. Kozák, N. Schönenberger, and P. Hommelhoff. Ponderomotive Generation and Detection of Attosecond Free-Electron Pulse Trains. *Physical Review Letters*, 120(10):103203, 2018.

[Lag] Laguerre polynomials. `https://en.wikipedia.org/wiki/Laguerre_polynomials`. Accessed: 2022-09-17.

[LC86] JA Lin and JM Cowley. Calibration of the operating parameters for an hb5 stem instrument. *Ultramicroscopy*, 19(1):31–42, 1986.

[LCR+08] Thomas LaGrange, Geoffrey H Campbell, BW Reed, Mitra Taheri, J Bradley Pesavento, Judy S Kim, and Nigel D Browning. Nanosecond time-resolved investigations using the in situ of dynamic transmission electron microscope (dtem). *Ultramicroscopy*, 108(11):1441–1449, 2008.

[LF11] Vasudevan Lakshminarayanan and Andre Fleck. Zernike polynomials: a guide. *Journal of Modern Optics*, 58(7):545–561, 2011.

[LHKO12] Grigory Lazarev, Andreas Hermerschmidt, Sven Krüger, and Stefan Osten. Lcos spatial light modulators: trends and applications. *Optical Imaging and Metrology: Advanced Technologies*, 1, 2012.

[LHU+16] Martin Linck, Peter Hartel, Stephan Uhlemann, Frank Kahl, Heiko Müller, Joachim Zach, Max Haider, Marcel Niestadt, Maarten Bischoff, Johannes Biskupek, et al. Chromatic aberration correction for atomic resolution tem imaging from 20 to 80 kv. *Physical review letters*, 117(7):076101, 2016.

[Liu05] Jingyue Liu. Scanning transmission electron microscopy and its application to the study of nanoparticles and nanoparticle systems. *Journal of electron microscopy*, 54(3):251–278, 2005.

[LL07] Hannes Lichte and Michael Lehmann. Electron holography—basics and applications. *Reports on Progress in Physics*, 71(1):016102, 2007.

[Lov97] Gordon D Love. Wave-front correction and production of zernike modes with a liquid-crystal spatial light modulator. *Applied optics*, 36(7):1517–1524, 1997.

[LP91] RA Lerche and DW Phillon. Rise time of bc-422 plastic scintillator< 20 ps. In *Conference Record of the 1991 IEEE Nuclear Science Symposium and Medical Imaging Conference*, pages 167–170. IEEE, 1991.

[MAA+11] Benjamin J. McMorran, Amit Agrawal, Ian M. Anderson, Andrew A. Herzing, Henri J. Lezec, Jabez J. McClelland, and John Unguris. Electron vortex beams with high quanta of orbital angular momentum. *Science*, 331(6014):192–195, 2011.

[MB18] Yuya Morimoto and Peter Baum. Diffraction and microscopy with attosecond electron pulse trains. *Nature Physics*, 14(3):252–256, 2018.

[MCP] Mcp specs. `https://tectra.de/analytics/microchannel-plates/`. Accessed: 2022-08-18.

[Mea22] *https://www.meadowlark.com/*. 2022.

[Mes14] Albert Messiah. *Quantum mechanics*. Courier Corporation, 2014.

[MG01] A Muller and John Grazul. Optimizing the environment for sub-0.2 nm scanning transmission electron microscopy. *Journal of electron microscopy*, 50(3):219–226, 2001.

[MH22] Stefan Meier and Peter Hommelhoff. Coulomb interactions and the spatial coherence of femtosecond nanometric electron pulses. *ACS Photonics*, 9(9):3083–3088, 2022.

[MHS19] Felix Mackenroth, Amol R Holkundkar, and Hans-Peter Schlenvoigt. Ultraintense laser pulse characterization using ponderomotive electron scattering. *New Journal of Physics*, 21(12):123028, 2019.

[MJBRM11a] C Maurer, A Jesacher, S Bernet, and M Ritsch-Marte. What spatial light modulators can do for optical microscopy. *Laser Photonics Reviews*, 5(1):81–101, 2011.

[MJBRM11b] Christian Maurer, Alexander Jesacher, Stefan Bernet, and Monika Ritsch-Marte. What spatial light modulators can do for optical microscopy. *Laser & Photonics Reviews*, 5(1):81–101, 2011.

[MJD+10] H Müller, Jian Jin, R Danev, J Spence, H Padmore, and R M Glaeser. **Design of an electron microscope phase plate using a focused continuous-wave laser**. *New Journal of Physics*, 12(7), 2010.

[MJF+07] Christian Maurer, Alexander Jesacher, Severin Fürhapter, Stefan Bernet, and Monika Ritsch-Marte. Tailoring of arbitrary optical vector beams. *New Journal of Physics*, 9(3):78, 2007.

[MLM+22] I Madan, V Leccese, A Mazur, F Barantani, T La Grange, A Sapozhnik, S Gargiulo, E Rotunno, J-C Olaya, I Kaminer, et al. Ultrafast transverse modulation of free electrons by interaction with shaped optical fields. *arXiv preprint arXiv:2206.02221*, 2022.

[MPSC06] Ben McMorran, John D Perreault, TA Savas, and Alex Cronin. Diffraction of 0.5 kev electrons from free-standing transmission gratings. *Ultramicroscopy*, 106(4-5):356–364, 2006.

[MSM+03] David McGloin, Gabriel C Spalding, H Melville, Wilson Sibbett, and Kishan Dholakia. Applications of spatial light modulators in atom optics. *Optics Express*, 11(2):158–166, 2003.

[NAL90] John A Neff, Ravinda A Athale, and Sing H Lee. Two-dimensional spatial light modulators: a tutorial. *Proceedings of the IEEE*, 78(5):826–855, 1990.

[NCS+13] Bhanu Neupane, Fang Chen, Wei Sun, Daniel T Chiu, and Gufeng Wang. Tuning donut profile for spatial resolution in stimulated emission depletion microscopy. *Review of Scientific Instruments*, 84(4):043701, 2013.

[NH93] Marc Nicklaus and Franz Hasselbach. Wien filter: A wave-packet-shifting device for restoring longitudinal coherence in charged-matter-wave interferometers. *Physical Review A*, 48(1):152, 1993.

[NWA+08] Volodymyr Nikolenko, Brendon O Watson, Roberto Araya, Alan Woodruff, Darcy S Peterka, and Rafael Yuste. Slm microscopy: scanless two-photon imaging and photostimulation using spatial light modulators. *Frontiers in neural circuits*, 2:5, 2008.

[OCP+16] Colin Ophus, Jim Ciston, Jordan Pierce, Tyler R. Harvey, Jordan Chess, Benjamin J. McMorran, Cory Czarnik, Harald H. Rose, and Peter Ercius. Efficient linear phase contrast in scanning transmission electron microscopy with matched illumination and detector interferometry. *Nature Communications*, 7(1):1–7, feb 2016.

[OKK70] Shigehiro Owaki, Yoshitake Kimura, and Masaharu Kawanishi. Scintillation pulse shapes of anthracene single crystals in nanosecond region. ii. difference between scintillation and fluorescence pulses. *Journal of the Physical Society of Japan*, 28(5):1251–1254, 1970.

[OMNA+09] Andrey S Ostrovsky, Gabriel Martínez-Niconoff, Victor Arrizón, Patricia Martínez-Vara, Miguel A Olvera-Santamaría, and Carolina Rickenstorff-Parrao. Modulation of coherence and polarization using liquid crystal spatial light modulators. *Optics express*, 17(7):5257–5264, 2009.

[OVDL22] Pavel K Olshin, Jonathan M Voss, Marcel Drabbels, and Ulrich J Lorenz. Accurate time zero determination in an ultrafast transmission electron microscope without energy filter. *Applied Physics Letters*, 120(10):104103, 2022.

[PHW+05] H Park, Z Hao, X Wang, S Nie, R Clinite, and J Cao. Synchronization of femtosecond laser and electron pulses with subpicosecond precision. *Review of scientific instruments*, 76(8):083905, 2005.

[PLZ10] Sang Tae Park, Milo Lin, and Ahmed H Zewail. Photon-induced near-field electron microscopy (pinem): theoretical and experimental. *New Journal of Physics*, 12(12):123028, 2010.

[PM18] Russell Pollari and Joshua N Milstein. Accounting for polarization in the calibration of a donut beam axial optical tweezers. *PloS one*, 13(2):e0193402, 2018.

[PN11] Stephen J Pennycook and Peter D Nellist. *Scanning transmission electron microscopy: imaging and analysis*. Springer Science & Business Media, 2011.

[PRY+17] Katharina E Priebe, Christopher Rathje, Sergey V Yalunin, Thorsten Hohage, Armin Feist, Sascha Schäfer, and Claus Ropers. Attosecond electron pulse trains and quantum state reconstruction in ultrafast transmission electron microscopy. *Nature Photonics*, 11(12):793–797, 2017.

[PWCD16a] Hui Pang, Jiazhou Wang, Axiu Cao, and Qiling Deng. High-accuracy method for holographic image projection with suppressed speckle noise. *Optics express*, 24(20):22766–22776, 2016.

[PWCD16b] Hui Pang, Jiazhou Wang, Axiu Cao, and Qiling Deng. High-accuracy method for holographic image projection with suppressed speckle noise. *Opt. Express*, 24(20):22766–22776, Oct 2016.

[QM98] Brice Quesnel and Patrick Mora. Theory and simulation of the interaction of ultraintense laser pulses with electrons in vacuum. *Physical Review E*, 58(3):3719, 1998.

[RDFB+16] Halina Rubinsztein-Dunlop, Andrew Forbes, Michael V Berry, Mark R Dennis, David L Andrews, Masud Mansuripur, Cornelia Denz, Christina Alpmann, Peter Banzer, Thomas Bauer, et al. Roadmap on structured light. *Journal of Optics*, 19(1):013001, 2016.

[RDSG97] Gertrude F Rempfer, Denis M Desloge, Walter P Skoczylas, and O Hayes Griffith. Simultaneous correction of spherical and chromatic aberrations with an electron mirror: an electron optical achromat. *Microscopy and Microanalysis*, 3(1):14–27, 1997.

[Rei00] Ludwig Reimer. Scanning electron microscopy: physics of image formation and microanalysis, 2000.

[Rei13] Ludwig Reimer. *Transmission electron microscopy: physics of image formation and microanalysis*, volume 36. Springer, 2013.

[Rem85] Gertrude F Rempfer. Unipotential electrostatic lenses: Paraxial properties and aberrations of focal length and focal point. *Journal of applied physics*, 57(7):2385–2401, 1985.

[Ren06] Dieter Renker. Geiger-mode avalanche photodiodes, history, properties and problems. *Nuclear Instruments and Methods in Physics Research Section A: Accelerators, Spectrometers, Detectors and Associated Equipment*, 567(1):48–56, 2006.

[RK20] Ori Reinhardt and Ido Kaminer. Theory of shaping electron wavepackets with light. *ACS Photonics*, 7(10):2859–2870, 2020.

[RLS+10] BW Reed, T LaGrange, RM Shuttlesworth, DJ Gibson, GH Campbell, and ND Browning. Solving the accelerator-condenser coupling problem in a nanosecond dynamic transmission electron microscope. *Review of Scientific Instruments*, 81(5):053706, 2010.

[Ros09] Harald H Rose. Historical aspects of aberration correction. *Journal of electron microscopy*, 58(3):77–85, 2009.

[RSL+21a] Dolev Roitman, Roy Shiloh, Peng-Han Lu, Rafal E. Dunin-Borkowski, and Ady Arie. Shaping of electron beams using sculpted thin films. *ACS Photonics*, 8(12):3394–3405, 2021.

[RSL+21b] Dolev Roitman, Roy Shiloh, Peng-Han Lu, Rafal E Dunin-Borkowski, and Ady Arie. Shaping of electron beams using sculpted thin films. *ACS photonics*, 8(12):3394–3405, 2021.

[SAC+19] Osip Schwartz, Jeremy J Axelrod, Sara L Campbell, Carter Turnbaugh, Robert M Glaeser, and Holger Müller. Laser phase plate for transmission electron microscopy. *Nature methods*, 16(10):1016–1020, 2019.

[SACF+12] Johannes Schindelin, Ignacio Arganda-Carreras, Erwin Frise, Verena Kaynig, Mark Longair, Tobias Pietzsch, Stephan Preibisch, Curtis Rueden, Stephan Saalfeld, Benjamin Schmid, Jean Yves Tinevez, Daniel James White, Volker Hartenstein, Kevin Eliceiri, Pavel Tomancak, and Albert Cardona. Fiji: An open-source platform for biological-image analysis. *Nature Methods*, 9:676–682, 7 2012.

[SAP96] NB Simpson, L Allen, and MJ Padgett. Optical tweezers and optical spanners with laguerre–gaussian modes. *Journal of modern optics*, 43(12):2485–2491, 1996.

[Sax00] WO Saxton. A new way of measuring microscope aberrations. *Ultramicroscopy*, 81(2):41–45, 2000.

[Sch36a] O_ Scherzer. Über einige fehler von elektronenlinsen. *Zeitschrift für Physik*, 101(9):593–603, 1936.

[Sch36b] O. Scherzer. Über einige Fehler von Elektronenlinsen. *Zeitschrift für Physik*, 101(9-10):593–603, sep 1936.

[Sch47] O Scherzer. Spharische und chromatische korrektur von elektronen-linsen. *Optik*, 2:114–132, 1947.

[Sch49] O Scherzer. The theoretical resolution limit of the electron microscope. *Journal of Applied Physics*, 20(1):20–29, 1949.

[Sch73] H Schwarz. The kapitza-dirac effect at high laser intensities. *Physics Letters A*, 43(5):457–458, 1973.

[Sch22a] Matthias Schneller. *Simulations of electron-light interactions*. DOI:10.25365/thesis.72344, University of Vienna, 2022.

[SCH22b] R Shiloh, T Chlouba, and P Hommelhoff. Quantum-coherent light-electron interaction in a scanning electron microscope. *Physical Review Letters*, 128(23):235301, 2022.

[SF42] Karl Spangenberg and Lester M Field. Some simplified methods of determining the optical characteristics of electron lenses. *Proceedings of the IRE*, 30(3):138–144, 1942.

[SG2] plastic scintillator. `https://www.crystals.saint-gobain.com/radiation-detection-scintillators/plastic-scintillators`. Accessed: 2022-05-17.

[SGHM05] Bradley J. Siwick, Alexander A. Green, Christoph T. Hebeisen, and R. J. Dwayne Miller. Characterization of ultrashort electron pulses by electron-laser pulse cross correlation. *Opt. Lett.*, 30(9):1057–1059, May 2005.

[Sha12] Ramamurti Shankar. *Principles of quantum mechanics*. Springer Science & Business Media, 2012.

[SKE+15] Tomoyoshi Shimobaba, Takashi Kakue, Yutaka Endo, Ryuji Hirayama, Daisuke Hiyama, Satoki Hasegawa, Yuki Nagahama, Marie Sano, Minoru Oikawa, Takashige Sugie, et al. Improvement of the image quality of random phase-free holography using an iterative method. *Optics Communications*, 355:596–601, 2015.

[SLLA14] Roy Shiloh, Yossi Lereah, Yigal Lilach, and Ady Arie. Sculpturing the electron wave function using nanoscale phase masks. *Ultramicroscopy*, 144:26–31, 2014.

[SRL+18] Roy Shiloh, Roei Remez, Peng-Han Lu, Lei Jin, Yossi Lereah, Amir H Tavabi, Rafal E Dunin-Borkowski, and Ady Arie. Spherical aberration correction in a scanning transmission electron microscope using a sculpted thin film. *Ultramicroscopy*, 189:46–53, 2018.

[SS70] ES Sarachik and GT Schappert. Classical theory of the scattering of intense laser radiation by free electrons. *Physical Review D*, 1(10):2738, 1970.

[SSH+08] H Sawada, T Sannomiya, F Hosokawa, T Nakamichi, T Kaneyama, T Tomita, Y Kondo, T Tanaka, Y Oshima, Y Tanishiro, et al. Measurement method of aberration from ronchigram by autocorrelation function. *Ultramicroscopy*, 108(11):1467–1475, 2008.

[SSH19] Noah Schnitzer, Suk Hyun Sung, and Robert Hovden. Introduction to the ronchigram and its calculation with ronchigram. com. *Microscopy Today*, 27(3):12–15, 2019.

[SSR+07] R Scheuermann, A Stoykov, D Renker, Z Sadygov, R Mehtieva, A Dovlatov, and V Zhuk. Scintillation detectors for operation in high magnetic fields: Recent developments based on arrays of avalanche microchannel photodiodes. *Nuclear Instruments and Methods in Physics Research Section A: Accelerators, Spectrometers, Detectors and Associated Equipment*, 581(1-2):443–446, 2007.

[SSS12] A Stoykov, R Scheuermann, and K Sedlak. A time resolution study with a plastic scintillator read out by a geiger-mode avalanche photodiode. *Nuclear Instruments and Methods in Physics Research Section A: Accelerators, Spectrometers, Detectors and Associated Equipment*, 695:202–205, 2012.

[SSVDS12] S Seifert, JHL Steenbergen, HT Van Dam, and DR Schaart. Accurate measurement of the rise and decay times of fast scintillators with solid state photon counters. *Journal of Instrumentation*, 7(09):P09004, 2012.

[TAC+21] Carter Turnbaugh, Jeremy J Axelrod, Sara L Campbell, Jeske Y Dioquino, Petar N Petrov, Jonathan Remis, Osip Schwartz, Zanlin Yu, Yifan Cheng, Robert M Glaeser, et al. High-power near-concentric fabry–perot cavity for phase contrast electron microscopy. *Review of scientific instruments*, 92(5):053005, 2021.

[TBM+18] Amir H Tavabi, Marco Beleggia, Vadim Migunov, Alexey Savenko, Ozan Öktem, Rafal E Dunin-Borkowski, and Giulio Pozzi. Tunable ampere phase plate for low dose imaging of biomolecular complexes. *Scientific reports*, 8(1):1–5, 2018.

[TDW+22] Shai Tsesses, Raphael Dahan, Kangpeng Wang, Ori Reinhardt, Guy Bartal, and Ido Kaminer. Tunable photon-induced spatial modulation of free electrons. *arXiv preprint arXiv:2203.08518*, 2022.

[TRR+21] Amir H. Tavabi, Paolo Rosi, Enzo Rotunno, Alberto Roncaglia, Luca Belsito, Stefano Frabboni, Giulio Pozzi, Gian Carlo Gazzadi, Peng-Han Lu, Robert Nijland, Moumita Ghosh, Peter Tiemeijer, Ebrahim Karimi, Rafal E. Dunin-Borkowski, and Vincenzo Grillo. Experimental demonstration of an electrostatic orbital angular momentum sorter for electron beams. *Phys. Rev. Lett.*, 126:094802, Mar 2021.

[UKS21] Yuuki Uesugi, Yuichi Kozawa, and Shunichi Sato. Electron round lenses with negative spherical aberration by a tightly focused cylindrically polarized light beam. *Phys. Rev. Applied*, 16:L011002, Jul 2021.

[UKS22] Yuuki Uesugi, Yuichi Kozawa, and Shunichi Sato. Properties of electron lenses produced by ponderomotive potential with bessel and laguerre–gaussian beams. *Journal of Optics*, 24(5):054013, 2022.

[UMH+13] Stephan Uhlemann, Heiko Müller, Peter Hartel, Joachim Zach, and Max Haider. Thermal magnetic field noise limits resolution in transmission electron microscopy. *Physical review letters*, 111(4):046101, 2013.

[UT10] Masaya Uchida and Akira Tonomura. Generation of electron beams carrying orbital angular momentum. *Nature*, 464(7289):737–739, apr 2010.

[VBLL+13] Noa Voloch-Bloch, Yossi Lereah, Yigal Lilach, Avraham Gover, and Ady Arie. Generation of electron Airy beams. *Nature*, 494(7437):331–335, feb 2013.

[VBM+19] Giovanni Maria Vanacore, Gabriele Berruto, Ivan Madan, Enrico Pomarico, P Biagioni, RJ Lamb, D McGrouther, O Reinhardt, I Kaminer, B Barwick, et al. Ultrafast generation and control of an electron vortex beam via chiral plasmonic near fields. *Nature materials*, 18(6):573–579, 2019.

[VBMC+18] Jo Verbeeck, Armand Béché, Knut Müller-Caspary, Giulio Guzzinati, Minh Anh Luong, and Martien Den Hertog. Demonstration of a 2×2 programmable phase plate for electrons. *Ultramicroscopy*, 190:58–65, 2018.

[VMB+18] Giovanni M Vanacore, I Madan, G Berruto, K Wang, E Pomarico, RJ Lamb, D McGrouther, I Kaminer, B Barwick, F Javier García de Abajo, et al. Attosecond coherent control of free-electron wave functions using semi-infinite light fields. *Nature communications*, 9(1):1–11, 2018.

[VMPA98] Fernando Vargas-Martın, Pedro M Prieto, and Pablo Artal. Correction of the aberrations in the human eye with a liquid-crystal spatial light modulator: limits to performance. *JOSA A*, 15(9):2552–2562, 1998.

[Voe11] David George Voelz. *Computational fourier optics: a MATLAB tutorial*, volume 534. SPIE press Bellingham, Washington, 2011.

[VTS10] Johan Verbeeck, He Tian, and Peter Schattschneider. Production and application of electron vortex beams. *Nature*, 467(7313):301–304, 2010.

[WDS+20] Kangpeng Wang, Raphael Dahan, Michael Shentcis, Yaron Kauffmann, Adi Ben Hayun, Ori Reinhardt, Shai Tsesses, and Ido Kaminer. Coherent interaction between free electrons and a photonic cavity. *Nature*, 582(7810):50–54, 2020.

[Wei00] Andrew M Weiner. Femtosecond pulse shaping using spatial light modulators. *Review of scientific instruments*, 71(5):1929–1960, 2000.

[WKBV14] B Winter, SJ King, M Brouard, and C Vallance. A fast microchannel plate-scintillator detector for velocity map imaging and imaging mass spectrometry. *Review of Scientific Instruments*, 85(2):023306, 2014.

[WLM+14] Chen Wang, Rui Liu, Daniel E Milkie, Wenzhi Sun, Zhongchao Tan, Aaron Kerlin, Tsai-Wen Chen, Douglas S Kim, and Na Ji. Multiplexed aberration measurement for deep tissue imaging in vivo. *Nature methods*, 11(10):1037–1040, 2014.

[WR01] Christoph Weißbäcker and Harald Rose. Electrostatic correction of the chromatic and of the spherical aberration of charged-particle lenses. *Journal of electron microscopy*, 50(5):383–390, 2001.

[YKKW06] Takashi Yamazaki, Yasutoshi Kotaka, Yoshio Kikuchi, and Kazuto Watanabe. Precise measurement of third-order spherical aberration using low-order zone-axis ronchigrams. *Ultramicroscopy*, 106(3):153–163, 2006.

[YMZ10] Ding-Shyue Yang, Omar F Mohammed, and Ahmed H Zewail. Scanning ultrafast electron microscopy. *Proceedings of the National Academy of Sciences*, 107(34):14993–14998, 2010.

[Zew10] Ahmed H Zewail. Four-dimensional electron microscopy. *science*, 328(5975):187–193, 2010.

[ZH95] Joachim Zach and Maximilian Haider. Aberration correction in a low voltage sem by a multipole corrector. *Nuclear Instruments and Methods in Physics Research Section A: Accelerators, Spectrometers, Detectors and Associated Equipment*, 363(1-2):316–325, 1995.

[ZSS+20] S. Zimmermann, K. Suzuki, D. Steinschaden, N. Kratochwil, W. Nalti, H. Orth, C. Schwarz, A. Lehmann, M. Böhm, and K.-Th. Brinkmann. The p anda barrel time-of-flight detector. *Nuclear Instruments and Methods in Physics Research Section A: Accelerators, Spectrometers, Detectors and Associated Equipment*, 952:161635, 2020. 10th International Workshop on Ring Imaging Cherenkov Detectors (RICH 2018).

[Zwi22] Barton Zwiebach. *Mastering Quantum Mechanics: Essentials, Theory, and Applications*. MIT Press, 2022.

[ZZW+20] Chunhui Zhu, Dingguo Zheng, Hong Wang, Ming Zhang, Zhongwen Li, Shuaishuai Sun, Peng Xu, Huanfang Tian, Zian Li, Huaixin Yang, et al. Development of analytical ultrafast transmission electron microscopy based on laser-driven schottky field emission. *Ultramicroscopy*, 209:112887, 2020.

Acronyms

BBO β-barium borate. 13

BC Bicron. 34, 35, 37

CFEG cold field emission gun. 2, 59

CMOS Complementary metal oxide semiconductor. 15, 16, 18, 26, 28, 30, 39, 43–45, 71, 96

CP conjugate plane. 14, 25, 26, 29, 30, 49, 71

FWHM full width half maximum. 42, 69, 73

GSA Gerchberg-Saxton algorithm. 4, 19–21, 23–30, 33, 44, 69, 76

IP interaction plane. 14, 26, 29, 34, 36, 37, 40–42, 44, 61, 67, 70, 73, 76, 96, 97

IR infrared. 13, 14, 17, 36–39, 96, 97

LC liquid crystal. 19

LG Laguerre Gaussian. 31–33, 48–56, 69, 70

MCP microchannel plate. 4, 15, 16, 43, 55, 66

MPPC multi-pixel photon counters. 35

NA numerical aperture. 26, 28, 32, 33, 36, 69, 72, 75

OA objective aperture. 36, 40, 42, 67, 69

OL objective lens. 40, 67, 68, 73

P43 phosphor screen. 16

PINEM Photon Induced Near Field Electron Microscopy. 2

SEM scannig electron microscope. vi, 2, 4, 13–15, 17, 18, 40, 42, 57, 67, 69, 73

SFEG Schottky field emission gun. 2

SiPM Silicon Photomultiplier. 35–37

SLM spatial light modulator. 4, 13, 14, 17–19, 22–25, 28, 29, 31–33, 39, 43–46, 48, 49, 70, 71, 76, 96

STED Stimulated emission depletion. 31

STEM scanning transmission electron microsocpe. 58, 63

TEM Transmission electron microsocpe. 4, 18, 43, 55, 57, 58, 69, 70, 73

UEM ultrafast electron miscroscope. 1

UTEM ultrafast transmission electron miscroscope. 1

UV ultraviolet. 13–16, 68

10 Appendix

10.1 Laser beam power measurement

Due to space constraints, the power levels in the IP were not measured directly with the power meter. A CMOS has been calibrated to measure the power levels of the laser beam before the SLM and in the IP to determine the transmission coefficient $T_{c_L} = P_{IP}/P_{PBS} = 0.275$ along the beam path. The power after the polarizing beam splitter (P_{PBS}) is measured directly with a power meter. The power in the IP (P_{IP}) is determined by measuring the intensity (I_{IP}) of the IR laser beam with the calibrated CMOS placed in the IP. Figure 10.1 shows the calibration of the CMOS (OV5647) camera, which was done outside of the vacuum chamber. The slope gives the recorded counts per Watt of incident laser power ($P_{IP} = I_{IP}/\text{slope}$). One can see that only a low fraction of the laser beam makes it to the IP. The losses come mainly from the SLM, the hole in the 45 mirror, and the other laser beam optics along the beam path. Figure 10.2 (black data) shows the determined power levels in the interaction plane, which were further used to calculate the focal lengths of the ponderomotive lenses.

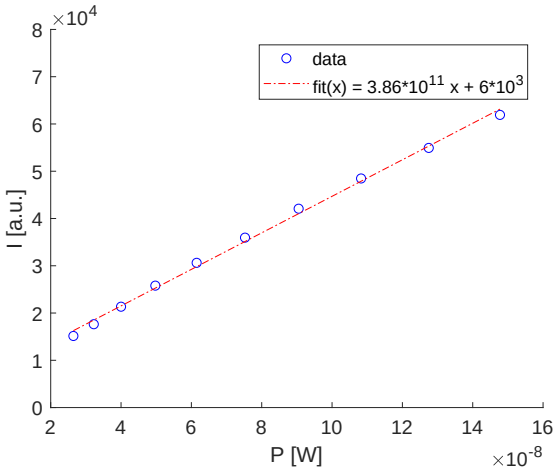


Figure 10.1: Calibration of a CMOS to measure power levels of the laser beam in the IP. The intensity (counts) of the laser beam is recorded outside vacuum with a CMOS and plotted against the measured power levels. The slope of the fitting curve is used to determine the power levels in the IP.

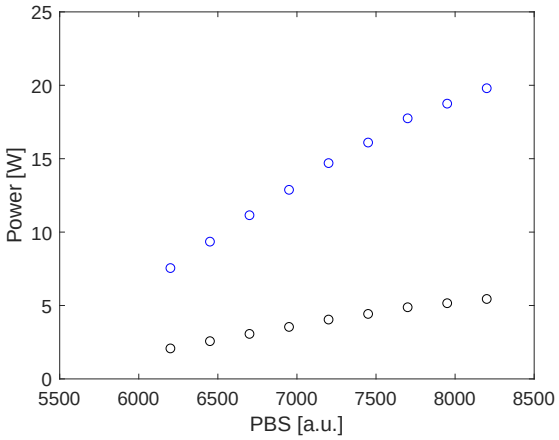


Figure 10.2: Power of the levels of the IR laser beam (at 50% output) measured with a power meter after the polarizing beam splitter (blue) plotted as a function of the half-wave plate rotation. Black data points are the power levels in the IP determined by multiplying the blue data points with T_{c_L}.